A data-driven model for magnetostatics

by

M.W. Schaaphok

to obtain the degree of Bachelor of Science
at the Delft University of Technology,
to be defended publicly on July 12th 2018.

Student number:	4355822	
Project duration:	April 23rd, 2018 – July 12th, 2018	
Thesis committee:	Ir. A.R.P.J. Vijn,	TU Delft, supervisor
	Prof. dr. ir. A. W., Heemink,	TU Delft, supervisor
	Dr. B. van den Dries,	TU Delft

TU Delft Delft University of Technology

Een data-gedreven model voor magnetostatica

M.W. Schaaphok

ter verkrijging van de graad van Bachelor of Science
aan de Technische Universiteit Delft,
in het openbaar te verdedigen op 12 juli 2018.

Studentnummer:	4355822	
Project lengte:	23 april 2018 – 12 juli 2018	
Thesis commissie:	Ir. A.R.P.J. Vijn,	TU Delft, supervisor
	Prof. dr. ir. A. W. Heemink,	TU Delft, supervisor
	Dr. B. van den Dries,	TU Delft

Een electronische versie van deze thesis is verkrijgbaar op `http://repository.tudelft.nl/`.

TU Delft Delft University of Technology

Abstract

This research presents a data-driven model for the magnetic signature of an object, consisting of linearly reacting isotropic material. From magnetostatics a mathematical-physical model is derived for the linear behaviour of the induced magnetization. Data-driven updates for the permanent magnetization are computed from comparisons of the computed magnetic field with measurements from onboard sensors, in order to describe magnetic hysteresis. In order to improve the solutions for ill-posed inverse problems, the Tikhonov regularization method is studied. Furthermore, the performance of the model is examined by a number of twin experiments.

Index terms - magnetic signature, permanent magnetization, induced magnetization, inverse problem, data-driven,regularization.

Acknowledgements

I want to give special thanks to my supervisor Aad Vijn for his help and enthusiasm during the complete process of this research and the lively discussions in case I ran into difficulties or unexpected results. The meetings we had were very pleasant and inspiring.

Furthermore I would like to thank my second supervisor Arnold Heemink for his input, ideas and feedback during the research.

Lastly I want to thank Eugene Lepelaars (TNO) for making it possible to visit the experimental setup at TNO and for his help with producing experimental data, even though time-wise I wasn't able to use it.

Preface

This report is written as part of completing the bachelor 'Applied Mathematics' at Delft University of Technology, Netherlands. From April 23rd until July 12th I have been working on this project and in this report an outline is given of the work that I have done and the accomplished results.

For 12 weeks I have been working on the construction of a so called *magnetic signature monitoring system* for naval vessels. This research is part of a much larger research conducted by TNO for DMO (Defence Material Organisation). The main goal of the broad research for DMO is to design a closed loop degaussing system for naval vessels. The focus of my research within this overall research was on the usage of data-assimilation in order to estimate the permanent magnetization. It was nice to be able to visit TNO and the experimental setup in order to gain more feeling with the project. Due to these visits, the lively talks with my supervisors and the project itself, I became very enthusiastic to work on this project. During the past 12 weeks I have worked with much pleasure on this project and I have gained a lot of knowledge and experience.

Unfortunately, due to time reasons, it has not been possible to add an analysis on the performance of the model on experimental data from the setup at TNO. In the near future, the model will be tested using these measurements from the experimental set-up. From these tests it can be concluded how well the model performs on data from the real-life setup.

List of symbols

Symbol	Meaning	Unit
χ	Magnetic susceptibility	
H_a	Applied field	Am^{-1}
H_{red}	Reduced magnetic induction field	Am^{-1}
M	Total magnetization object	Am^{-1}
M_{ind}	Induced magnetization object	Am^{-1}
M_{per}	Permanent magnetization object	Am^{-1}
B_m^{arr}	Measured magnetic field at array	Tesla
B_c^{arr}	Computed magnetic field at array	T
B_m^b	Measured magnetic field in the box	T
B_c^b	Computed magnetic field in the box	T
μ_0	Magnetic permeability	$4\pi \cdot 10^{-7}$ H/m
ϕ_i	Linear basis function	-
Φ_{red}	Potential function for $\mathbf{H}_{red}$	-
e_k	Triangular element k	-
v_i	Vertex i of triangular element	-
Ω	Object geometry	-
N_e	Number of elements	-
λ	Regularization parameter	-
R	Regularization operator	-
γ_i	Filter factors GSVD	-
ϵ_{abs}^s	Absolute field error per sensor	T
ϵ_{rel}^s	Relative field error per sensor	-
ε_{abs}^d	Absolute error per direction	T
ε_{rel}^d	Relative error per direction	-

Table 1: List of symbols

Contents

Acknowledgements . . . ii
Preface . . . iii
List of symbols . . . v

1 Introduction **1**
1.1 Motivation research . . . 1
1.2 Introduction research . . . 2
1.3 Chapter outline . . . 3

2 Research objective and approach **5**
2.1 Research objective . . . 5
2.2 Approach . . . 6

3 Magnetism **9**
3.1 Magnetic hysteresis . . . 9
3.2 Assumption on M . . . 9
3.3 Magnetostatics . . . 10

4 Numerical Forward Model for Magnetostatics **13**
4.1 The discrete forward model . . . 13
4.1.1 Linear basis functions . . . 14
4.1.2 Expansions of M . . . 14
4.1.3 Computation of the matrix entries . . . 15
4.1.4 Computation of the normal vectors . . . 18
4.2 Forward computation to the sensor positions . . . 19

5 Inverse problems **21**
5.1 Inverse problem formulation . . . 21
5.2 Singular value decomposition . . . 22
5.3 Tikhonov regularization . . . 23
5.4 Tikhonov error analysis . . . 25

6 Magnetic state model **27**
6.1 Computation permanent magnetization . . . 27
6.1.1 Initial State . . . 27
6.1.2 Data-driven update . . . 28
6.2 The inverse problem . . . 29
6.2.1 Regularization for $\mathbf{M}_{per}$ . . . 29
6.2.2 Smoothing operator for $\mathbf{M}_{per}$ . . . 30
6.3 Signature Monitoring Model . . . 31

7 Steel Vessel Prototype 01 and setup **35**

8 Twin Experiments **39**
8.1 General notions . . . 40
8.2 Data generation . . . 40
8.3 Phase I: Fixed permanent magnetization with noiseless data . . . 41
8.3.1 Regularization . . . 41
8.3.2 Data-assimilation . . . 45
8.3.3 Y- and z-direction . . . 45

8.4 Conclusion phase I . . . 48
8.5 Phase II.1: Fixed permanent magnetization with noisy data . . . 49
8.6 Phase II.2: Model adaptions . . . 51
8.6.1 Induced magnetization . . . 51
8.6.2 Initial condition . . . 51
8.7 Conclusion phase II . . . 54
8.8 Phase III.1: Magnetic hysteresis . . . 55
8.9 Phase III.2: Non-uniform permanent magnetization . . . 57
8.10 Phase III.3: Unknown susceptibility distribution . . . 59
8.11 Conclusion phase III . . . 64

9 Conclusion **65**
9.1 Research objectives and main results . . . 65
9.2 Signature Monitoring Model . . . 66
9.3 Performance of the model . . . 66

10 Future research **67**
10.1 Inverse problems . . . 67
10.1.1 Regularization methods . . . 67
10.1.2 Regularization parameter . . . 67
10.2 Data-assimilation . . . 68
10.2.1 Permanent magnetization . . . 68
10.2.2 Susceptibility . . . 68
10.2.3 Number of sensors . . . 68
10.3 Performance tests . . . 68
10.3.1 Computational efficiency . . . 68
10.3.2 Internal structure . . . 69
10.3.3 Influence of distance . . . 69
10.3.4 Complex situations and prototypes . . . 69
10.3.5 Experimental Data . . . 69

Bibliography **70**

A Enlarged figures **72**

1 Introduction

First the background information and the motivation for the research are provided. Then an insight into the broad research done by The Netherlands Organization for Applied Scientific Research (TNO) is given, after which it is narrowed down to the introduction of the subject of our research.

1.1. Motivation research

The Royal Netherlands Navy is active in many international waters. Their operations take place in waters with a high threat of naval mines, this can differ from areas with leftover mines from previous wars to areas where mines are used as an active defense mechanism. Detonation of a mine can severely damage a naval ship, endangering the success of the mission. Therefore it is of utmost importance to decrease any risk on the detonation of a mine. Sweeping the waters for mines in advance is a difficult, time inefficient and costly operation. This is undesirable since the Navy often has to act fast and every slight delay can endanger the success of the mission. For a long time contact mines have been popular, these mines float on or just beneath the surface. As contact mines are close to the surface, they can be detected quite easily with the modern technology. Nowadays, so called influence mines are more frequently used, this type of mines can be positioned far below the surface and they can detonate on basis of the vessels signature. As one can imagine naval vessels emit many signals by which it can be identified, e.g. electric, acoustic, pressure and magnetic, see figure 1.1 for an overview. A naval vessels signature is defined by the complete picture of the propagation of these signals in the environment. The influence mines can detonate on ground of the magnetic signature, they measure the disturbance of the Earths magnetic field by the magnetic field of the vessel. The magnetic field of the vessel is created by the magnetization of the steel hull due to the Earths magnetic field. To decrease the chance of detonating an influence mine, it is essential to minimize the signature of the vessels, [10], [11], [12]. TNO conducts research in describing and decreasing the signatures of the vessels, focusing mainly on the underwater signatures. In this research the focus is only on the magnetic signatures of the vessels and when speaking of signatures we will always refer to the magnetic signature.

Figure 1.1: Overview signatures naval vessel [23]

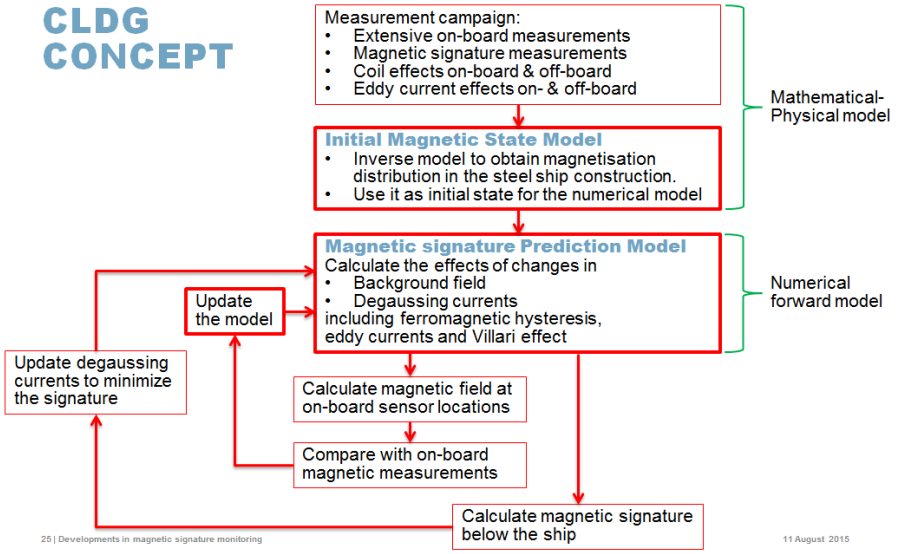

Figure 1.2: Closed Loop Degaussing Concept [23]

1.2. Introduction research

The ultimate goal in the research on magnetic signatures is to equip the naval vessels with a closed-loop degaussing system, which will reduce the magnetic signature in real-time. For an overview of this system, see figure 1.2. In [1] such a system is defined and a proof of concept is given. In order to reduce the signature in real-time, the naval vessels must be equipped with both a *signature monitoring system* and a *signature management system*. The monitoring system should be able to track and visualize the signature at a certain distance around the vessel. Based on the predictions of the monitoring system the management system should reduce the computed signatures by controlling the currents in the coils and thereby the generated fields. The desired fields can be generated by large coils, which will be placed in the hull of the vessel in all three directions. If the signatures are known, opposite field can be generated to reduce the magnetic signature and thereby decrease the chance of detonating a mine. In this research we set a step into the direction of developing a magnetic signature monitoring system. From the CLDG concept in figure 1.2 we work on the *Initial Magnetic State Model* and the *Magnetic signature Prediction Model*. The model update loop based on measurements from onboard sensors is included in the model, but effects of changes in degaussing currents and influences of eddy currents and the Villari effect are left for future research. The developed system should be able to effectively compute the magnetic state of our Steel Vessel Prototype 01 (SVP01) and to predict the signature at a certain depth beneath this vessel.

In general the identification of the magnetic state of steel and other ferromagnetic materials is difficult due to its hysteretic behaviour [3]. To be able to describe the magnetization of the objects, the total magnetization is split into two parts: the induced magnetization and the permanent magnetization [20]. The induced magnetization is a linear reaction of the material to the applied background field and is dependent on the magnetic susceptibility. Although the magnetic susceptibility is not as straightforward for alloys as for pure materials, there are methods available to approximate this property [22]. The permanent magnetization is the more challenging part of the description as it is caused by the magnetic history of the object. The permanent magnetization has both a direct influence on the magnetization of the object and an indirect influence on the induced magnetization. To achieve accurate predictions it is important to be able to describe this phenomenon. There are already several approaches to the subject of hysteresis, for example by Jiles and Atherthon models [14],[24], Harrisons models[9],[8], Rayleigh model [15] and Preisach Models [21]. For the monitoring system we do not make use of one of these models. Instead data-assimilation from the onboard sensors is used to track the permanent magnetization.
In this research the focus is on predicting the magnetic state and magnetic signature of an object, consisting of linear reacting isotropic material. The monitoring system is based on the description of the magnetization by considering permanent magnetization as well as induced magnetization. From the onboard sensors

data is collected of the magnetic induction field inside the object. This data is used to update the permanent magnetization of the material. Using this data-based correction we hope to capture the evolution of the permanent magnetization of the vessel. Firstly a mathematical model, able to describe and compute both induced and permanent magnetization is developed. For this development the approach in [22] is followed and extended. A numerical model for the reduced magnetic field at an array below the the object is constructed and implemented in Matlab. For validation the model is tested with a number of twin experiments on a 3-dimensional object.

1.3. Chapter outline

The structure of the report is given by an outline of each chapter:

Chapter 2 states the research objectives and gives an approach to the development of the desired model.

Chapter 3 introduces the concept of magnetic hysteresis and magnetostatics. From the basic magnetostatic field equations an integral expression for the reduced magnetic field and an integral equation for the magnetization are derived. When the material properties, like magnetic susceptibility, and the permanent magnetization are known, this integral equation determines the induced magnetization of the object.

Chapter 4 presents a discretization of this integral equation based on a finite element method with triangular elements and linear basis functions. From this discretization the numerical model is developed. Further the forward model, necessary to compute induced magnetic fields from the magnetization of an object, is presented.

Chapter 5 introduces inverse problem formulations and difficulties accompanied with solving inverse problems. Moreover it discusses methods to improve solutions from inverse problems, like regularization. In order to gain insight into the effects of regularization, the generalized eigenvalue decomposition is explained.

Chapter 6 combines the previous chapters to arrive at the final model for the magnetic signature. First methods for the computation of the initial permanent magnetization are provided. Further the model for the data-driven corrections is presented. The necessary inverse problems are derived from the connected forward problems and are correctly reformulated with use of regularization. At last this chapter presents pseudo-codes for the complete model.

Chapter 7 describes the laboratory set up and the steel vessel prototype, which is used for the validation of the model. Furthermore the model defines the method of meshing the object.

Chapter 8 presents and discusses the results of the twin experiments conducted to validate the model. For the validation of the model a number of data sets with different permanent magnetizations are generated. Furthermore two improvements are posed and analyzed.

Chapter 9 contains the conclusions drawn from the results in the previous chapter.

Chapter 10 at last gives recommendations for future research.

2

Research objective and approach

In this chapter the research objective is be posed and explained. Moreover sub-objectives are formulated combined with their contribution to the main objective. At last the approach for the development of the model is discussed.

2.1. Research objective

The main objective of the research is defined as follows:

Design, implement and test a data-driven model for the magnetic signature of an object, made of linearly reacting isotropic material, considering both induced and permanent magnetization.

The model should be able to predict the magnetic induction field at a sensor array beneath the object. This prediction is based on data from measurements of the onboard magnetic induction field, knowledge of the applied field and the susceptibility distribution of the material. After the initial computation of the permanent magnetization, the permanent magnetization should be updated each step according to measurements from the onboard sensors. We hope to gain knowledge on how well the evolution of the permanent magnetization of the object in time can be approximated. Further it is also of interest to know to which extend errors in the approximation of the magnetization translate into errors in the prediction of the magnetic signature. In order to do this the mathematical-physical model is designed, which consists of both forward and inverse problems. Since difficulties often arise with inverse problems, a literature study on inverse problems is performed and methods like regularization are explored to be able to cope with these difficulties. If the model is designed and implemented, its performance is tested. This validation is done by conducting various twin experiments, using a 3-dimensional steel vessel prototype. For each of the experiments test data is generated and the results of the experiments are analyzed in order to give well argued conclusions on the accuracy of the model. At the end we hope to give some remarks on how the hysteresis behaviour of isotropic material is of influence on a first order approximation of the magnetic behaviour of isotropic material. To sum up the sub-objectives are described as follows:

- Design a mathematical-physical model, create the numerical model and implement the model;
- Perform a study on inverse problems, difficulties associated with inverse problems and methods, like regularization, to cope with these difficulties;
- Design and perform twin experiments to test the performance of the model;
- Research the accuracy of the predictions of the magnetic signature;
- Gain insight in the translation of errors in the approximation of the magnetization to errors in the signature prediction;
- Gain knowledge of the influence of inaccuracies in the estimation of the susceptibility on the accuracy of the prediction of the induced magnetic field.

2.2. Approach

In the introduction the concept of the closed loop degaussing system was illustrated in figure 1.2. In this section we look more closely at the concept of the signature monitoring model and the approach used to develop this model. In the research the focus is on three different parts of the CLDG concept: the initial magnetic state model, the magnetic signature prediction model and the (small) update loop using the onboard sensor data. See also figure 2.1.

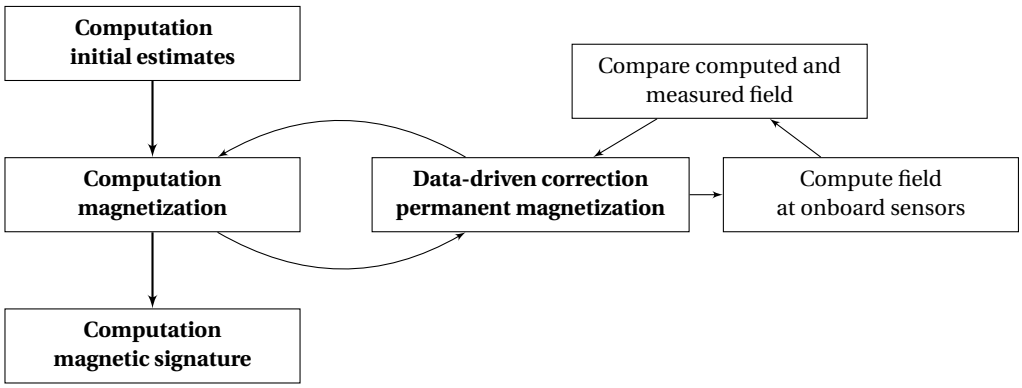

Figure 2.1: Basic Structure magnetic signature monitoring system

Here we look at a more detailed approach of the steps that need to be taken in the two main parts of the model, the computation of the magnetic state and the computation of the magnetic signature. At the start the initial magnetization and magnetic susceptibility distribution need to be computed. The magnetic state of the model is defined as the total magnetization $\mathbf{M}$, which consist of the induced magnetization $\mathbf{M}_{ind}$ and the permanent magnetization $\mathbf{M}_{per}$:

$$\mathbf{M} = \mathbf{M}_{ind} + \mathbf{M}_{per}.$$

This is explained in more detail in the next chapter.

The magnetic susceptibility, denoted by χ, is a material parameter which has to be estimated for the specified object. For the estimation of this parameter the Magnetic Susceptibility Estimator Method from [22] can be used. We assume χ to be constant in time but not in space, such that the susceptibility distribution is non-uniform over the object. The first main part of the model is the computation of the magnetic state, in which both the induced and permanent magnetization are estimated. The mathematical model for the induced magnetization is derived from basic magnetostatics. This model is used and adapted to include the permanent magnetization. Therefore an integral equation is derived from basic magnetostatics and discretized. From the integral equation the numerical forward model can be constructed.

The forward model is able to compute the induced magnetic field at certain locations. In order to do so, we consider the necessary linear basis function and expand the magnetization using these basis functions. The integral equation is rewritten to a matrix equation which can be solved more efficiently. Using the induced magnetization from the current iteration and the permanent magnetization from the previous iteration a forward problem is solved to find the computed induced magnetic field at the onboard sensors. From the numerical forward model the inverse problem is formulated. This inverse problem has to be solved to find the induced magnetization from the applied field and the permanent magnetization.

After these models have been constructed we move to the construction of the data-driven update of the permanent magnetization. This correction is based on the difference between the computed and the measured magnetic induction field at the onboard sensors. The computation of the correction is based on an inverse problem. In order to improve the solutions from the inverse problems a study on regularization methods is performed. From the computed induced magnetization and updated permanent magnetization the total magnetization can be computed. The updated permanent magnetization is then saved for the next iteration.

If the magnetic state of the object is computed, the model moves to the next step: the computation of the magnetic signature. Another forward problem has to be solved to find the computed magnetic induction field at the sensor array below the vessel. The computed values of the field at the sensor array can be compared to the measured values to find the performance of the model. Note that this last step is part of the validation and not of the prediction. The following part gives an overview of the model:

Prediction model:
Input: applied field, onboard sensor data
Output: induced magnetic field

1. Determine initial state $\mathbf{M}_{per}(0)$ and susceptibility distribution, χ.
2. For each iteration k:
   (a) Solve inverse problem to determine induced magnetization $\mathbf{M}_{ind}$ by the applied field and previous permanent magnetization.
   (b) Update permanent magnetization $\mathbf{M}_{per}(k)$:
      i. Compute magnetic field at onboard sensors from previous permanent magnetization, applied field and induced magnetization.
      ii. Calculate difference between computed and measured field at onboard sensors.
      iii. Solve inverse problem to find $\mathbf{M}_{per}$-correction.
      iv. Update the permanent magnetization.
   (c) Determine complete magnetization $\mathbf{M}$ from induced and permanent magnetization.
   (d) Solve forward problem to find magnetic field below the object.

After the mathematical-physical model is developed, the model is implemented in Matlab. Firstly a 3-dimensional CAD model of the object is designed in the program Blender to be able to discretize it, this CAD model is used to generate meshes in Matlab. Then the mathematical-physical model is implemented with and without the regularization methods. Using the MSEM from [22] the magnetic susceptibility distribution of the object is computed. The implemented model is then validated using twin experiments.

3

Magnetism

The following chapter discusses magnetic hysteresis and the derivation of the theoretical model from magnetostatics. From basic magnetostatics equations an integral expression for the reduced field is derived and an integral equation for the induced magnetization is constructed. By solving the integral equation, the induced magnetization from the applied field and permanent magnetization can be computed. First lets introduce two notations, which are used throughout the research: The total magnetization is denoted by $\mathbf{M}$ and the background or applied magnetic field is denoted by $\mathbf{H}_a$.

3.1. Magnetic hysteresis

When ferromagnetic materials are placed in a magnetic field they experience ferromagnetism. Ferromagnetism is nonlinear and shows magnetic hysteresis, a complex phenomenon[3]. Already much research has been done on hysteresis and there are multiple models that can be used to describe this phenomenon. Well known models are the Jiles and Atherton models [14] and the Preisach models [21]. However these models also have their downsides, as for Jiles Atherton models it has been shown that they incorporate some non-physical properties [24]. It is known that hysteresis can be depicted by the well known hysteresis curve. In figure 3.1b a single loop of the hysteresis curve is shown. Here, the start point of the curve is the unmagnetized state, where both $\mathbf{H}_a$ and $\mathbf{M}$ are zero. If the applied field is increased, the magnetization increases until the saturation point is reached (M_s), if the applied field is then brought back to zero, there is residual magnetization (M_r) left, called the permanent magnetization. If in turn a negative field is applied the permanent magnetization decreases again and passes zero at a certain point. In figure 3.1a one can find multiple hysteresis curves, showing how the permanent magnetization can vary due to the applied fields. Note that the hysteresis curves all seem approximately linear close to $\mathbf{H}_a = 0$, which might tell us something about the induced magnetization. As mentioned before the residual magnetization at $\mathbf{H}_a = 0$ is called the permanent magnetization, such that the distance of the curve to the $\mathbf{H}_a$ says something about the permanent magnetization. From these two observations an assumption can be made on how to approximate $\mathbf{M}$ close to $\mathbf{H}_a = 0$. This assumption is further explained in the next section.

3.2. Assumption on M

From the observations in the previous section it seems that magnetization $\mathbf{M}$ can be described by a sum of the induced magnetization and the permanent magnetization. We have seen that the hysteresis curve has a certain linear behaviour around $\mathbf{H}_a = 0$, this can be seen as the approximately linear response of the magnetization to the applied field, describing the induced magnetization. This observation is supported by the Taylor expansion of $\mathbf{M}$ around $\mathbf{H}_a = 0$:

$$\mathbf{M} \cong \mathbf{M}(0) + \frac{\partial \mathbf{M}}{\partial \mathbf{H}}\mathbf{H} + \text{h.o.t.} \tag{3.1}$$

When higher order terms are ignored it can be seen that indeed $\mathbf{M}(\mathbf{H}_a)$ is linear around $\mathbf{H}_a = 0$. The term $\frac{\partial \mathbf{M}}{\partial \mathbf{H}}$ describes the magnetic susceptibility χ. The magnetic susceptibility is a dimensionless material property that indicates the degree of magnetization in response to the applied field and its form is different for anisotropic and isotropic materials. Anisotropic materials do not magnetize in a preferred direction and their

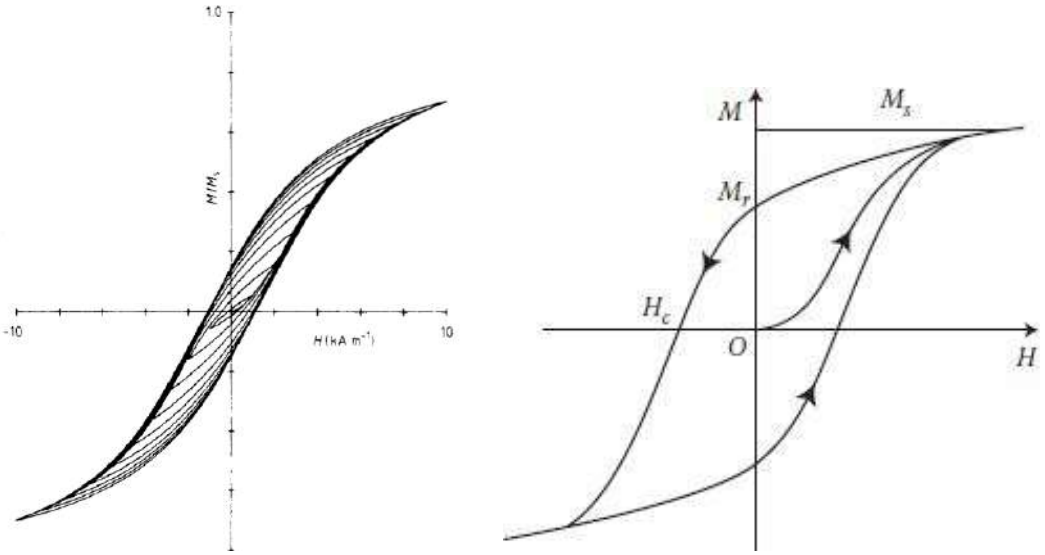

(a) Theoretical hysteresis curves Jiles-Atherton [14] (b) Single Hysteresis curve [18]

Figure 3.1: Hystersis curves

susceptibility is dependent on the orientation dependencies in the material. For these materials the magnetic incremental susceptibility χ_{an} is described by the tensor $\chi_{an} \equiv (\frac{\partial \mathbf{M}}{\partial \mathbf{H}})$. Isotropic materials on the other hand magnetize in a preferred direction and their susceptibility can be described by a scalar quantity χ. In this research it is assumed that the material is isotropic and therefore χ is a scalar quantity. In ferromagnetic materials the susceptibility can vary over time due to external influences, like stress. Since these variations are very small if no large external forces are exerted on the material, we can assume that the susceptibility χ is constant. Note that χ is spatially dependent. Now consider the second observation from the previous section: The distance of the hysteresis curve to the $\mathbf{H}_a$-axis at $\mathbf{H}_a = 0$ can be seen as the contribution of the permanent magnetization. We assume that the permanent magnetization varies slowly linear over time. The distances between the 'linear' parts of the hysteresis curves support this idea.

These observations and results from [20] support the assumption that the induced and the permanent magnetization can be considered separately if $\mathbf{H}_a$ stays relatively close to zero. We have already defined a model to approximate the linear induced magnetization, but we also need a method to approximate the permanent magnetization. In our model we do not work with the named models for the permanent magnetization, but we try a new approach based completely on data-assimilation. With data-assimilation we try to track the changes in the permanent magnetization by considering differences in computed and measured induced magnetic field at onboard sensor locations. From these differences an update on the permanent magnetization is computed each time step.

3.3. Magnetostatics

Now we start with the derivation of the model for the computation of the magnetization $\mathbf{M}$. For this derivation theory on magnetism and magnetostatics from [13] is used. The following assumptions are made: the object of concern is made of isotropic and linearly reacting material and the geometry of the object and the applied field $\mathbf{H}_a$ are known. We also assume that the applied field $\mathbf{H}_a$ is uniform in a certain volume of interest around the object. Following we derive an integral expression for the reduced field and an integral equation for the induced magnetization of an object. The integral equation is expanded to include the separation of the induced and permanent magnetization. The magnetization of the object induces a magnetic field around the object, disturbing the total field $\mathbf{H}$. This influence is called the reduced (or induced) magnetic field $\mathbf{H}_{red}$ and is obviously dependent on $\mathbf{M}$. Due to the linearity in Maxwell's equations (3.4) the following holds for the total field:

$$\mathbf{H} = \mathbf{H}_a + \mathbf{H}_{red}[\mathbf{M}]. \tag{3.2}$$

The linear reaction of our material to an applied field is described by the magnetic susceptibility χ. We assume, as described in the previous section, that the susceptibility is fully known, constant over time, spatially non-uniform and can be described by a scalar quantity. The relation between the induced magnetization and the applied field for isotropic linearly reacting material is given by:

$$\mathbf{M}_{ind} = \chi \mathbf{H}_a. \tag{3.3}$$

For the computation of $\mathbf{H}_{red}$ due to the magnetization of the object the magnetostatic field equations of Maxwell are needed:

$$\begin{cases} \nabla \times \mathbf{H} &= \mathbf{0} \\ \nabla \cdot \mathbf{B} &= 0 \\ \mathbf{B} &= \mu_0(\mathbf{H} + \mathbf{M}) \end{cases} \tag{3.4}$$

Here μ_0 is the magnetic permeability coefficient with a value of $4\pi \cdot 10^{-7} H/m$. Substitution of equation 3.2 in the first equation of Maxwell (3.4) and linearity of fields results in the following equation:

$$\nabla \times (\mathbf{H}_a + \mathbf{H}_{red}) = \nabla \times \mathbf{H}_a + \nabla \times \mathbf{H}_{red} = \mathbf{0}. \tag{3.5}$$

Due to the assumption that $\mathbf{H}_a$ is uniform in a volume around the object, it holds that $\nabla \times \mathbf{H}_a = 0$ reducing equation 3.5 to $\nabla \times \mathbf{H}_{red} = 0$. From this we can conclude that $\mathbf{H}_{red}$ is a rotation-free field. It is known that for each scalar function Φ it holds that $\nabla \times (-\nabla\Phi) = 0$. From this relation and the discovery that $\mathbf{H}_{red}$ is rotation free, it follows that $\mathbf{H}_{red}$ can be described by a potential function:

$$\mathbf{H}_{red} = \nabla \Phi_{red}. \tag{3.6}$$

Now combine the second and third equation from 3.4 and substitute equation 3.6:

$$\nabla \cdot \mathbf{B}_{red} = \nabla \cdot \mu(\mathbf{H}_{red} + \mathbf{M}) \tag{3.7}$$

$$0 = \mu_0(\nabla \cdot \mathbf{H}_{red} + \nabla \cdot \mathbf{M}) \tag{3.8}$$

$$0 = \mu_0(\nabla \cdot (-\nabla\Phi_{red}) + \nabla \cdot \mathbf{M}) \tag{3.9}$$

$$\Delta\Phi_{red} = \nabla \cdot \mathbf{M} \tag{3.10}$$

Following [[13],page 194-197], equations 3.6 and 3.10 can be solved resulting in the following solution for the reduced magnetic field at point $\mathbf{r}$ inside the object:

$$\mathbf{H}_{red}(\mathbf{r}) = -\frac{1}{4\pi} \nabla \iiint_{\Omega} \mathbf{M}(\mathbf{r}') \cdot \frac{|\mathbf{r} - \mathbf{r}'|}{|\mathbf{r} - \mathbf{r}'|^3} d\mathbf{r}' \tag{3.11}$$

With use of general properties for vector inproducts, the Leibniz integration rule and the divergence theorem of Gauss this integral can be rewritten in terms of $(\nabla' \cdot \mathbf{M})$ and $(\mathbf{n}' \cdot \mathbf{M})$:

$$\mathbf{H}_{red}(\mathbf{r}) = -\frac{1}{4\pi} \iiint_{\Omega} \frac{\mathbf{r} - \mathbf{r}'}{|\mathbf{r} - \mathbf{r}'|^3} (\nabla' \cdot \mathbf{M})(\mathbf{r}') d\Omega' + \frac{1}{4\pi} \iint_{\partial\Omega} \frac{\mathbf{r} - \mathbf{r}'}{|\mathbf{r} - \mathbf{r}'|^3} (\mathbf{n}' \cdot \mathbf{M})(\mathbf{r}') dS' \tag{3.12}$$

Note that the magnetization is only present inside the object, outside the object the magnetization $\mathbf{M}$ is zero. Further the normal vector $\mathbf{n}' = \mathbf{n}'(\mathbf{r}')$ points outwards and the differential operator is defined as $\nabla' = [\partial'_x, \partial'_y, \partial'_z]^T$. If we assume the magnetization is only due to induced magnetization ($\mathbf{M} := \mathbf{M}_{ind}$), an integral equation for $\mathbf{M}_{ind}$ can be derived with use of 3.2, 3.3 and 3.12:

$$\mathbf{H} = \mathbf{H}_a + \mathbf{H}_{red}[\mathbf{M}_{ind}]$$

$$\chi\mathbf{H} = \chi\mathbf{H}_a + \chi\mathbf{H}_{red}[\mathbf{M}_{ind}].$$

$$\mathbf{M}_{ind}(\mathbf{r}) + \frac{\chi(\mathbf{r})}{4\pi} \iiint_{\Omega} \frac{\mathbf{r} - \mathbf{r}'}{|\mathbf{r} - \mathbf{r}'|^3} (\nabla' \cdot \mathbf{M}_{ind})(\mathbf{r}') d\Omega' - \frac{\chi(\mathbf{r})}{4\pi} \iint_{\partial\Omega} \frac{\mathbf{r} - \mathbf{r}'}{|\mathbf{r} - \mathbf{r}'|^3} (\mathbf{n}' \cdot \mathbf{M}_{ind})(\mathbf{r}') dS = \chi(\mathbf{r})\mathbf{H}_a \tag{3.13}$$

Now we want to consider permanent magnetization as well as induced magnetization:

$$\mathbf{M} = \mathbf{M}_{per} + \mathbf{M}_{ind}. \tag{3.14}$$

Note that integral 3.11 is a function of $\mathbf{r}$ and that the reduced magnetic field is linear in $\mathbf{M}$. Due to this linearity we can rewrite 3.2 to:

$$\mathbf{H} = \mathbf{H}_a + \mathbf{H}_{red}[\mathbf{M}_{ind}] + \mathbf{H}_{red}[\mathbf{M}_{per}]. \tag{3.15}$$

Remember the assumption that the permanent magnetization and the susceptibility are known before the computation of $\mathbf{M}_{ind}$. Now equations 3.3, 3.12,3.14 and 3.15 can be used to derive a new integral equation for $\mathbf{M}_{ind}$ taking into account the permanent magnetization.

$$\chi\mathbf{H} = \chi\mathbf{H}_a + \chi\mathbf{H}_{red}[\mathbf{M}_{ind}] + \chi\mathbf{H}_{red}[\mathbf{M}_{per}]. \tag{3.16}$$

$$\mathbf{M}_{ind} = \chi\mathbf{H}_a + \chi\mathbf{H}_{red}[\mathbf{M}_{ind}] + \chi\mathbf{H}_{red}[\mathbf{M}_{per}] \tag{3.17}$$

$$\frac{1}{\chi}\mathbf{M}_{ind} - \mathbf{H}_{red}[\mathbf{M}_{ind})] = \mathbf{H}_a + \mathbf{H}_{red}[\mathbf{M}_{per}]. \tag{3.18}$$

The division by χ is allowed, since for ferromagnetic materials it holds that $\chi >> 0$. The integral equation is as follows:

$$\begin{aligned}\frac{1}{\chi}\mathbf{M}_{ind}(\mathbf{r}) + \frac{1}{4\pi}\iiint_\Omega \frac{\mathbf{r}-\mathbf{r}'}{|\mathbf{r}-\mathbf{r}'|^3}(\nabla'\cdot\mathbf{M}_{ind})(\mathbf{r}')d\Omega' - \frac{1}{4\pi}\iint_{\partial\Omega}\frac{\mathbf{r}-\mathbf{r}'}{|\mathbf{r}-\mathbf{r}'|^3}(\mathbf{n}'\cdot\mathbf{M}_{ind})(\mathbf{r}')dS' \\ = \mathbf{H}_a - \frac{1}{4\pi}\iiint_\Omega \frac{\mathbf{r}-\mathbf{r}'}{|\mathbf{r}-\mathbf{r}'|^3}(\nabla'\cdot\mathbf{M}_{per})(\mathbf{r}')d\Omega' + \frac{1}{4\pi}\iint_{\partial\Omega}\frac{\mathbf{r}-\mathbf{r}'}{|\mathbf{r}-\mathbf{r}'|^3}(\mathbf{n}'\cdot\mathbf{M}_{per})(\mathbf{r}')dS'.\end{aligned} \tag{3.19}$$

Note that equation 3.19 contains singularities in point $\mathbf{r}' = \mathbf{r}$ and needs to be reformulated in the numerical computation to avoid these singularities. We consider this in the next chapter.

4

Numerical Forward Model for Magnetostatics

In the previous chapter an integral equation for the induced magnetization was derived from basic magnetostatics. By solving this equation we are able to compute the induced magnetization of an object. For the computation of the induced magnetization, the permanent magnetization has to be known, making it possible to continue with the computation of the total magnetization of the object. In this chapter the numerical forward model for solving integral equation (3.19) is developed. The integral equation is discretized using a finite element method such that the singularities are avoided. We discuss triangular elements and linear basis functions. By solving the forward problem the induced magnetic field can be determined at certain predefined observation points from the magnetization and the applied field.

4.1. The discrete forward model

To define the discrete forward model, first the geometry of the object must be discretized. We introduce a triangulation to discretize the geometry Ω. For the model derivation, we start with 3-dimensional triangular elements and work towards a formulation where 2-dimensional elements can be considered. This is possible if the order of one dimension is small compared to the other dimensions. Define the triangulation $\Omega = \bigcup_{k=1}^{N_e} e_k$ with N_e the number of triangular elements. A generic 3-dimensional triangular element can be seen in figure 4.1. As discussed before the susceptibility χ is constant in time but spatially dependent. The spatial dependency is described by considering a constant χ on each individual element: $\chi = \chi_p$ on e_p. The magnetization can be approximated on each element using an expansion of $\mathbf{M}$ in basis functions. We choose to use linear basis functions defined by $\varphi_i(\mathbf{v}_j) = \delta_{ij}$, for $i, j = 1,2,3$, where v_1, v_2, v_3 are the vertices of the triangle. More on (linear) basis functions can be found in [17]. The approximation of the magnetization at point $\mathbf{r}$ in element e, $(\mathbf{M}_e)$ is then given by:

$$(\mathbf{M})_e(\mathbf{r}) = \sum_{p=1}^{3} \mathbf{M}_p \phi_p(\mathbf{r}), \tag{4.1}$$

where $\mathbf{M}_p$ is magnetization at the vertices $\mathbf{v}_1, \mathbf{v}_2, \mathbf{v}_3$ of the triangular element.

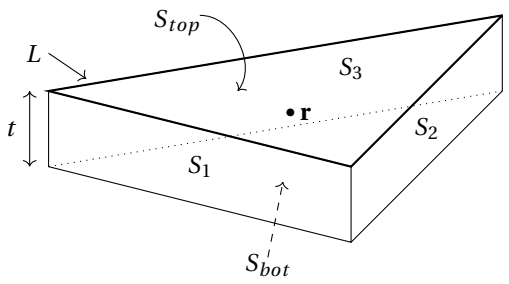

Figure 4.1: A typical triangular element in a mesh of Ω

4.1.1. Linear basis functions

We take a closer look at the basis functions ϕ_i, since only linear basis functions are taken they can be written as

$$\varphi_i(x,y,z) = a_i x + b_i y + c_i z + d_i, (i = 1,2,3). \tag{4.2}$$

In an element each basis function is known in three different points, namely the three vertices of the triangular elements. Each of the linear basis functions is equal to 1 on one of the vertices and is zero on the other two. E.g. basis function φ_1 is one on vertex v_1 and zero on v_2 and v_3. Note that by definition on each vertex only one basis function can be equal to one. Evaluation of basis function φ_1, described by equation 4.2, in all three vertices of the element results in three equations:

$$\begin{bmatrix} v_{1x} & v_{1y} & v_{1z} & 1 \\ v_{2x} & v_{2y} & v_{2z} & 1 \\ v_{3x} & v_{3y} & v_{3z} & 1 \end{bmatrix} \begin{bmatrix} a_1 \\ b_1 \\ c_1 \\ d_1 \end{bmatrix} = \begin{bmatrix} 1 \\ 0 \\ 0 \end{bmatrix}, \tag{4.3}$$

where v_{ix} denotes the x-coordinate of the i^{th} vertex. If this evaluation is repeated for the remaining two basis functions of the element, we find the resulting system of equations. Note that the system contains three equations for four unknowns and is therefore inconsistent.

$$\begin{bmatrix} \mathbf{v}_1 & 1 \\ \mathbf{v}_2 & 1 \\ \mathbf{v}_3 & 1 \end{bmatrix} \begin{bmatrix} a_i \\ b_i \\ c_i \\ d_i \end{bmatrix} = \begin{bmatrix} 1 & 0 & 0 \\ 0 & 1 & 0 \\ 0 & 0 & 1 \end{bmatrix} \tag{4.4}$$

To achieve a consistent system, an additional equation is needed. This extra equation should give a certain relationship between a_i, b_i and c_i. In order to find this condition consider an element in the xy-plane. Since the element has a fixed z-coordinate, the linear basis functions are now of the form $\varphi_i(x,y,z) = a_i x + b_i y + d_i (i = 1,2,3)$. Comparison to 4.2 results in the condition $c_i = 0$. We find the same condition for a_i and b_i if the element is in the yz- or xz-plane respectively. This condition can be added to the system by considering the equation:

$$\nabla\varphi \cdot \mathbf{n} = 0,$$

where $\mathbf{n}$ is the normal to the element. If the element is in the xy-plane, the normal is $[0,0,\pm 1]^T$ resulting in the equation $a_i \cdot 0 + b_i \cdot 0 + c_i \cdot (\pm)1 = 0$, which gives exactly the wanted condition $c_i = 0$. It can be seen that this equation also gives the proper conditions for a_i and b_i in the cases the element is located in the yz- or xz-plane. Note that the equation $\nabla\varphi \cdot \mathbf{n} = 0$ gives a relationship between a_i, b_i, c_i for arbitrary elements, not located in the xy-,yz-,xz-plane, as well. Adding this equation to our systems always results in the following consistent system:

$$\begin{bmatrix} \mathbf{v}_1 & 1 \\ \mathbf{v}_2 & 1 \\ \mathbf{v}_3 & 1 \\ \mathbf{n} & 0 \end{bmatrix} \begin{bmatrix} a \\ b \\ c \\ d \end{bmatrix} = \begin{bmatrix} 1 & 0 & 0 \\ 0 & 1 & 0 \\ 0 & 0 & 1 \\ 0 & 0 & 0 \end{bmatrix} \tag{4.5}$$

System 4.5 has full rank and is thus a consistent system which can always be solved uniquely.

4.1.2. Expansions of M

Using the expansion of $\mathbf{M}$ in the basis functions (eq. 4.1), the divergence of $\mathbf{M}$ and the flux can be approximated by the evaluation in the vertices of the element:

$$(\nabla' \cdot \mathbf{M})_e(\mathbf{r}') = \sum_{p=1}^{3} \mathbf{M}_p \cdot \nabla' \varphi_p(\mathbf{r}') \tag{4.6}$$

$$(\mathbf{n}' \cdot \mathbf{M})_e(\mathbf{r}') = \sum_{p=1}^{3} (\mathbf{n}' \cdot \mathbf{M}_p) \varphi_k(\mathbf{r}') \tag{4.7}$$

Using the triangulation and the approximations of $\mathbf{M}$, integral equation 3.19 is reduced to the following finite-dimensional system of equations:

$$\frac{1}{\chi(\mathbf{r})}\mathbf{M}^{ind}(\mathbf{r}) + \frac{1}{4\pi}\sum_e \iiint_e \frac{\mathbf{r}-\mathbf{r}'}{|\mathbf{r}-\mathbf{r}'|^3}(\nabla'\cdot\mathbf{M}^{ind})_e(\mathbf{r}')\mathrm{d}\mathbf{r}' - \frac{1}{4\pi}\sum_{be}\iint_{be}\frac{\mathbf{r}-\mathbf{r}'}{|\mathbf{r}-\mathbf{r}'|^3}(\mathbf{n}'\cdot\mathbf{M}^{ind})_{be}(\mathbf{r}')\mathrm{d}\mathbf{r}'$$
$$= \mathbf{H}_0 - \frac{1}{4\pi}\sum_e \iiint_e \frac{\mathbf{r}-\mathbf{r}'}{|\mathbf{r}-\mathbf{r}'|^3}(\nabla'\cdot\mathbf{M}^{per})_e(\mathbf{r}')\mathrm{d}\mathbf{r}' + \frac{1}{4\pi}\sum_{be}\iint_{be}\frac{\mathbf{r}-\mathbf{r}'}{|\mathbf{r}-\mathbf{r}'|^3}(\mathbf{n}'\cdot\mathbf{M}^{per})_{be}(\mathbf{r}')\mathrm{d}\mathbf{r}' \quad (4.8)$$

When the expansion of $\mathbf{M}$ (eq. 4.1) is substituted and a point evaluation method is used it can be observed that above equation is linear in $\mathbf{M}_{ind}$ and can be written as the following matrix system:

$$\left[\sum_{i=1}^{N_e}\frac{1}{\chi_i}D_i + A + B\right]\mathbf{M}_{ind} = \mathbf{H}_a - [A+B]\,\mathbf{M}_{per}. \quad (4.9)$$

From this equation it can be seen directly that $\mathbf{M}_{ind}$ can be directly computed from $\mathbf{H}_a$ and $\mathbf{M}_{per}$ if the matrices A, B, D_i are known. In the next subsections all matrix entries are computed.

4.1.3. Computation of the matrix entries

We use a collocation method with three evaluation points inside each element to solve this integral equation in each element. To find the correct entries for the matrices we consider one fixed element e_j and one evaluation point $\mathbf{w} \in e_i$ in which we evaluate the integral equation. Matrix equation 4.9 can be written as:

$$\begin{aligned} D(e_j,\mathbf{w})(\hat{\mathbf{M}}_{ind}) + \sum_{e_j} A(e_j,\mathbf{w})(\hat{\mathbf{M}}_{ind})_{e_j} + \sum_{be_j} B(be_j,\mathbf{w})(\hat{\mathbf{M}}_{ind})_{be_j} \\ = \mathbf{H}_0 - \sum_{e_j} A(e_j,\mathbf{w})(\mathbf{M}_{per})_{e_j} + \sum_{be_j} B(be_j,\mathbf{w})(\mathbf{M}_{per})_{be_j} \end{aligned} \quad (4.10)$$

Note that the estimate $\hat{\mathbf{M}}_{ind}$ contains 9 unknowns in total, the magnetization in three directions for all three vertices of the element. These are ordered according to the order of the vertices in the list of vertices P. Considering the left hand side of this equation in three separate parts results in the following expressions for the matrices:

$$D(e,\mathbf{r}) = \frac{1}{\chi(\mathbf{r})}\varphi_k(\mathbf{r}).$$
$$A(e,\mathbf{r}) = \frac{1}{4\pi}\iiint_e \frac{\mathbf{r}-\mathbf{r}'}{|\mathbf{r}-\mathbf{r}'|^3}\mathrm{d}\mathbf{r}'(\nabla\varphi_k)_t$$
$$B(be,\mathbf{r}) = -\frac{1}{4\pi}(\mathbf{n}')\iint_{be}\frac{\mathbf{r}-\mathbf{r}'}{|\mathbf{r}-\mathbf{r}'|^3}\varphi_k(\mathbf{r})\mathrm{d}\mathbf{r}'$$

Bear in mind that $D(e,\mathbf{r})$, $A(e,\mathbf{r})$ and $B(e,\mathbf{r})$ are $3\times|P|$ matrices and that both D and A are evaluated for all three vertices of the element and B is only evaluated for the two vertices of the boundary element .

Computation of $D(e,\mathbf{r})$

The computation of the entries of $D(e,\mathbf{r})$ are rather straightforward. The value of $\chi(\mathbf{r})$ is known, so the only difficulty is the evaluation of $\varphi_\ell(\mathbf{r})$ for $\ell = 1,2,3$. The basis functions were defined as $\varphi_\ell(\mathbf{v}_j) = \delta_{\ell j}$ for the vertices $\mathbf{v}_j$ of the element. The point $\mathbf{r}$ can be written as a linear combination of the vertices of the element: $\mathbf{r} = \alpha\mathbf{v}_1 + \beta\mathbf{v}_2 + \gamma\mathbf{v}_3$. Then it holds for the linear basis functions that:

$$\varphi_\ell(\mathbf{r}) = \varphi_\ell(\alpha\mathbf{v}_1) + \varphi_\ell(\beta\mathbf{v}_2) + \varphi_\ell(\gamma\mathbf{v}_3)$$

In this way all entries for $D(e,\mathbf{r})$ can be computed.

Computation of $A(e,\mathbf{r})$

The entries *of* $A(e,\mathbf{r})$ are expressed in terms derived from

$$\frac{1}{4\pi}\iiint_e \frac{\mathbf{r}-\mathbf{r}'}{|\mathbf{r}-\mathbf{r}'|^3}\mathrm{d}\mathbf{r}'\nabla\varphi_l. \quad (4.11)$$

Next we give an outline of the method used to compute the entries of matrix $A(e,\mathbf{r})$ analytically. We study two different cases: one where $\mathbf{r} \in e_j$, which is the difficult case due to the singularity $\mathbf{r} = \mathbf{r}'$, and the case

$\mathbf{r} \notin e_j$, which does not contain a singularity. For the case with the singularity, a limit argument is used to find a solution. We evaluate the integral on the element except a ball with small radius $\varepsilon > 0$ around $\mathbf{r}$. Since the singularity is not included, the integrand is smooth. Now a corollary of the divergence theorem is used:

$$\iiint_V \nabla\psi dV = \oiint \psi \mathbf{n} dS, \tag{4.12}$$

for any smooth ψ, where $\mathbf{n}$ is the outward normal. After using this corollary and taking the limit $\varepsilon \downarrow 0$, we find that:

$$\iiint_e \frac{\mathbf{r}-\mathbf{r}'}{|\mathbf{r}-\mathbf{r}'|^3} dS = \iint_{\partial e} \frac{1}{|\mathbf{r}-\mathbf{r}'|} \mathbf{n}' dS'. \tag{4.13}$$

The boundary of our element consists of five faces, see figure 4.1. For the three side faces, S_1, S_2, S_3 it can be observed that:

$$\iiint_{S_1+S_2+S_3} \frac{1}{|\mathbf{r}-\mathbf{r}'|} \mathbf{n}' dS' \approx t \int_L \frac{1}{|\mathbf{r}-\mathbf{r}'|} \mathbf{n}' dL', \tag{4.14}$$

since $\mathbf{r}' \mapsto \frac{1}{|\mathbf{r}-\mathbf{r}'|}$ is approximately constant in the normal direction.

For the top and bottom plate we find that these cancel out due to the small t. Application of a suitable transformation on the three edges of L transforms the integral into an integral over the interval [-1,1] and we find that:

$$\begin{aligned}\iiint_e \frac{\mathbf{r}-\mathbf{r}'}{|\mathbf{r}-\mathbf{r}'|^3} \mathrm{d}S &= t \int_L \frac{1}{|\mathbf{r}-\mathbf{r}'|} \mathbf{n}' \mathrm{d}L' \\ &= t \sum_{p=1}^{3} \frac{|L_p|}{2} \mathbf{n}'_p \int_{-1}^{1} \frac{1}{|\mathbf{r}-\mathbf{r}'_p(u)|} \mathrm{d}u\end{aligned}$$

This integral can be computed analytically, since it is of the form:

$$\int_{-1}^{1} \frac{1}{\sqrt{(a+bx)^2+(c+dx)^2+(e+fx)^2}} \mathrm{d}x. \tag{4.15}$$

The parameters a, b, c, d, e, f depend on one of the line faces L_p. This analytical solution for this integral is:

$$\begin{aligned}\int \frac{1}{\sqrt{(a+bx)^2+(c+dx)^2+(e+fx)^2}} \mathrm{d}x = \frac{1}{\sqrt{b^2+d^2+f^2}} \times \log\Big[\sqrt{b^2+d^2+f^2} \\ \times\sqrt{(a+bx)^2+(c+dx)^2+(e+fx)^2} + b(a+bx)+d(c+dx)+f(e+fx).\Big]\end{aligned}$$

However care must be taken, since this solution is only valid if not more than two of the parameters a, b, c, d, e, f are zero. In case of more than two zeros we need the analytical solution to:

$$\int_{-1}^{1} \frac{1}{a^2+c^2+e^2} dx \text{ or } \int_{-1}^{1} \frac{1}{(bx)^2+(dx)^2+(fx)^2} dx \text{ or } \int_{-1}^{1} \frac{1}{(a+bx)^2} dx, \tag{4.16}$$

dependent on the combination of zeros. Fortunately these are basic integrals with a simple analytical solution.

For the case where $\mathbf{r} \notin e_j$ the same approach can be used without the limit argument.

Computation of $B(e, \mathbf{r})$

Again we give an outline of the methodology used for the computation of the entries. For this computation we need to consider integrals of the form:

$$\iint_{be} \frac{r_x - r'_x}{|\mathbf{r}-\mathbf{r}'|^3} \varphi_k(\mathbf{r}') \mathrm{d}\mathbf{r}', \qquad \iint_{be} \frac{r_y - r'_y}{|\mathbf{r}-\mathbf{r}'|^3} \varphi_k(\mathbf{r}') \mathrm{d}\mathbf{r}' \qquad \iint_{be} \frac{r_z - r'_z}{|\mathbf{r}-\mathbf{r}'|^3} \varphi_k(\mathbf{r}') \mathrm{d}\mathbf{r}' \tag{4.17}$$

We only focus on the first integral as the other two can be done analogously. Fortunately, there are no singularities in the integral, simplifying the computation. Again we can approximate the integral, due to the small thickness t:

$$\iint_{be} \frac{r_x - r'_x}{|\mathbf{r}-\mathbf{r}'|^3} \varphi(\mathbf{r}') \mathrm{d}\mathbf{r}' = t \int_{L_{be}} \frac{r_x - r'_x}{|\mathbf{r}-\mathbf{r}'|^3} \varphi(\mathbf{r}')_k \mathrm{d}\mathbf{r}'. \tag{4.18}$$

We parametrize the line element L_{be} with vertices $\mathbf{v}_1$ and $\mathbf{v}_2$ over the interval [-1,1] via

$$\mathbf{r}'(s) = \frac{1}{2}(\mathbf{v}_1 + \mathbf{v}_2) + \frac{1}{2}s(\mathbf{v}_2 - \mathbf{v}_1), \quad s \in [-1, 1] \tag{4.19}$$

Now the integral can be transformed, using this parametrization:

$$t\int_{L_{be}} \frac{r_x - r'_x}{|\mathbf{r} - \mathbf{r}'|^3}\varphi_k(\mathbf{r}')\mathrm{d}\mathbf{r}' = \frac{t|L_{be}|}{2}\int_{-1}^{1} \frac{r_x - r'_x(s)}{|\mathbf{r} - \mathbf{r}'(s)|^3}\varphi_k(\mathbf{r}'(s))\mathrm{d}s \tag{4.20}$$

Note that the linear basis function $\phi_k(\mathbf{r}'(t))$ is now a basis function $u(t)$ on [-1,1] and can be written as: $u_k(s) = \frac{1}{2} + \frac{1}{2}(-1)^k s \quad (k = 1, 2)$. Using this expression for u_k we can split the integral into two separate integrals.

$$\begin{aligned}\frac{t|L_{be}|}{2}\int_{-1}^{1} \frac{r_x - r'_x(s)}{|\mathbf{r} - \mathbf{r}'(s)|^3}\varphi_k(\mathbf{r}'(s))\mathrm{d}s &= \frac{t|L_{be}|}{4}\int_{-1}^{1} \frac{r_x - r'_x(s)}{|\mathbf{r} - \mathbf{r}'(s)|^3}\mathrm{d}s + (-1)^k\frac{t|L_{be}|}{4}\int_{-1}^{1} \frac{(r_x - r'_x(s))s}{|\mathbf{r} - \mathbf{r}'(s)|^3}\mathrm{d}s \\ &= \frac{t|L_{be}|}{4} \times A + (-1)^k\frac{t|L_{be}|}{4} \times B\end{aligned}$$

These two integrals are both of a form that can be computed analytically. For integral A we have

$$\int \frac{(a + bs)}{\sqrt{(a + bs)^2 + (c + ds)^2 + (e + fs)}^3}\mathrm{d}s = \frac{d_1(s)}{e_1(s)} + \text{constant} \tag{4.21}$$

and for integral B

$$\int \frac{(a + bs)s}{\sqrt{(a + bs)^2 + (c + ds)^2 + (e + fs)^2}^3}\mathrm{d}s = \frac{d_2(s)}{e_2(s)} + \frac{d_3(s)}{e_3(s)} + \text{constant}. \tag{4.22}$$

with:

$$\begin{aligned}d_1(s) &= a\Big(cd + ef + (d^2 + f^2)s\Big) - b\Big(c(c + ds) + e(e + fs)\Big) \\ e_1(s) &= \Big(b^2(c^2 + e^2) + (de - cf)^2 - 2ab(cd + ef) + a^2(d^2 + f^2)\Big) \\ &\quad \times \sqrt{(a + bs)^2 + (c + ds)^2 + (e + fs)^2} \\ d_2(s) &= -\Big(a^2 + c^2 + e^2\Big)\Big(-b(cd + ef) + a(d^2 + f^2)\Big) - \Big[b^3(c^2 + e^2) - 3ab^2(cd + ef) \\ &\quad + a(cd + ef)(d^2 + f^2) + b\Big[2a^2(d^2 + f^2) \\ &\quad - \Big(e(-d + f) + c(d + f)\Big)\Big(c(d - f) + e(d + f)\Big)\Big]\Big]s\end{aligned}$$

$$\begin{aligned}e_2(s) &= \Big(b^2 + d^2 + f^2\Big)\Big(b^2(c^2 + e^2) + (de - cf)^2 - 2ab(cd + ef) + a^2(d^2 + f^2)\Big) \\ &\quad \times \sqrt{(a + bs)^2 + (c + ds)^2 + (e + fs)^2}\end{aligned}$$

$$\begin{aligned}d_3(s) &= b\log\Big(ab + cd + ef + (b^2 + d^2 + f^2)s + \sqrt{b^2 + d^2 + f^2} \\ &\quad \times \sqrt{(a + bs)^2 + (c + ds)^2 + (e + fs)^2}\Big)\end{aligned}$$

$$e_3(s) = (b^2 + d^2 + f^2)^{3/2}$$

Again care must be taken since these exact solutions are not valid for certain combinations of zeros for a, b, c, d, e, f. For the geometry used in our research the analytical solutions are valid.

4.1.4. Computation of the normal vectors

In the computation of A(e,**r**) and B(e,**r**) the normal vectors are important. For each element the normal vectors must be defined in the outward direction. Here we describe the method used to achieve that in each case the outward normal is used. In figure 4.2 an element is shown with its center and the normal vector on one boundary element. The center **c** is computed as $\frac{1}{3}(\mathbf{v}_1+\mathbf{v}_2+\mathbf{v}_3)$ and the point $\mathbf{c}_m$ is computed by $\frac{1}{2}(\mathbf{v}_1+\mathbf{v}_2)$. The vector between **c** and $\mathbf{c}_m$ is named $c_c = \mathbf{c}-\mathbf{c}_m$. Since $\mathbf{n}'$ is in the same 2-dimensional plane as the independent vectors $\mathbf{v}_1-\mathbf{v}_2$ and $\mathbf{v}_3-\mathbf{v}_1$, we write $\mathbf{n}'$ as a linear combination of those two: $\mathbf{n}' = c_1(\mathbf{v}_2-\mathbf{v}_1)+c_2(\mathbf{v}_3-\mathbf{v}_1)$. For convenience we write $\mathbf{n}' = c_1\mathbf{a}+c_2\mathbf{b}$.

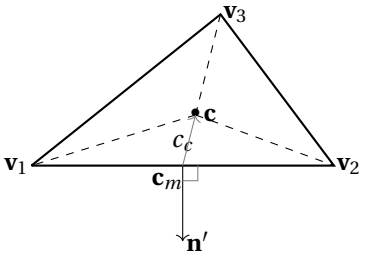

Figure 4.2: Element with center c and normal vector $\mathbf{n}'$

The outward normal vector must satisfy two conditions. Firstly it must be perpendicular to the vector $\mathbf{v}_1-\mathbf{v}_2$ and secondly it must be in the opposite direction of c_c. These can be written as the following two inproducts:

$$\mathbf{n}'\cdot(\mathbf{v}_2-\mathbf{v}_1) = 0 \tag{4.23}$$

$$\mathbf{n}'\cdot c_c = -1 \tag{4.24}$$

From the first condition it follows that:

$$\mathbf{n}'\cdot(\mathbf{v}_2-\mathbf{v}_1) = (c_1\mathbf{a}+c_2\mathbf{b})\cdot\mathbf{a} = c_1\parallel\mathbf{a}\parallel^2 + c_2(\mathbf{a}+\mathbf{b}) = 0. \tag{4.25}$$

The second condition results in $\begin{bmatrix}\mathbf{a}\cdot\mathbf{c} & \mathbf{b}\cdot\mathbf{c}\end{bmatrix} = -1$. Combining the two conditions results in the following system that needs to be solved:

$$\begin{bmatrix}\parallel\mathbf{a}\parallel^2 & \mathbf{a}\cdot\mathbf{b}\\ \mathbf{a}\cdot c_c & \mathbf{b}\cdot c_c\end{bmatrix}\begin{bmatrix}c_1\\ c_2\end{bmatrix} = \begin{bmatrix}0\\ -1\end{bmatrix} \tag{4.26}$$

When c_1 and c_2 are computed the normal vector is known and only needs to be normalized to find the unitary outward normal vector: $\mathbf{n}' = \frac{\mathbf{n}'}{\|\mathbf{n}'\|}$.

Remark: For three dimensional objects care must be taken in the implementation of the normal vectors, since one boundary element can have different orientations of the outward normal. This is the case if the boundary element is contained in two elements which make an angle.

4.2. Forward computation to the sensor positions

All of the sensor positions, inside the box and on the array, are known. Note that if the expansions of the basis functions are used, equation 3.12 is linear in $\mathbf{M}$ and the integrals only depend on the sensor position $\mathbf{r}_c$. The position is known for each sensor and is naturally equal in each iteration. Therefore the forward computation of $\mathbf{H}_{red}$ by solving the integral equation 3.12 can be simplified to the matrix equation

$$\mathbf{H}_{red}(\mathbf{r}_c) = C(\mathbf{r}_c)\mathbf{M} \tag{4.27}$$

where r_c is the position of a sensor, $\mathbf{H}_{red}(r_c)$ is the magnetic field at the sensor due to the magnetization and $C(r_c)$ is the field matrix. The field matrix $C(r_c)$ can be obtained by using the discretization from the previous chapter and the evaluation at an arbitrary observation point in integral equation 3.12.The reduced magnetic field needs to be computed during each iteration of the prediction model. Being able to use the same matrix every time drastically decreases the computational time. Therefore we compute the field matrices C_1 and C_2. The matrix C_1 is constructed such that it is able to compute the induced magnetic field $\mathbf{B}_c^{arr}$ at all sensors locations on the sensor array. Matrix C_2 is constructed such that it computes the magnetic induced magnetic field at the onboard sensor positions. The total magnetic induction field is given by:

$$\mathbf{B}_c^{arr} = \mathbf{B}_0^{arr} + \mathbf{B}_{red}^{arr}$$

with $\mathbf{B}_{red}^{arr} = \mu_0 C_1 \mathbf{M}$. Note that in our data the contribution of $\mathbf{B}_0^{arr}$ is directly filtered leaving us with $\mathbf{B}_c^{arr} = \mathbf{B}_{red}^{arr} = \mu_0 C_1 \mathbf{M}$. For simplicity in the notation we use $\mathbf{B}_c^{arr}$ in the research to denote $\mathbf{B}_{red}^{arr}$. For the construction of C_1 the integral equation 3.12 is evaluated for all sensors at the array and is multiplied with μ_0 to compute $\mathbf{B}^{arr}$ instead of $\mathbf{H}^{arr}$. This matrix is saved and can be used for each forward computation from $\mathbf{M}$ to the sensor array. The same can be done for matrix C_2, which is used for the forward computation to the onboard sensors.

Remark: In the following chapters we denote by $\mathbf{M}$ the numerical vector used in the designed matrix formed model.

5

Inverse problems

The purpose of this chapter is to explain the basic theory behind inverse problems. First general definitions of inverse problems and properties like ill-conditioned are explained. We review some of the difficulties related to solving inverse problems and a few solutions on how to cope with these difficulties. Methods like the (generalized) singular value decomposition and Tikhonov regularization are discussed.

5.1. Inverse problem formulation

Lets start with a basic linear system:

$$A\mathbf{x} = \mathbf{b} \text{ with } A \in \mathbb{R}^{m\times n}, \mathbf{x} \in \mathbb{R}^n, \mathbf{b} \in \mathbb{R}^m. \tag{5.1}$$

We assume that the model matrix A is completely known. Now if the input $\mathbf{x}$ is known the computation of the output $\mathbf{b}$ can be done by simply multiplying A and $\mathbf{x}$. The formulation of computing the output from the input is called the forward problem. If on the other hand the output $\mathbf{b}$ is known and the input $\mathbf{x}$ is unknown, we are speaking of an inverse problem. Note that we also speak of an inverse problem in the case where both the input and the output are known, but the system is unknown. For now we only focus on inverse problems where the system and the output are known. In practice we often come across problems where external information or measurements are available and the internal structure is unknown. From basic linear algebra it is known that if A is an invertible square matrix, the inverse problem can be solved by computation of $\mathbf{x} = A^{-1}\mathbf{b}$. Unfortunately in nearly all practical problems the matrix A is not square nor invertible. From the desire to be able to solve these problems many studies have been conducted on the properties of inverse problems and methods to achieve accurate approximations of the solution. First we look at a few properties and definitions related to inverse problems. The class of inverse problems belongs to the larger class of *ill-posed* problems. Logically, ill-posed problems are problems which do not satisfy the conditions of a well-posed problem. According to Hadamard a mathematical problem is well-posed if it satisfies each of the following three requirements [6]:

- **Existence:** The problem must have a solution.
- **Uniqueness:** There must be only one solution to the problem.
- **Stability:** The solution must depend continuously on the data.

The first two requirements speak for themselves as to why they are important for well-posed problems. The third condition is less intuitive, but certainly not less important. This condition prevents that small perturbations in the data $\mathbf{b}$ result in large perturbations in the solution $\mathbf{x}$. Assume that matrix A is not invertible, then the system can be either *underdetermined* or *overdetermined*. If the system is overdetermined there are more equations than unknowns after linear dependencies between equations have been removed. An overdetermined system often has no solutions since there are more restrictive equations than unknowns. Overdetermined systems are ill-posed since they do not satisfy the first condition. If a system has less equations than unknowns, it is called underdetermined. There are now unknowns left in $\mathbf{x}$ which are not determined by the equations. Underdetermined systems often have an infinite number of solutions and therefore do not satisfy the second condition. Problems which do not satisfy the third requirement often have so called

ill-conditioned matrices. Violations of the first requirement can often be fixed by a slight reformulation of the problem. A well-known method to reformulate the problem is by considering the least squares problem instead:

$$\min_x \| A\mathbf{x} - \mathbf{b} \|_2^2$$

With addition of extra requirements violations of the second requirement can often be solved. If the additional requirements are chosen carefully, the solution becomes unique. Violations of the third requirement are harder to deal with, since the problem must be reformulated in such a way that the solution to the new problem is less sensitive to perturbations. A well-known method to solve the violation of the stability criterion is regularization. The sensitivity of solutions to perturbations are often caused by *ill-conditioned* matrices. Matrices are considered to be ill-conditioned if they have a high condition number ($> 10^3$). The condition number of a matrix is defined by its smallest and largest singular value:

$$\text{cond}(A) = \frac{\sigma_l}{\sigma_s}, \tag{5.2}$$

where σ_l is the largest singular value and σ_s is the smallest singular value. To see that high condition numbers lead to high sensitivity consider the exact and perturbed solutions, $\mathbf{x}^{exact}$ and $\mathbf{x}$, these solutions satisfy:

$$A\mathbf{x}^{exact} = \mathbf{b}^{exact}, A\mathbf{x} = \mathbf{b}^{exact} + e, \tag{5.3}$$

with e the perturbation of the right-hand side. From the classical perturbation theory the following bound is found for the error between the solution and the exact solution [6]:

$$\frac{\| \mathbf{x}^{exact} - \mathbf{x} \|_2}{\| \mathbf{x}^{exact} \|_2} \leq \text{cond(A)} \frac{\| e \|_2}{\| \mathbf{b}^{exact} \|_2}, \tag{5.4}$$

with cond(A) the condition number of A. From this bound it can easily be seen that a large condition number implies that the found solution can be far from the exact solution, which is highly undesirable. It can also be observed that for ill-conditioned problem a small residual does not necessarily imply that the perturbed solution is close to the exact solution. The problem behaves like an undetermined problem and as noted before these solutions can be improved by supplying additional information. To improve both unwanted observations we look at regularization, a common method to improve solutions of ill-conditioned problems. With regularization we impose an extra condition or regularity on the solution of the inversion in order to reduce the solution space and suppress unwanted noise components. Although there are many regularization methods, we focus on one of the most successful methods, the Tikhonov regularization, see also [2], [6].

5.2. Singular value decomposition

First a recap of the standard singular value decomposition (SVD) is given from which the reason for regularization is shown. Then we turn to the generalized singular value decomposition, since this decomposition can give more insight in the Tikhonov regularization. Remember that the SVD computes the following factorization of matrix $A \in \mathbb{R}^{m \times n}$ with $m \leq n$:

$$A = U\Sigma V^T = \sum_{i=1}^{n} u_i \sigma_i v_i^T, \tag{5.5}$$

where

$$\Sigma \in \mathbb{R}^{n \times n} = \text{diag}(\sigma_1, ..., \sigma_n), \quad \sigma_1 \leq \sigma_2 \geq ... \geq 0.$$

The matrices U and V are orthonormal matrices consisting of the left and right singular vectors respectively. It holds that

$$A^{-1} = V\Sigma^{-1}U^T.$$

Using this inverse of A an expression for the naive solution an be determined:

$$\mathbf{x} = A^{-1}\mathbf{b} = \sum_{i=1}^{n} \frac{u_i^T \mathbf{b}}{\sigma_i} v_i. \tag{5.6}$$

From this equation it is evident that if $\mathbf{b}$ contains noise these noise factors are largely amplified by small singular values. Notice that the condition number of A is large if it smallest singular values are very small

compared to the highest singular value. This observation supports the observation that a high condition number implies a higher sensitivity to perturbation.

The generalized singular value decomposition is a matrix decomposition more general than the singular value decomposition (SVD) since it can give a decomposition of two matrices with the same number of columns. The need for this extra property is given in the next section. First we give a short introduction on this decomposition. For more detailed descriptions and derivations, see [19],[6],[16]. Name $Y^T = [A^T, R^T]$ and rank(Y) = r. The GSVD of the matrix $A(m \times n)$ and matrix R $(p \times n)$ with $m > n$ is given by the factorizations:

$$A = U\Sigma_1[W^T X, 0]Q^T \quad \text{and} \quad R = V\Sigma_2[W^T X, 0]Q^T. \tag{5.7}$$

The following statements hold for the matrices in the factorizations:

1. U $[m \times m]$, V $[p \times p]$, W $[r \times r]$, Q $[n \times n]$ are orthogonal matrices. U and V hold the orthonormal left singular vectors for both matrices and Q holds the right singular vectors. The right singular vectors are linearly independent but not normalized or orthogonal.

2. X $[r \times$ r] is nonsingular with singular values equal to the nonsingular values of Y.

3. Σ_1 [m × r] and Σ_2 [p × r] are of the form:

$$\Sigma_1 = \begin{pmatrix} I_1 & & \\ & S_1 & \\ & & O_1 \end{pmatrix}, \quad \Sigma_2 = \begin{pmatrix} O_2 & & \\ & S_2 & \\ & & I_1 \end{pmatrix}, \tag{5.8}$$

   with $S_1 = \text{diag}(\sigma_{k+1}, ..., \sigma_{k+s}$ and $S_2 = \text{diag}(\mu_{k+1}, ..., \mu_{k+s})$ are real $s \times s$ matrices. Further I_1, I_2 are unit matrices and O_1 and O_2 are zero matrices, possibly with no rows or no columns. Further it holds that $1 \geq \sigma_{k+1} \geq ... \geq \sigma_{k+s} \geq 0$, $0 \leq \mu_{k+1} \leq ... \leq \mu_{k+s} \leq 1$ and $\sigma_i^2 + \mu_i^2 = 1$ for $i = k+1, ..., k+s$.

The ratio's σ_i / μ_i are called the generalized singular values. The generalized singular vectors also satisfy the following relations:

$$\begin{array}{lllll} p < n & C_2 q_i = \sigma_i u_i, & Rq_i = \mu_i v_i, & i = 1, ..., p, \\ & C_2 q_i = u_i, & Rq_i = 0, & i = p+1, ..., n, \\ p \geq n: & C_2 q_i = \sigma_i u_i, & Rq_i = \mu_i v_i, & i = 1, ..., n. \end{array} \tag{5.9}$$

5.3. Tikhonov regularization

Now lets focus on the well-known regularization method, Tikhonov regularization. Tikhonov regularization has the advantage on other methods that it is better suited for large computational problems and that it explicitly incorporates the regularity requirement in the formulation of the problem [6]. Tikhonov regularization replaces the ill-conditioned problem

$$\min_{\mathbf{x}} \| A\mathbf{x} - \mathbf{b} \|_2^2 \tag{5.10}$$

with the nearby problem

$$\min_{\mathbf{x}} \{ \| A\mathbf{x} - \mathbf{b} \|_2^2 + \lambda^2 \| R\mathbf{x} \|_2^2 \}. \tag{5.11}$$

Here λ is a positive regularization parameter which weights both parts of the criterion function and R is the regularization operator which adds a certain requirement to the solution. The first part of the criterion, $\| A\mathbf{x} - \mathbf{b} \|_2^2$ describes the fit of the solution on the data and therefore tells something on how well the solution resembles the data. The second part is a penalty term that describes the required regularity. Naturally we want a good combination between both parts, a completely smooth solution which does not fit the data is not preferred, as is a solution which fits the data but does not satisfy the expected regularity at all. The balance between both parts is defined by the parameter λ^2. There are many methods to find an optimal λ, but the most common is with use of the L-curve, [2], [6],[7]. The L-curve plots the solution norm versus the residual norm for valid parameters λ. The name comes from the typical L-shaped form of the curve if plotted in log-log axes, see figure 5.1. The optimal λ is found at the corner of the L-curve. At this corner both the solution norm and the residual norm are smallest, resulting in the best solution of minimization problem.
The problem 6.16 has two important alternative formulations:

$$\min \left\| \begin{pmatrix} A \\ \lambda R \end{pmatrix} \mathbf{x} - \begin{pmatrix} \mathbf{b} \\ 0 \end{pmatrix} \right\|_2 \tag{5.12}$$

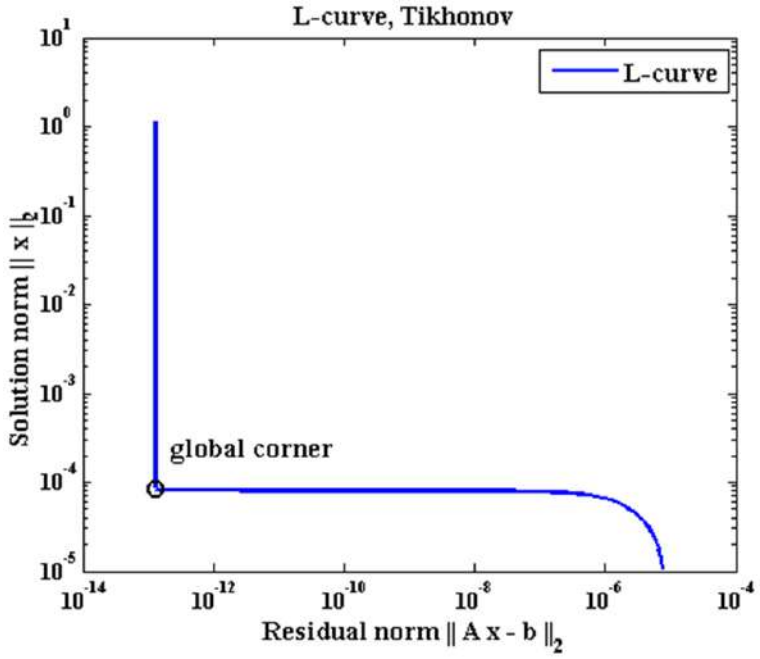

Figure 5.1: Standard L-curve for parameter λ of Tikhonov regularization

and equivalently using the normal equations:

$$(A^T A + \lambda^2 R)\mathbf{x} = A^T \mathbf{b} \tag{5.13}$$

From these formulations it can be observed that the Tikhonov problem can be rewritten to a least-squares problem. Further it can be seen that the solution is unique if the intersection of the null spaces of A and R only contains the zero vector. To construct the regularity condition properties of the problem must be inspected. A basic regularity condition is to add a constraint to the norm of the solution. Then for the regularization operator the identity matrix is used ($R = I$), resulting in the problem:

$$\min_{\mathbf{x}} \{\| A\mathbf{x} - \mathbf{b} \|_2 + \lambda^2 \| I\mathbf{x} \|_2^2\}. \tag{5.14}$$

Now the norm is minimized as well resulting in a more regular solution. Any additional requirements can be added to the problem throughout the regularization operator. With help of finite differences it is possible to add smoothness to the solution. Through the operator R we can force the solution on one element to be close to the solutions on the adjacent elements. The structure of R should be defined for each problem separately.

When the regularized problem is constructed, it naturally must be solved. The Tikhonov criterion can be solved by using the Eldéns bidiagonalization algorithm or by using the singular value decomposition (SVD) or generalized singular value decomposition (GSVD) [5]. Although the bidiagonalization algorithm is the most efficient and numerically stable method to solve the Tikhonov problem, the SVD and GSVD method give more insight into the regularization problem. Note that the SVD is used for problems with $R = I$ and the GSVD is used for problems with $R \neq I$. Since we have $R \neq I$ we need a decomposition for both matrices A and R and therefore the GSVD must be used instead of the SVD. For the implementation of the Tikhonov problem we use methods from the *regtools* package implemented by Hansen [4]. The implemented method for solving the Tikhonov problem makes use of the GSVD.

5.4. Tikhonov error analysis

In coming section we show how Tikhonov regularization influences the error made by the noise components. The right singular vectors provide the basis for the general-form Tikhonov solution $\mathbf{x}_{R,\lambda}$. From the above relations it follows that:

$$p < n: \quad \mathbf{x}_{R,\lambda} = \sum_{i=1}^{p} \gamma_i^{[R,\lambda]} \frac{u_i^T \mathbf{b}}{\sigma_i} q_i + \sum_{i=p+1}^{n} u_i^T \mathbf{b} q_i \tag{5.15}$$

$$p \geq n: \quad \mathbf{x}_{R,\lambda} = \sum_{i=1}^{p} \gamma_i^{[R,\lambda]} \frac{u_i^T \mathbf{b}}{\sigma_i} q_i, \tag{5.16}$$

here filter factors $\gamma_i^{[R,\lambda]}$ have been introduced. The filter factors are defined by:

$$\gamma_i^{[R,\lambda]} = \frac{\sigma_i}{\sigma_i^2 + \lambda^2 \mu_i^2}, \quad i = 1, ..., \min(p, n) \tag{5.17}$$

From the relation $\gamma_i^{[R,\lambda]} = (\sigma_i/\mu_i)^2 / ((\sigma_i/\mu_i)^2 + \lambda^2)$ and $\sigma_i^2 + \mu_i^2 = 1$ the following approximation can be derived:

$$\gamma_i^{[R,\lambda]} \approx \begin{cases} 1, & \sigma_i/\mu_i \gg \lambda, \\ \sigma_i^2/\mu_i^2, & \sigma_i/\mu_i \ll \lambda \end{cases} \tag{5.18}$$

Now remember the measurements of $\mathbf{b}$ are contaminated with noise, see equation 5.3. The naive solution without regularization in terms of the GSVD is as follows:

$$\mathbf{x} = \sum_{i=1}^{n} \frac{u_i^T (\mathbf{b}^{exact} + \mathbf{e})}{\sigma_i} q_i. \tag{5.19}$$

From this equation it is evident that the noise terms are enlarged by small singular values, which is highly unwanted. Now if we look at the solution in equation 5.15, we find that each noise term is also multiplied with the filter factor. Now consider the approximations of the filter factors in equation 5.18. For singular values larger than the parameter λ, the filter factors are close to one and therefore the corresponding GSVD component contribute to the solution with almost full strength. When the solutions are much smaller than the parameter λ, the filter factors are small and these GSVD components are damped. From this it can be concluded that the regularization dampens the contribution from the small singular values and thereby prevents the contribution of increased noise components.

6

Magnetic state model

In the previous chapter we have discussed inverse problems, difficulties related to inverse problems and methods to improve the solutions. Now we turn back to our model and define the models for the computation of the magnetic state and the data-driven updates. For these models the formulation of the inverse problems is defined. In order to find a regularized solution that satisfies our expectations of the solution, a regularization operator is constructed. At the end of this chapter the complete model is summarized in a clear overview and pseudo-algorithms for the model are provided.

6.1. Computation permanent magnetization

6.1.1. Initial State

Before each simulation the initial permanent magnetization and susceptibility must be computed, since these are unknown. The initial permanent magnetization can be computed in multiple ways using the Helmholtz construction and measurements from the onboard sensors as well as the sensors on the array. Using the coils the earth's magnetic field can be disables in a volume around the object. The absence of an applied field results in a zero induced magnetization due to the linear relationship, although there might be a small induced magnetization present due to the permanent magnetization. The measured induced magnetic field measured at the sensors is only caused by the permanent magnetization. The permanent magnetization can then be computed from the inverse problems:

$$\mathbf{B}_m^{arr}(0) = C_1 \mathbf{M}_{per}^1(0)$$

and

$$\mathbf{B}_m^b(0) = C_2 \mathbf{M}_{per}^2(0).$$

To achieve the best from both inversions, the results are averaged:

$$\mathbf{M}_{per}(0) = \frac{1}{2}(\mathbf{M}_{per}^1(0) + \mathbf{M}_{per}^2(0)).$$

If it is not possible to cancel the Earth's magnetic field the permanent magnetization can also be computed in a different way. First apply a field $\mathbf{H}_1 = c$ and then apply a field $\mathbf{H}_2 = -c$. The total measured field is:

$$\mathbf{B}_{red}[\mathbf{M}] = \mathbf{B}_{red}[\mathbf{M}_{ind}] + \mathbf{B}_{red}[\mathbf{M}_{per}]. \tag{6.1}$$

Remember that the induced magnetization is a linear reaction on the applied field and therefore is opposite for $\mathbf{H}_1$ and $\mathbf{H}_2$. Adding equation 6.1 for both applied fields results in:

$$\mathbf{B}_{red}^1 + \mathbf{B}_{red}^2 = 2\mathbf{B}_{red}[\mathbf{M}_{per}].$$

Note that $\mathbf{M}_{per}$ could change slightly due to the first applied field but this is not enough to drastically change the initial condition estimate. Solving this inverse problem results in an initial guess for $\mathbf{M}_{per}$.

The susceptibility distribution of the material can be computed using the Magnetic Susceptibility Estimation Method (MSEM) from [22]. For the computation of the susceptibility the permanent magnetization must be known. Fortunately the inversions for the computation of the permanent magnetization can be done without knowledge of the susceptibility distribution. Therefore in the model first the initial permanent magnetization is estimated after which the susceptibility can be estimated. The complete process can be done offline if there is one set of data available. With offline we mean that this can be done before the actual monitoring system is needed.

6.1.2. Data-driven update

After the initial permanent magnetization has been computed, we want the monitoring system to keep track of changes in the permanent magnetization. These changes should be corrected in the estimation in order to give accurate measurements of the induced magnetic field. For the corrections the system makes use of data collected by the onboard sensors. The onboard sensor group contains in total 24 sensors, which measure the magnetic field inside the object. Care needs to be taken since the sensors are not completely accurate and will give noise in the data. So the true $\mathbf{B}^b$ is equal to the measured $\mathbf{B}^b_m$ minus some noise. Before each iteration the data $\mathbf{B}^b_m(k)$ from the onboard sensors for iteration k is collected. The task is to update the permanent magnetization such that $\mathbf{B}^b_c(k) = C_2\mathbf{M}(k)$ approximates the measured field $\mathbf{B}^b_c(k)$ inside the box the best. Here $\mathbf{M}(k) = \mathbf{M}_{ind}(k) = \mathbf{M}_{per}(k)$. Remember that $\mathbf{B}_0$ has been removed from the measurements $\mathbf{B}^b_m$ and it holds that: $\mathbf{B}^b_m = \mathbf{B}_{res}[\mathbf{M}]$ This results in an minimization problem that needs to be solved. The update step can be written as follows:

$$\mathbf{M}_{per}(k) = \mathbf{M}_{per}(k-1) + \Delta\mathbf{M}_{per}(k) \tag{6.2}$$

The magnetization $\mathbf{M}$ is a sum of the estimated $\hat{\mathbf{M}}(k|k-1)$ and a data based correction of the permanent magnetization $\Delta\mathbf{M}_{per}$. In this prediction model the estimated magnetization is given by:

$$\hat{\mathbf{M}}(k|k-1) = \mathbf{M}_{ind}(k) + \mathbf{M}_{per}(k-1), \tag{6.3}$$

where $\mathbf{M}_{ind}(k)$ is based on the applied field and $\mathbf{M}_{per}(k-1)$ and is computed by solving the inverse problem 4.9:

$$[D + A + B]\mathbf{M}_{ind}(k) = \mathbf{H}_a(k) - [A + B]\mathbf{M}_{per}(k-1) \tag{6.4}$$

From the estimated magnetization the magnetic field $\mathbf{B}^b_c[\hat{\mathbf{M}}](k)$ inside the box can be computed using the forward system $\mathbf{B}^b_m(k) = C_2\mathbf{M}(k)$. Comparison of the measured field and the estimated field results in a residual field from which the data based correction of $\mathbf{M}_{per}(k)$ can be found.

$$\mathbf{B}_{res}(k) = \mathbf{B}^b_m(k) - \mathbf{B}_c(\hat{\mathbf{M}}(k)). \tag{6.5}$$

$$\mathbf{B}_{res}(k) = C_2\Delta\mathbf{M}_{per}(k) \tag{6.6}$$

The computation of $\Delta\mathbf{M}_{per}$ again results in solving an inverse problem. These inverse problems are studied in more detail in the next sections. After the correction has been computed both $\mathbf{M}_{per}(k)$ and $\mathbf{M}(k)$ are updated:

$$\mathbf{M}_{per}(k) = \mathbf{M}_{per}(k-1) + \Delta\mathbf{M}_{per}(k) \tag{6.7}$$

$$\mathbf{M}(k) = \mathbf{M}_{ind}(k) + \mathbf{M}_{per}(k) \tag{6.8}$$

Remember from equation 3.19 that the induced magnetization is dependent on the applied field as well as on the permanent magnetization. At this moment the induced magnetization at time step k is dependent on the permanent magnetization from the previous time step $k-1$. It might be more realistic for the induced magnetization at time step k to be dependent on the permanent magnetization of time step k. Since it is not yet clear which resembles the induced magnetization the best we consider two models, one where the induced magnetization is only based on the permanent magnetization of the previous time step and one where an extra update on the induced magnetization is done. The additional update is done by solving:

$$[D + A + B]\mathbf{M}_{ind}(k) = \mathbf{H}_a - [A + B]\mathbf{M}_{per}(k) \tag{6.9}$$

6.2. The inverse problem

In the construction of the model multiple inverse problems were encountered. In the current section the inverse problems are examined to find if they are well-posed. The first inverse problem encountered is the computation of the induced magnetization from the permanent magnetization and the applied field:

$$[D+A+B]\mathbf{M}_{ind}(k) = \mathbf{H}_a - [A+B]\mathbf{M}_{per}(k) \tag{6.10}$$

$$K_1\mathbf{M}_{ind}(k) = h0 - K_2\mathbf{M}_{per}(k) \tag{6.11}$$

For simplicity matrix [D+A+B] are named matrix K_1 and matrix [A+B] is denoted by K_2. Note that the computation of $\mathbf{M}_ind$ is an inversion, based on matrix K_1. The condition number of this matrix is approximately 71, from which it can be concluded that this inversion is well-posed and therefore can be solved without the need for regularization. The other inverse problems occur when the magnetization has to be computed from the induced magnetic field values at the sensor positions. These inverse problems are used for the computation of the initial permanent magnetization and the corrections. Remember from chapter 4 that the forward problems are given by

$$\mathbf{B}_m^{arr} = C_1\mathbf{M}, \tag{6.12}$$

for the sensors on the array and by

$$\mathbf{B}_m^{b} = C_2\mathbf{M}, \tag{6.13}$$

$$\mathbf{B}_{res}(k) = C_2\Delta\mathbf{M}_{per}(k) \tag{6.14}$$

for the onboard sensors. Unfortunately these problems can not be solved directly for $\mathbf{M}$, since we are working with large discrete systems with ill-posed, ill-ranked matrices C_1 and C_2. Especially matrix C_1 is ill-posed, since it has a condition number of $1.446 \cdot 10^6$[6]. The matrix C_2 is better posed than C_1 but still not good with a condition number of 3524. The high condition number of the matrices mean that small perturbations of the right-hand side result in large errors in the naive solution $\mathbf{M}_{per}^{exact}$, as explained in the previous chapter. In order to improve the solutions from the ill-posed inverse problems we use the Tikhonov regularization method. Further it also has to be taken into account that the measurements B_m contain measurement noise and we do not want to fit the noise in the model.

6.2.1. Regularization for $\mathbf{M}_{per}$

As noted in the previous part it is essential to improve the inversion in order to reduce inaccuracies in the solutions. A common way for this is to use regularization [6], as discussed in the previous chapter. We only consider the Tikhonov regularization for the ill-posed problem of the correction step. The redefinition of the inverse problems for the initial permanent magnetization can be done likewise. Tikhonov regularization replaces the ill-conditioned problem

$$\min_{\mathbf{x}} \parallel C_2\Delta\mathbf{M}_{per} - \mathbf{B}_{res} \parallel_2 \tag{6.15}$$

with the nearby problem

$$\min_{\mathbf{x}}\{\parallel C_2\Delta\mathbf{M}_{per} - \mathbf{B}_{res} \parallel_2^2 + \lambda^2 \parallel R\mathbf{M}_{per} \parallel_2^2\}. \tag{6.16}$$

Here λ is a regularization parameter which weights both parts of the criterion function and R is the regularization operator which adds a certain requirement to the solution. In order to add a correct and useful requirement, the expected properties of the permanent magnetization need to be inspected. We expect the permanent magnetization to be more or less equal throughout the material, since most of the material experienced the same magnetic history. Naturally differences may exist due to earlier stress or other deformations of the material. However we assume there are no extremes in a short time span. Further we also assume that the permanent magnetization changes gradually due to the magnetic field and does not make large increases/decreases within one time step.

Therefore we can choose to pose a smoothness requirement on the permanent magnetization in each direction separately. This smoothness conditions ensures that the permanent magnetization in each direction at a grid point does not differ much from the adjacent grid points. The separation of the directions is important, since large differences can occur between directions of the permanent magnetization depending on the directions of the applied fields in the history. Such as smoothing condition can be applied to the system in the form of a smoothing operator R.

6.2.2. Smoothing operator for $\mathbf{M}_{per}$

The smoothing operator is designed in such a way that in the solution the value at one grid point does not differ much from the adjacent grid points. We call two grid points adjacent when they share an element. To find the adjacent grid points of point p_k we need to add all grid points from the elements in which p_k is contained and then filter all double points and the point i. In figure 6.1 part of a triangulation is shown. We consider point 5 colored in green, its adjacent grid points are colored in yellow. From the figure it can be seen that each adjacent grid point is part of an element in which 5 is contained. Note also that for example grid point 6 is contained in two of these elements and therefore doubles should be filtered.

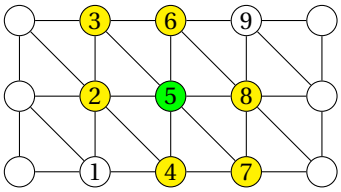

Figure 6.1: Example of a triangulation

In the mesh of the SVP01, each grid point p_k has at least 3 and at most 8 adjacent grid points. Define the function

$$\psi : \bigcup_{k=1}^{N_p} p_k \to \{3,4,5,6,7,8\}, p_k \mapsto \psi(p_k) \tag{6.17}$$

as the number of adjacent grid points. The smoothing operator originates from finite differences, which says that the value at point i should be 'close' to the average of the adjacent grid points. We quantify 'close' by adding an innovation term $I_k \sim \mathcal{N}(0,\sigma_k^2)$ to the equation. The innovations term shows in what extend the value of $\mathbf{M}_{per}^{p_k}$ can differ from its neighbours. The smoothness condition can be formalized by the following equation:

$$\mathbf{M}_{per}^{p_k} = \frac{1}{\psi(p_k)} \sum_{i=1}^{\psi(p_k)} \mathbf{M}_{per}^{p_{ki}} + I_k \tag{6.18}$$

To illustrate this idea, apply 6.18 to the grid points in fig 6.1 to obtain e.g.

$$\mathbf{M}_{per}^{p_5} = \frac{1}{6}(\mathbf{M}_{per}^{p_2} + \mathbf{M}_{per}^{p_3} + \mathbf{M}_{per}^{p_4} + \mathbf{M}_{per}^{p_6} + \mathbf{M}_{per}^{p_7} + \mathbf{M}_{per}^{p_8}) + I_5, \tag{6.19}$$

$$\mathbf{M}_{per}^{p_4} = \frac{1}{5}(\mathbf{M}_{per}^{p_1} + \mathbf{M}_{per}^{p_2} + \mathbf{M}_{per}^{p_5} + \mathbf{M}_{per}^{p_7} + \mathbf{M}_{per}^{p_8}) + I_4. \tag{6.20}$$

The set of equations from 6.18 can be written as: $R\mathbf{M}_{per} = E$, where $R = (I_{NpxNp} - S)$, $E \sim \mathbf{N}(0, \Sigma_{NpxNp})$ and S is originates from the right hand side in 6.20. Here the standard average is considered, since all triangles are the same size and the distance between the grid points is approximately the same. In the general case where the mesh is not uniform, the generalized form can be used, which gives more weight to grid points close by:

$$\mathbf{M}_{per}^{p_k} = \sum_{i=1}^{\psi(p_k)} \left(\frac{1 - \delta(p_k, p_i)}{\sum_{j=1}^{\psi(p_k)} 1 - \delta(p_k, p_j)} \right) \mathbf{M}_{per}^{p_{ki}} + I_k, \tag{6.21}$$

here $\delta(p_k, p_j)$ measures the distance between grid point p_k and p_j.

If this operator is used in the regularization the solution shows more uniformity dependent on the value of λ. For small λ there is less weight on the term with R and therefore the solution will be less regular. If there is a higher λ the operator term becomes more important and the solution will show more regularity. In the experiments we use the λ found by the L-curve.

6.3. Signature Monitoring Model

In the previous chapters the model has been build and all mathematical theory has been discussed. The basic structure of the signature monitoring model is given in figure 6.2. In the blue rectangles the monitoring model can be found, in the grey rectangle the method of validation can be seen. Naturally first the initial values for the permanent magnetization and susceptibility need to be computed (not shown in the structure). After the initial condition it follows the structure for each time step. In each iteration the magnetic state of the object is computed. First the induced magnetization is found from the previous permanent magnetization and the applied field. Then comparison with the onboard sensor data results in an update for the permanent magnetization after which the total magnetization can be computed. From the total magnetization we move towards the forward problem, where the magnetic signature at the array below the vessel is computed from the magnetization. According to this structure and with use of all theory discussed in the previous chapters,

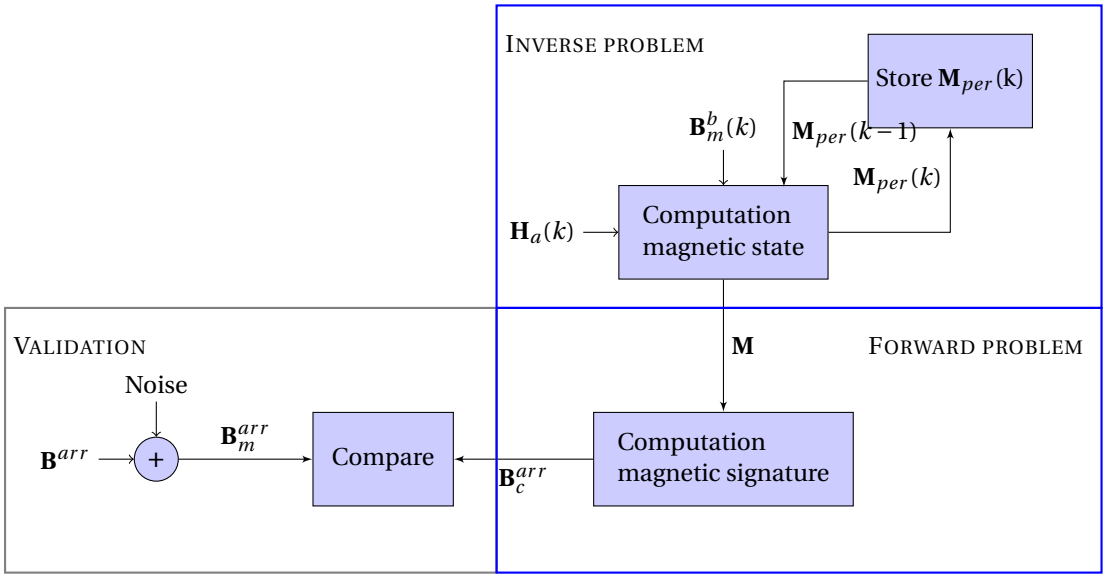

Figure 6.2: Structure magnetic signature monitoring system

we give two pseudo-codes for the prediction algorithms. First for the model without regularization on the inversion and secondly with regularization on the inversions. For the model with regularization we can either provide a fixed regularization parameter λ which is used in all inversions or we can provide λ = 'free' and let the L-curve determine an optimal parameter. In the pseudo-codes the computation of the necessary matrices A, B, D, C_1, C_2 are not shown for clarity, since these can be computed and saved in advance.

Prediction model without regularization
Input: $\mathbf{H}_a, \mathbf{B}_m^b$
Output: $\mathbf{B}_c^{arr}, \mathbf{M}$

- Compute initial permanent magnetization from onboard and array sensors (inversions):
  - $\mathbf{B}_m^b(0) = C_2\mathbf{M}_{per}^1$
  - $\mathbf{B}_m^{arr}(0) = C_1\mathbf{M}_{per}^2$
  - $\mathbf{M}_{per}(0) = \frac{1}{2}(\mathbf{M}_{per}^1 + \mathbf{M}_{per}^2)$
- Compute estimated susceptibility pattern $\hat{\chi}$ with Magnetic Susceptibility Estimation Method.
- **for** each $\mathbf{H}_a(k)$:
  - Compute induced magnetization (inversion): $[A+B+D]\mathbf{M}_{ind}(k) = \mathbf{H}_a(k) - [A+B]\mathbf{M}_{per}(k-1)$.
  - Set $\mathbf{M}_{temp}(k) = \mathbf{M}_{ind}(k) + \mathbf{M}_{per}(k-1)$.
  - Compute field onboard sensors: $\mathbf{B}_c^b(k) = C_2\mathbf{M}_{temp}(k)$.
  - Compute residual field: $\mathbf{B}_{res}(k) = \mathbf{B}_m^b(k) - \mathbf{B}_c^b(k)$.
  - Compute correction (inversion): $\mathbf{B}_{res}(k) = C_2\Delta\mathbf{M}_{per}(k)$
  - Update $\mathbf{M}_{per}$ and $\mathbf{M}$: $\mathbf{M}_{per}(k) = \mathbf{M}_{per}(k-1) + \Delta\mathbf{M}_{per}$ and $\mathbf{M}(k) = \mathbf{M}_{ind}(k) + \mathbf{M}_{per}(k)$.
- Compute magnetic field at array: $\mathbf{B}_c^{arr} = C_1\mathbf{M}$.

In the above model all inversions are done without use of regularization, meaning that each solution of an inverse problem is found by solving the least squares problem. Since we expect the solutions from the regular inversion to be inaccurate due the high condition number of matrices C_1 and C_2, in the next overview the model with regularization is shown. Both models are compared in the next chapter to find the influence of regularization.

The prediction models are implemented in the Matlab. For the regularization we made use of the functions *cgsvd,tikhonov* and *lcurve* from the *regtools* toolbox. The functions in this toolbox are designed and implemented by P.C. Hansen [4]. The well-posed inversion for $\mathbf{M}_{ind}$ is done using the backslash operator from Matlab. For the remaining implementation only standard Matlab functions and own implementations have been used. For computational convenience variables and matrices are computed and saved in advance.

Prediction model with regularization
Input: $\mathbf{H}_a$, $\mathbf{B}_m^b$, λ
Output: $\mathbf{B}_c^{arr}$,$\mathbf{M}$

- Compute regularization operator: R = RegularizationOperator(P,E)
- Compute Compact Singular Value Decomposition of C_1 and C_2:
  - $[U, sm, X, V]$ = cgsvd(C_2,R)
  - $[U1, sm1, X1, V1]$ = cgsvd(C_1,R)
- Compute initial state from onboard and array sensors (inversions):
  - If λ = 'free': λ_1 = lcurve($U, sm, B_m^b, tikh$), λ_2 = lcurve($U1, sm1, B_m^{arr}, tikh$)
  - $\mathbf{M}_{per}^1$ = tikhonov($U, sm, X, B_m^b(0)', \lambda_1$)
  - $\mathbf{M}_{per}^2$ = tikhonov($U1, sm1, X1, B_m^{arr}(0)', \lambda_2$)
  - $\mathbf{M}_{per}(0) = \frac{1}{2}(\mathbf{M}_{per}^1 + \mathbf{M}_{per}^2)$
- Compute estimated susceptibility pattern $\hat{\chi}$ with Magnetic Susceptibility Estimation Method.
- **for** each $\mathbf{H}_a(k)$:
  - Compute induced magnetization (inversion): $[A+B+D]\mathbf{M}_{ind}(k) = \mathbf{H}_a(k) - [A+B]\mathbf{M}_{per}(k-1)$.
  - Set $\mathbf{M}_{temp}(k) = \mathbf{M}_{ind}(k) + \mathbf{M}_{per}(k-1)$.
  - Compute field onboard sensors: $\mathbf{B}_c^b(k) = C_2\mathbf{M}_{temp}(k)$.
  - Compute residual field: $\mathbf{B}_{res}(k) = \mathbf{B}_m^b(k) - \mathbf{B}_c^b(k)$.
  - If λ = 'free': λ_3 = lcurve($U, sm, \mathbf{B}_{res}(k), tikh$)
  - Compute correction (inversion): $\Delta\mathbf{M}_{per}(k)$ = tikhonov($U1, sm1, X1, B_{res}(k), \lambda_3$)
  - Update $\mathbf{M}_{per}$ and $\mathbf{M}$: $\mathbf{M}_{per}(k) = \mathbf{M}_{per}(k-1) + \Delta\mathbf{M}_{per}$ and $\mathbf{M}(k) = \mathbf{M}_{ind}(k) + \mathbf{M}_{per}(k)$.
- Compute magnetic field at array: $\mathbf{B}_c^{arr} = C_1\mathbf{M}$.

7

Steel Vessel Prototype 01 and setup

In this chapter we explain the object of concern, the SVP01, and the Helmholtz structure used to compute the necessary data. This object is used in the twin experiments to validate the model. The SVP01 and Helmholtz structure are designed by and located at TNO[1].

The Steel Vessel Prototype 01 is a rectangular box, consisting of four attached open cubes of 12x12x12 cm, without a top plate, see figure 7.1a. This results in a total length of 48 cm, a width of 12 cm and a height of 12 cm. The thickness of the used steel plates is 0.5 mm. In each of the cubes there are five sensors, placed in the middle of the faces, which can measure the magnetic field in all three directions. Note these are not visible in the figure, later we look more closely at the sensors. Each of the cubes contains coils in all directions, such that it is possible to construct a desired magnetic field inside the box. For this research only the sensors inside the box are used, since these are important for the monitoring system. In the software program Blender a 3D model of the box has been build, in this model all squares of 12x12 cm are divided into two triangles to create a simple triangular mesh of 34 elements. The choice and method of meshing are discussed further on in this chapter. The Blender models can be found in figure 7.1. In the solid frame figure it is clear that the 3D model is a good visualization of the SVP01, from the wireframe model the basic mesh of 34 elements can be observed.The SVP01 is placed inside 'Clavis', a square Helmholtz coil structure, see figure

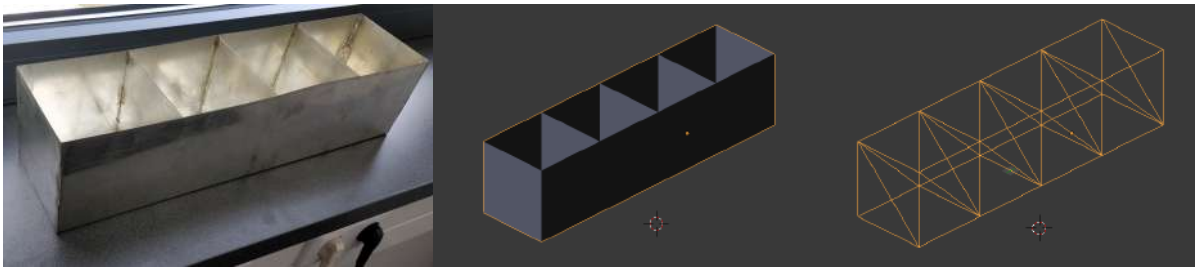

(a) Real SVP01 (b) Blender solid frame (c) Blender wireframe

Figure 7.1: SVP01 and 3D models in Blender

7.2b. The structure consists of a cage surrounded with multiple coils in each direction. This combination of coils makes it possible to construct a locally uniform magnetic field in all three directions in a volume within the cage. The magnitude of the field can be chosen between ± 100 microtesla, which is about two times the Earths magnetic field. Note that with these numbers it is also possible to cancel the Earths magnetic field. In the implementation we follow the local axes from Clavis. The vessel is placed with its middle point of the bottom located at the origin of the local axes. The long side of the vessel is placed in the x-direction and the short side in the y-direction. The z-field is defined positive in the downward direction, such that the z-axis is positive below the origin. In figure 7.2a the positive direction of the x-,y- and z-direction are indicated by the arrows. These orientations hold if one is looking from above into Clavis (Birds view). The vessel is placed on a

[1]The Netherlands Organization for Applied Scientific Research.

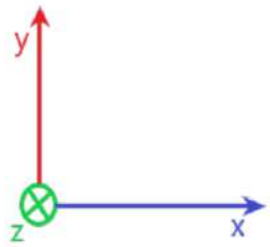

(a)
Orientation of axis in Clavis (Birds view)

(b) Helmholtz structure

Figure 7.2: Helmholtz structure 'Clavis' and axis orientation

plastic template with markers to ensure that it is in the same place with all experiments. Below the Helmholtz structure is a sensor array of 75x30 cm located, which contains 112 sensors. These sensors are the same as the onboard sensors and they can measure the magnetic induction field below the vessel in three directions.

The sensors used are Honeywell HMC883L sensors with a noise level of approximately 1 μT. The sensors are divided into two groups, the onboard sensors and the array sensors. Inside the box there are 20 sensors located, five inside each 12x12x12 cube, all close to the middle of one of the faces. The sensors are connected to a flexible plastic model, which can be fitted inside the box. In figure 7.3a one sensor, connected to the flexible model can be seen. One can also see a few of the onboard coils of the vessel. In this way the sensors can be calibrated without the steel cover of the vessel and are always at approximately the same positions inside the vessel. At the front and back there are two more sensors located outside the vessel. These 24 sensors are all part of the onboard sensor group. The implemented onboard sensors can be found in black in figure 7.4a. The magnetic field measured by the onboard sensors is denoted by $\mathbf{B}_m^b$, where the m stands for measured and the b for onboard. Beneath the box, at a height of 56 mm, there is a sensor array located with in total 112 sensors, these sensors are all part of the array sensor group. Both the real sensor array and the Matlab figure of the array sensors can be found in figure 7.4. The magnetic field measured by the array sensors is denoted by $\mathbf{B}_m^{arr}$, where the m is for measured and the arr is for array. The onboard sensors are used as input to the prediction model, while the measurements from the sensor array are used for the validation. Note that the measurements from the sensors, contain the true magnetic field as well as measurement noise. The order of the noise of these Honeywell sensors is approximately 1 μT.

Further it has to be kept in mind that the measured magnetic field is a combination of the applied field and the reduced magnetic field. The reduced magnetic field is of interest to us, since it is caused by the magnetization of the object. Obviously the values of the applied fields are known and therefore the data from the sensors can be corrected, such that the data only contains the reduced magnetic field. In the rest of this research the measurement data from the sensors only includes the reduced field and not the applied field: $\mathbf{B}_{res} = \mathbf{B}_m - \mathbf{B}_a$. When speaking of $\mathbf{B}_m^b$ or $\mathbf{B}_m^a$ we always refer to the corrected values.

The earlier described CAD model is loaded into Matlab, where the mesh can be refined. In the mesh refinement each triangle is divided into four equal triangles, resulting quickly in large numbers of elements. In each step the mesh becomes four times as large. The loaded CAD model consists of a mesh with 34 elements, after one division this has already increased to 136 elements and after two divisions the mesh consists of 544 elements. In general, the methods results in a mesh of the SVP01 with $34 \cdot 4^{div}$ elements for number of divisions $div = 1,2,3...$ [2]. In this research we work with a mesh of $34 \cdot 4^2 = 544$ elements, see figure 7.5a. For more accurate measurement a smaller mesh can be taken, however this also significantly increases the computational time.

[2] The mesh refinement is done with code written by Bart-Jan Peet, employee of TNO

(a) Board sensor

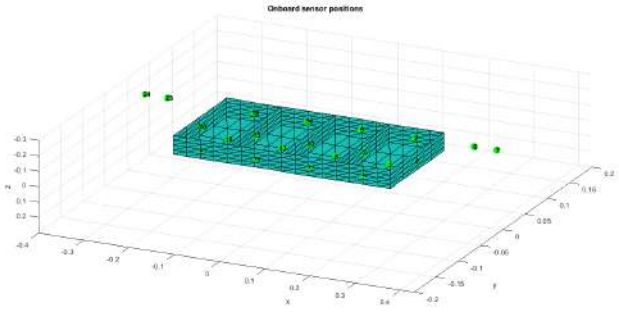

(b) Board sensors Matlab

Figure 7.3: Board Sensors

(a) Sensor array

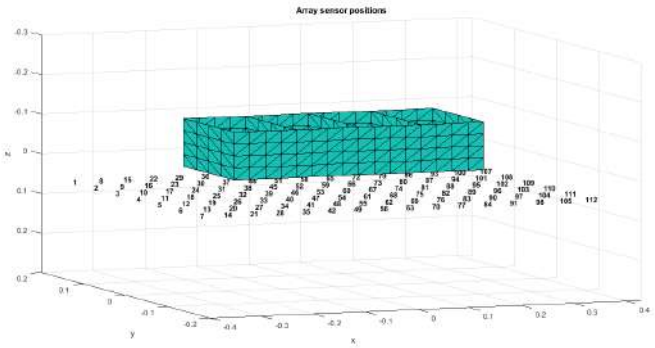

(b) Array sensors Matlab

Figure 7.4: Array Sensors

In subsection 4.1.4 a remark was made on the computation of the outward normal vectors in 3-dimensions. From the discretization of the box it can be observed that there are boundary elements present which have two different orientations for their outward normals, since they are connected to two elements. In order to check the method and its implementation, the normal vectors are plotted together with the box in figure 7.5b. All the normal vectors are pointing outward and boundary elements at corners have two normal vectors as expected.

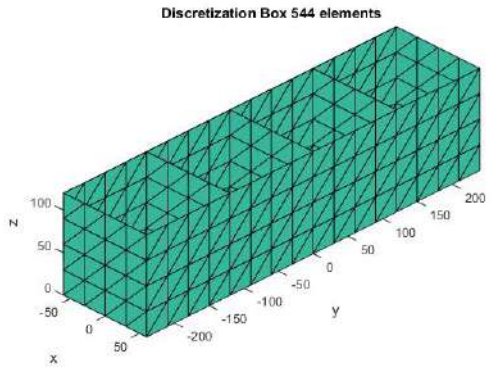

(a) Discretization steel box

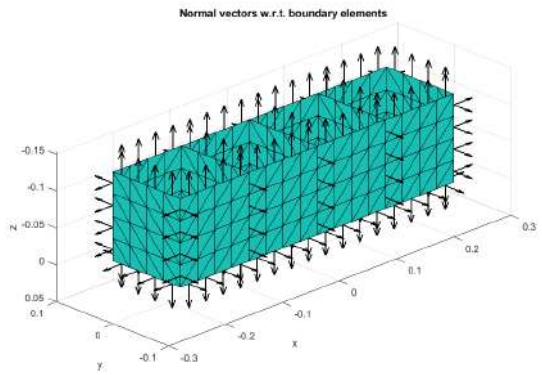

(b) Normal vectors boundary elements

Figure 7.5: Mesh SVP01 and outward normals

8

Twin Experiments

To test the performance of the designed model, multiple twin experiment are conducted. In twin experiments the designed model is used to create a set of observations, noise is added to this set of observations to create a simulation data set. Then with help of the same model it is tried to estimate the true model parameters from the noisy data. From twin experiments it can be concluded if the model is correctly implemented and it can be observed how well the model is able to handle noise components. In the twin experiments the computed observations consist of a varying applied field $\mathbf{H}_a$ and the magnetic induction field onboard as well as on the array. The onboard data and the applied field are used as input for the model and the array data is used as the validation data. No noise is added to the applied field, since we assume that the applied field is a known input. For the first experiments we assume that the susceptibility is known in order to prevent inaccuracies from the susceptibility estimation contaminating the performance of the model. In the next section we elaborate on the used parameters and the simulation data. The monitoring model is used to predict the magnetization in the box and the induced field on the sensor array on basis of the applied field and the data from the onboard sensors. To test the performance of the prediction model, we run a number of twin experiments. The twin experiments are divided into three phases.

In phase I the twin experiments are based on data generated with constant permanent magnetization $\mathbf{M}_{per}$ in time and without noise. In this data set the permanent magnetization and the applied field are both defined in the $x-$direction. The monitoring model is first tested on data without noise, such that we can observe whether the model is correctly implemented and we can observe the behaviour of the inversions. In phase I the influence of regularization is tested as well as the influence of the data-assimilation. In the last part of phase I twin experiments are conducted to test the performance of the model in the $y-$ and $z-$ direction. From phase I we hope to conclude that the model and the inversions work properly and that there are no implementation mistakes.

In phase II we continue with data sets contaminated with noise, in order to test the behaviour of the inversions on the noise components. In this phase we also propose and test two improvements of the models: one improvement for the computation of $\mathbf{M}_{ind}$ and one for the computation of the initial estimate of $\mathbf{M}_{per}$.

In phase III more complex types of permanent magnetizations are used for the generation of the data to gain more insight into the performance of the model in real-life situations. First a twin experiments with a linearly varying permanent magnetization is conducted, since we expect the permanent magnetization to change approximately linear in practice. Moreover an experiment is conducted using a non-uniform permanent magnetization, to find the ability of the model to approximate non-uniform distributions. In the last experiment that is conducted, we no longer assume that the susceptibility distribution is known. Noisy estimates of the susceptibility distribution are used instead of the true values. Here we hope to draw some conclusions on the influence of inaccuracies in the susceptibility estimation in the magnetic field predictions.

8.1. General notions

The twin experiments are based on a few general assumptions. In most experiments we assume that the susceptibility distribution is known and uniform: $\chi \equiv \chi_{true}$. Only in the last experiment the susceptibility distribution is estimated. For each separate experiment we look at two different type of figures, the first figure shows contour plots of the measured and computed induced magnetic field at all sensors locations at time step 48 ($\mathbf{H}_a \approx 18.7 A/m$). In grey the projection of the SVP01 on the sensor array is drawn in the contour plots. In these figures also the contour plots of the absolute and relative error are shown, we refer to these two errors as the absolute/relative field errors. These errors are the vector norms of all three directions in one sensor location for time step 48 and thereby show the error per sensor:

$$\epsilon^s_{abs} = \| \mathbf{B}^{arr}_m - \mathbf{B}^{arr}_c \|_2, \quad \epsilon^s_{rel} = \frac{\| \mathbf{B}^{arr}_m - \mathbf{B}^{arr}_c \|_2}{\| \mathbf{B}^{arr}_m \|_2} \tag{8.1}$$

The absolute error ϵ^s_{abs} is measured in Tesla's [T] and the relative error ϵ^s_{rel} is logically dimensionless. The second figures shows the evolution of the (permanent) magnetization and the correction over time for grid point 25. This figure also shows the evolution of the absolute and relative errors over time for array sensor 25. In these figures the absolute and relative errors are defined pointwise per sensor and per direction separately. We refer to these errors as the absolute/relative point errors:

$$\varepsilon^p_{abs} = |\mathbf{B}^{arr}_m - \mathbf{B}^{arr}_c|, \quad \varepsilon^p_{rel} = \frac{|\mathbf{B}^{arr}_m - \mathbf{B}^{arr}_c|}{|\mathbf{B}^{arr}_m|}. \tag{8.2}$$

Again the unit of ε^p_{abs} is T and ε^p_{rel} is dimensionless. From animations and data analysis it is clear that the other grid points and sensor locations show the same behaviour. Therefore it suffices to consider only these two figures. Next to each case one can also find a QR code, which can be scanned with a smartphone application. The QR codes are connected to the animation of the model. These animations show the measured field and the computed prediction changing over time. The animations are added as an extra feature and in general the analysis of the twin experiments will be based on the figures in this report. In the models with regularization we use the notation 'free' for λ to denote that this parameter is optimized by the L-curve in each iteration and is variable. In some cases the λ is assigned a specific value, which is used in all inversions. As a last general note, remember that the purpose of the model is to predict the reduced magnetic field at the sensor array. In the results we also discuss how well the model is able to reconstruct the permanent magnetization, since we assume a better reconstruction of the permanent magnetization results in a better prediction. Further the accuracy of this reconstruction also gives information on the accuracy of the inversions. However the correct reconstruction of the magnetization is the second measure for the performance of the model.

8.2. Data generation

We start by computing the set of data using a constant permanent magnetization of 500 Am^{-1} in the $x-$direction and zero in both $y-$ and $z-$direction and an uniform susceptibility distribution of 100. For the applied field H_a a sinusoidal field with an amplitude of 100 A/m is taken. The applied field can be seen in figure 8.1. We discretized the field in 101 steps to be able to compute the prediction at each field strength. The induced magnetization is computed according to the computed model, based on the applied field and the permanent magnetization:

$$\left[\sum_{i=1}^{N_e} \frac{1}{\chi} D_i + A + B \right] \mathbf{M}_{ind} = \mathbf{H}_a - [A+B]\,\mathbf{M}_{per}$$

The total magnetization is given by $\mathbf{M} = \mathbf{M}_{ind} + \mathbf{M}_{per}$. Now matrices C_1 and C_2 from 4.2 can be used to compute the induced magnetic fields at all the sensor locations:

$$\mathbf{B}^{arr} = C_1 \mathbf{M}$$
$$\mathbf{B}^{b} = C_2 \mathbf{M}$$

The values of the induced magnetic fields $\mathbf{B}^b_m$ and $\mathbf{B}^{arr}_m$ are saved together with the applied field. $\mathbf{B}^b$ has 3 times $N = 24$ measurements per time step and 101×72 measurements in total. $\mathbf{B}^{arr}$ has 3 times $N = 112$ measurements per time step and 101×336 measurements in total.

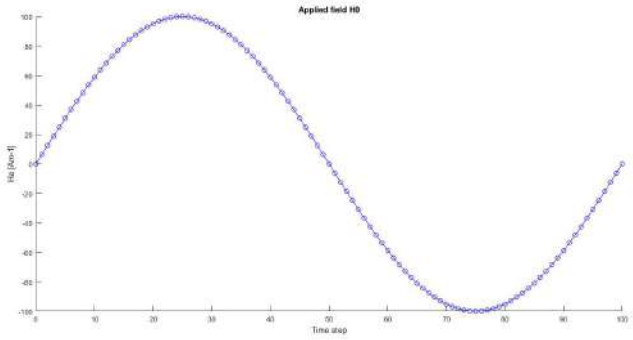

Figure 8.1: Applied field $\mathbf{H}_a$ for one direction, other directions zero.

To be able to test how well the model performs with noisy data, we also create data sets contaminated with Gaussian white noise:

$$\mathbf{B}_m^b = \mathbf{B}_c^b + \mathbf{e}, \mathbf{e} \sim \mathcal{N}(0, \sigma^2 I_{3Nx3N}). \tag{8.3}$$

We choose $\sigma = 2 \cdot 10^{-7}$ as the standard deviation of the noise, which results approximately in an variation of 1 μT in each sensor. As mentioned in chapter 7 the noise level in the sensors is approximately 1 μT. In each individual direction the noise is contained within $3\sigma = 6 \cdot 10^{-7}$. The other data sets are generated likewise but with a different predefined permanent magnetization. The following data sets are constructed:

- Data set 1: Constant $\mathbf{M}_{per}$ 500 A/m in x-direction without noise, $\mathbf{H}_a$ in x-direction.
- Data set 2: Constant $\mathbf{M}_{per}$ 500 A/m in y-direction without noise, $\mathbf{H}_a$ in y-direction.
- Data set 3: Constant $\mathbf{M}_{per}$ 500 A/m in z-direction without noise, $\mathbf{H}_a$ in z-direction.
- Data set 4: Constant $\mathbf{M}_{per}$ 500 A/m in x-direction with noise $\sigma = 2 \cdot 10^{-7}$, $\mathbf{H}_a$ in x-direction.
- Data set 5: Linear varying $\mathbf{M}_{per}$ in x-direction with noise $\sigma = 2 \cdot 10^{-7}$, $\mathbf{H}_a$ in x-direction.
- Data set 6: Non-uniform $\mathbf{M}_{per}$ in x-direction with noise $\sigma = 2 \cdot 10^{-7}$, $\mathbf{H}_a$ in x-direction.

8.3. Phase I: Fixed permanent magnetization with noiseless data

The first experiments are conducted with data set 1: a constant permanent magnetization without noise. We test the monitoring model without regularization on the model, after which the model with regularization is used to find the influence of regularization. From these experiments it is concluded whether the regularization is necessary. After the experiments on regularization we turn to the validation of the usage of data-assimilation. In order to ensure that the data-assimilation is an useful and important part of the model, a twin experiment using the model without data-assimilation is conducted. These results are compared to the result of the model with data-assimilation. At last it is validated that the models work in both $y-$ and $z-$direction with the same accuracy. We expect the model to be able to correct the computed initial condition of $\mathbf{M}_{per}$ to the true value of $\mathbf{M}_{per}$, since there are no noise components in the data.

8.3.1. Regularization

First lets consider the results from the model without regularization on data set 1. The results can found in figures 8.2 and 8.3.

From figure 8.2 it can be observed that the prediction of the field strength is not very accurate with a maximum absolute error of 4.3142 μT. It is also visible that the form of the computed field does not resemble the measured field very well. From figure 8.3 we find that the model corrects the permanent magnetization in both $x-$ and $z-$direction, even though the true $\mathbf{M}_{per}$ is only present in the $x-$direction. The corrections do not converge to zero which we would expect if the estimated permanent magnetization converges to the constant permanent magnetization. Note that the absolute error in the $x-$direction at sensor 25 is increasing linearly over time. From the data we find that the estimated $\mathbf{M}_{per}$ has large variations between grid points and between directions, these large variations can be seen in figure 8.5.

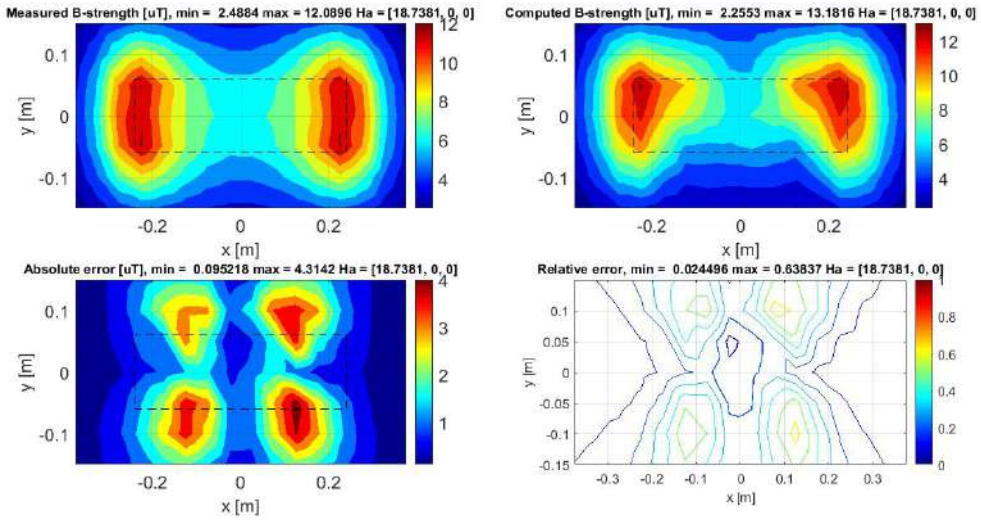

Figure 8.2: Measurements, predictions and errors of the induced field strength without regularization and noise, $\mathbf{H}_a$ in x-direction, $\mathbf{M}_{per}^{true}$ 500 A/m in x-direction

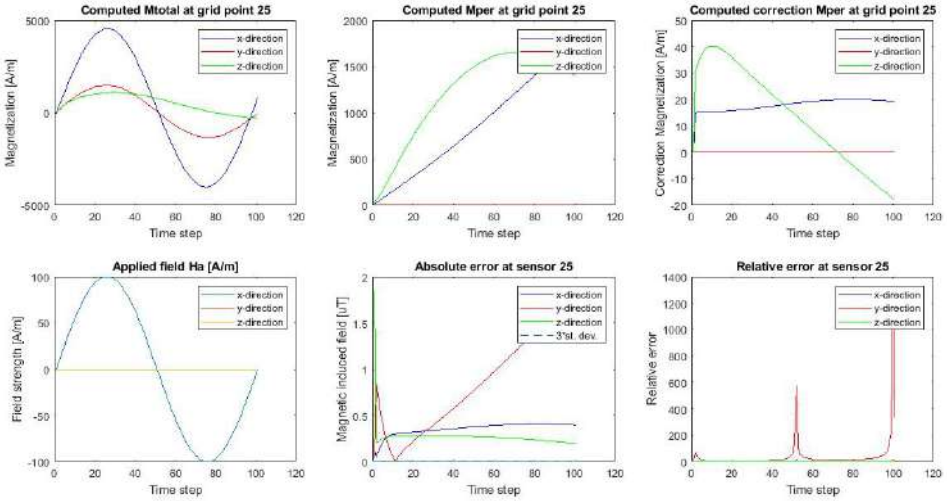

Figure 8.3: Evolution of magnetization and prediction errors over time without regularization and noise, $\mathbf{H}_a$ in x-direction, $\mathbf{M}_{per}^{true}$ 500 A/m in x-direction

Figure 8.4: Animation, without regularization, without noise

Here the initial estimated permanent magnetization is shown for each direction at each grid point. It is evident that the initial estimate of the permanent magnetization in no way resembles the true permanent magnetization. Inspection of the data shows that the model only corrects the permanent magnetization at certain grid points close to the sensor positions. We expect the estimated permanent magnetization to be smooth in each direction, such that the permanent magnetization in one grid point does not differ too much from its neighbours. To force the model to find this type of solution we use the Tikhonov regularization with the smoothing operator, introduced in section 6.2.1. To give an impression of the influence of this parameter, the initial permanent magnetization is estimated with different parameters: $\lambda = 10^{-9}, 10^{-7}, 10^{-5}$. Remember that for smaller λ the regularization term is less important than for higher λ. The estimations are shown in figure 8.6, it is evident from the figures that a higher λ results in a smoother solution. Note however that the initial estimate in the x-direction is far from the true value 500 A/m.

Now the question is, which λ will give the best prediction? In order to find the optimal λ the L-curve is

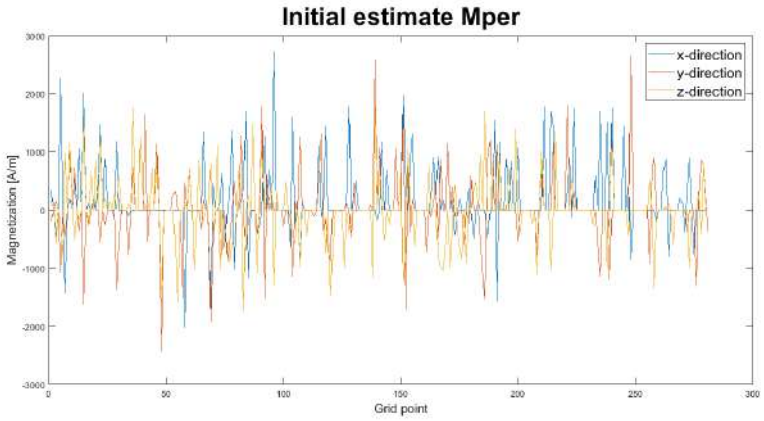

Figure 8.5: Initial estimate permanent magnetization without regularization for data set 1.

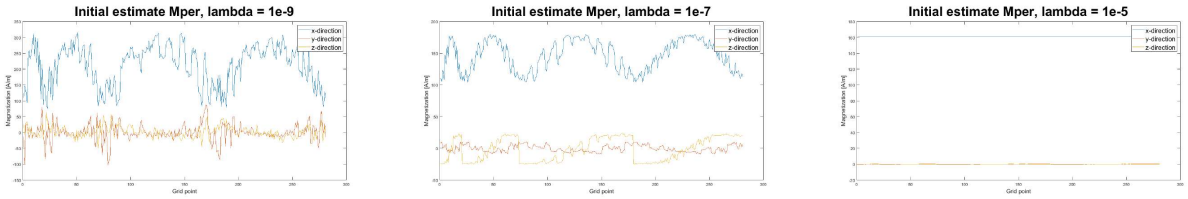

(a) $\lambda = 10^{-9}$ (b) $\lambda = 10^{-7}$ (c) $\lambda = 10^{-5}$

Figure 8.6: Initial estimates permanent magnetization with different regularization parameters λ[1]

used. The L-curve associated with the inverse problem in the initial condition is shown in figure 8.7. The L-curve gives as an optimal parameter in the initial computation $\lambda = 4.80 \cdot 10^{-6}$ for the inversion from the array sensors and $\lambda = 5.68 \cdot 10^{-6}$ for the inversion from the onboard sensors. The values for the parameters in the corrections vary each iteration but are in the same order of magnitude as for the initial computation. From the L-curve it is evident that the computed λ results in the minimal norm.

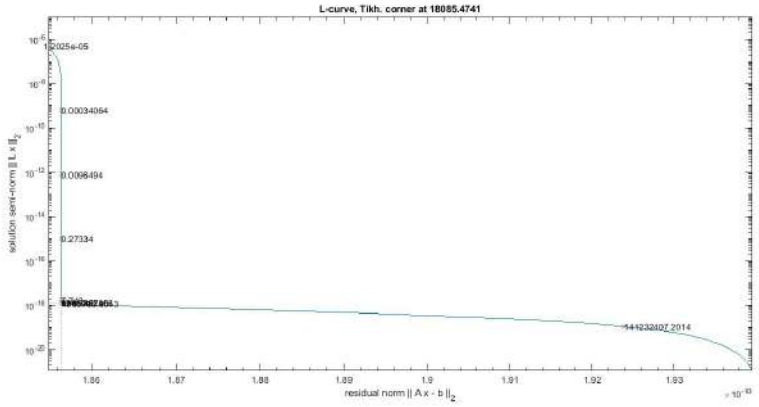

Figure 8.7: L-curve inversion initial condition

In figures 8.9 and 8.10 one can find the results for the model with use of regularization on data set 1. In the prediction of the field at the array, figure 8.9, we find that the prediction has improved significantly compared to the prediction without regularization. The absolute field error decreased from 4.3142 μT to 0.13 nT and the relative field error decreased from 63.8% to 1.72 $\cdot 10^{-3}$%. The shape of the computed field resembles the true field with a very small error, which is very promising.

[1] Enlarged versions of these figures can be found in appendix A.

Figure 8.8: Animation, with regularization, without noise

In figure 8.10 it can be seen that the model is able to correct the permanent magnetization to the true value $\mathbf{M}_{per} = 500\ A/m$. The absolute and relative $x/y/z$ point errors converge to zero, which is a very good improvement. From this we can conclude that the regularization significantly improves the solutions found by the model. We can also conclude that the model is implemented properly and is able to give accurate solutions. Since we have seen that regularization is necessary for the accuracy of the predictions, in all following experiments the Tikhonov regularization is used.

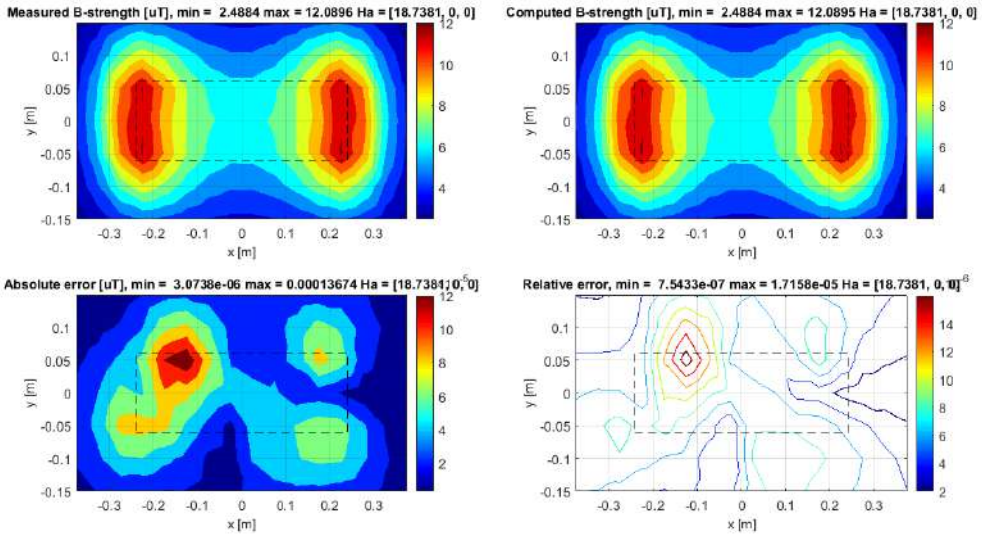

Figure 8.9: Measurements, predictions and errors of the induced field strength with regularization λ = 'free', without noise, with $\mathbf{H}_a$ in x-direction and $\mathbf{M}_{per}^{true}$ 500 A/m in x-direction

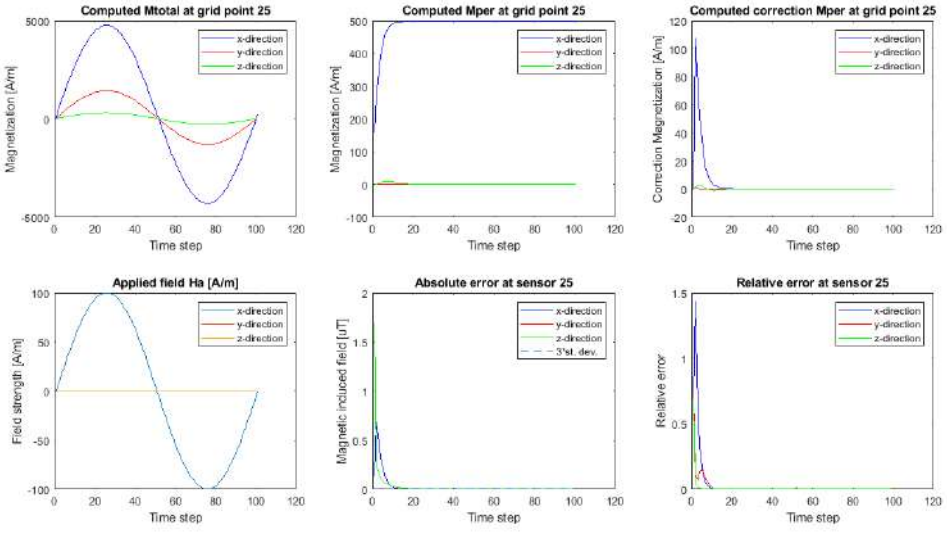

Figure 8.10: Evolution of magnetization and prediction errors over time with regularization λ = 'free' and without noise, $\mathbf{H}_a$ in x-direction and $\mathbf{M}_{per}^{true}$ 500 A/m in x-direction

8.3.2. Data-assimilation

From the previous twin experiment it can be concluded that regularization improves the predictions. These experiments were conducted with use of the model with data-assimilation although it has not yet been proven that the data-assimilation improves the predictions. In order to verify that the data-assimilation indeed satisfies our expectations, the previous twin experiment is redone without correcting the permanent magnetization with data-assimilation. The induced magnetization is still be updated according to the applied field. In figures 8.12 and 8.13 the results can be found for the model without data-assimilation. We compare these figures to the figures 8.9 and 8.10 from the model with data-assimilation.

Figure 8.11: Animation with regularization, without noise and data-assimilation

Although the general shape of the prediction is correct, it can directly be observed that the absolute and relative errors increase significantly when data-assimilation is left out. The maximum absolute error ϵ^s_{abs} increased from 0.13 nT to 1.7354 μT and the maximum relative errors ϵ^s_{rel} increased from $1.64 \cdot 10^{-3}$% to 14.392%, which is a large difference. Note that in figure 8.13 the permanent magnetization indeed is equal to the initial condition at all other time steps. Note that also the pointwise absolute errors ϵ^d_{abs} are constant over time. This is mostly due to the fact that $\mathbf{M}^{true}_{per}$ is constant and therefore the error in the magnetization is constant. However it is very interesting to find that there is clearly no varying error due to the computation of the induced magnetization. In the relative pointwise errors large peaks occur at time steps where the applied field is almost zero. Because the measured fields are close to zero around these points the fixed errors in the permanent magnetization are more clearly visible. From the results it is safe to conclude that it is essential to use the data-assimilation in order to achieve accurate predictions on the magnetic signature.

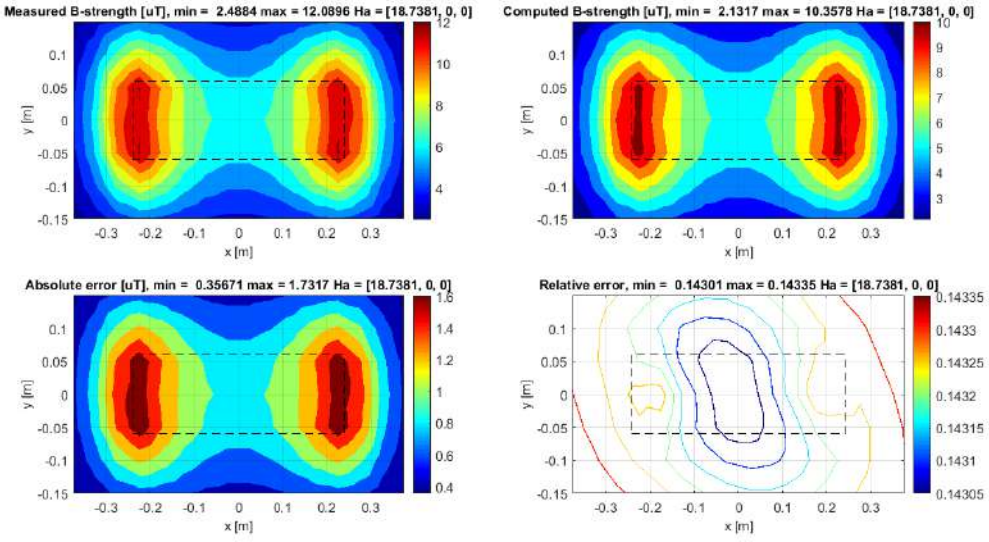

Figure 8.12: Measurements, predictions and errors of the induced field strength with regularization λ = 'free', without noise, with $\mathbf{H}_a$ in x-direction and $\mathbf{M}^{true}_{per}$ 500 A/m in x-direction and without use of data-assimilation

8.3.3. Y- and z-direction

Until this moment all the twin experiments have been conducted with applied fields and magnetizations in the x-direction. For completeness lets consider the y- and z-direction to assure that the model works accurately in these directions as well. We use data sets generated with a constant permanent magnetization of 500 A/m in y- and z-direction respectively. The applied field follows the same sinusoidal pattern as for the x-direction (fig 8.1), but now applied in the y- or z-direction. We still consider data sets without noise to validate that the models are correctly implemented and are able to reconstruct the true parameters accurately in all directions. The results for the y-direction can be found in figures 8.14 and 8.15. The results for the z-direction can be found in figures 8.16 and 8.17.

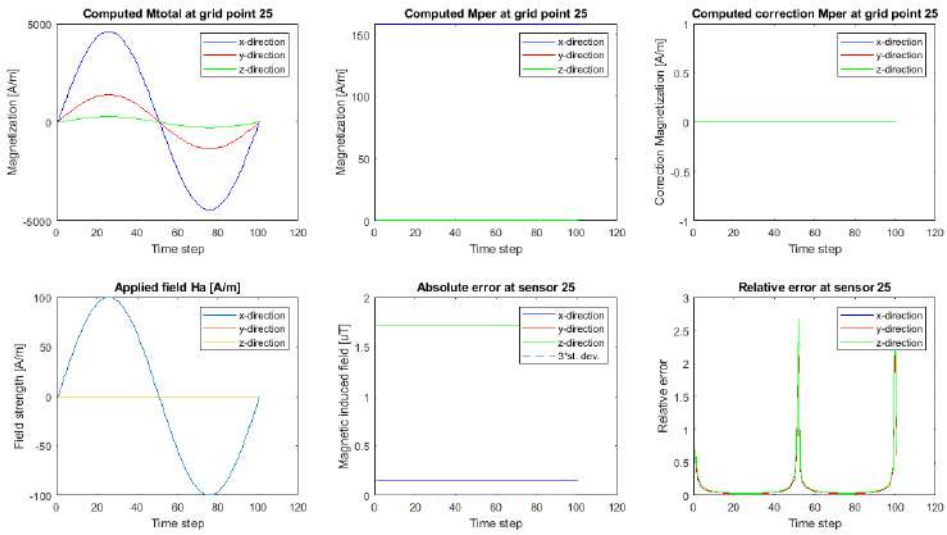

Figure 8.13: Evolution of magnetization and prediction errors over time with regularization λ = 'free' and without noise, $\mathbf{H}_a$ in x-direction and $\mathbf{M}_{per}^{true}$ 500 A/m in x-direction without use of data-assimilation

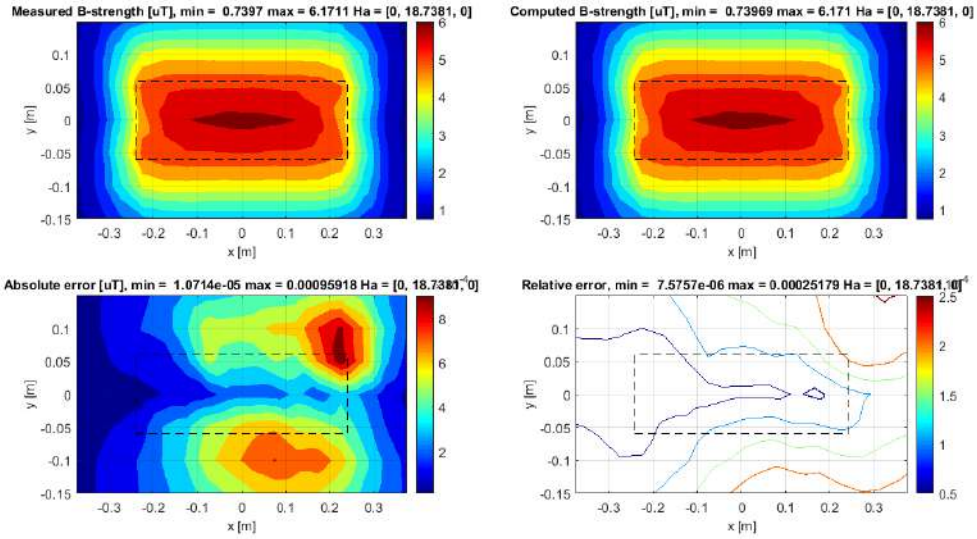

Figure 8.14: Measurements, predictions and errors of the induced field strength with regularization λ='free', without noise, with $\mathbf{H}_a$ in y-direction and$\mathbf{M}_{per}^{true}$ 500 A/m in y-direction

For both the $y-$ and $z-$direction it is found that the relative and absolute field errors are small and the model is able to reconstruct $\mathbf{M}_{per}^{true}$ accurately. Interestingly, the errors are slightly higher than for the $x-$direction. An explanation for the slightly higher errors can be found in the computed permanent magnetizations. The initial estimates for $\mathbf{M}_{per}$ are lower for the $y-$ and $z-$direction than for the $x-$direction and the model needs more steps to be able to converge to the true values. This can also explain that the maximum absolute field errors are still slightly higher than for the $x-$direction, since the estimates is still converging. The relative and absolute point errors still almost converge to zero and the corrections on the permanent magnetization truly converge to zero. Although it might be of interest to find out why the inversions are less accurate in the $y-$ and $z-$directions, it is not unexpected that the results are slightly different for each direction, since the orientation between the field and the box is different. Note that the relative errors are still below 0.15%, which can be considered very accurate. From these observations it can be concluded that the model works properly in all three directions. Therefore it is acceptable to only focus on applied fields and

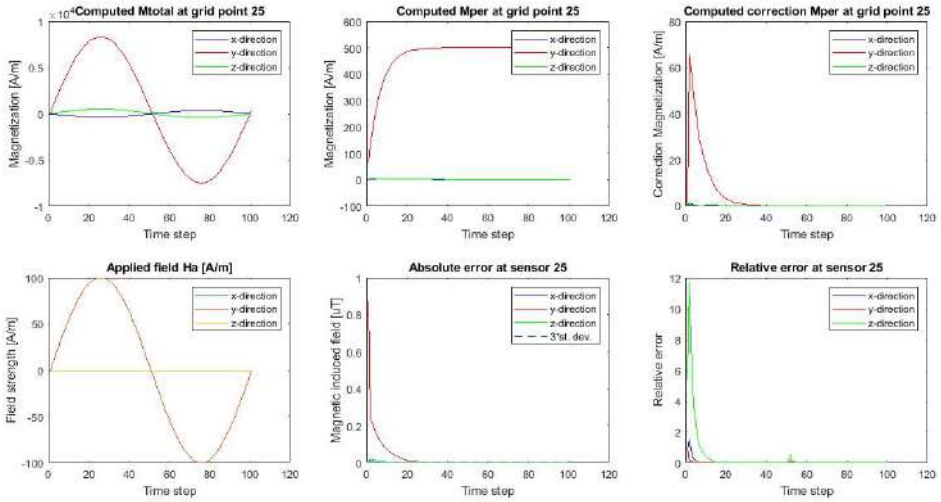

Figure 8.15: Evolution of magnetization and prediction errors over time with regularization λ = 'free', without noise, $\mathbf{H}_a$ in y-direction and $\mathbf{M}_{per}^{true}$ 500 A/m in y-direction

magnetization in the $x-$direction in the next experiments.

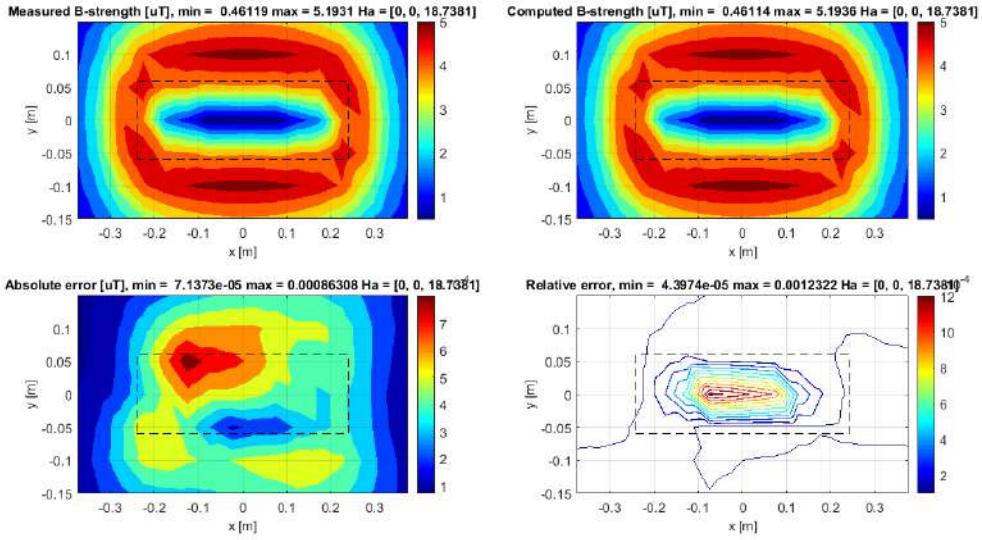

Figure 8.16: Measurements, predictions and errors of the induced field strength with regularization λ = 'free', without noise, with $\mathbf{H}_a$ in z-direction and $\mathbf{M}_{per}^{true}$ 500 A/m in z-direction

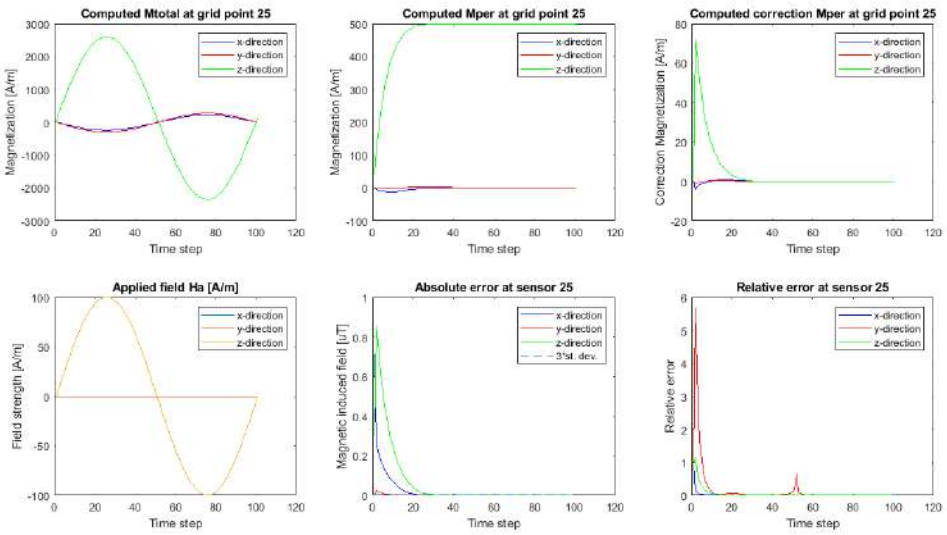

Figure 8.17: Evolution of magnetization and prediction errors over time with regularization λ = 'free', without noise, $\mathbf{H}_a$ in z-direction and $\mathbf{M}_{per}^{true}$ 500 A/m in z-direction

8.4. Conclusion phase I

In this section a short summary and conclusion of the conducted twin experiments in phase 1 are given. These first twin experiments are based on data set 1: a data set, constructed with fixed permanent magnetization and without added noise to the measurements. To gain insight into the influence of regularization the model without and with regularization is used. For the model without regularization it was found that the initial estimate of $\mathbf{M}_{per}$ contained large variations and that the estimate of $\mathbf{M}_{per}$ did not converge to the true values with help of the data-driven updates. The inaccuracies in the estimates lead to large absolute field errors ϵ_{abs}^{s} of 4.3142 μT at $\mathbf{H}_a$ = 18.7381 A/m.

Next the model with Tikhonov regularization is used on the same data set. It is observed that a higher parameter λ results in a more uniform estimate of $\mathbf{M}_{per}$. In order to find an optimal parameter the L-curve is used. The results of the model with regularization are far better than for the model without. The maximum absolute field error ϵ_{abs}^{s} decreased to only 0.13 nT, which is a very good improvement. Further it is observed that the estimate for the permanent magnetization converges to the true values, by data-driven corrections. From the experiments it is concluded that it essential to use regularization in order to achieve accurate estimates.

To assure that the data-driven updates truly improve the estimate of the permanent magnetization, a model without the updates is used. From this experiment it is directly concluded that the results are far less accurate and that the data-driven updates are indeed necessary for accurate predictions.

At last two twin experiments were conducted to find if the model works properly in the $y-$ and $z-$direction as well. It is concluded that although in these directions the model needs a few more time-steps to be able to correct $\mathbf{M}_{per}$ to the true values, the predictions are still very accurate. To sum up, from the experiments in the first part it is concluded that the use of regularization and data-driven updates are essential for accurate predictions and that the model seems to be working properly.

8.5. Phase II.1: Fixed permanent magnetization with noisy data

In this phase we test the performance of the prediction model on noisy data to find how well the model deals with perturbations in the received data. Especially with the large number of inversions in the model, it is important to have knowledge on how well the model can handle perturbations in the inversions. Therefore we use data sets contaminated with Gaussian white noise. As mentioned in section 8.2 a standard deviation of $2 \cdot 10^{-7} \mu T$ is chosen for the generation of noise in order to achieve a noise of $1\ \mu T$ in each sensor. In figures 8.19 and 8.20 the result of the prediction model are shown.

Figure 8.18: Animation with regularization, noise $2 \cdot 10^{-7}$

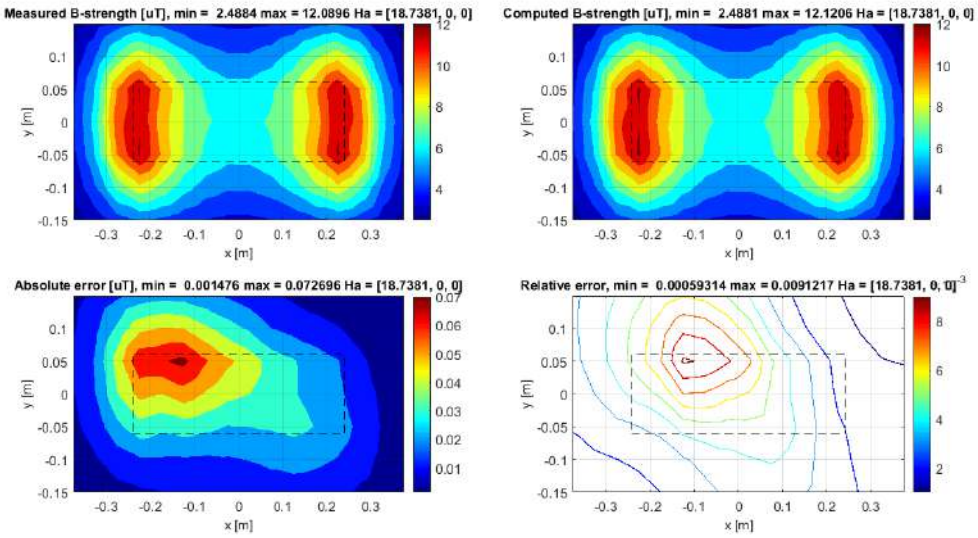

Figure 8.19: Measurements, predictions and errors induced field strength with regularization λ = 'free', noise = $2 \cdot 10^{-7}$, $\mathbf{H}_a$ in x-direction and $\mathbf{M}_{per}^{true}$ 500 A/m in x-direction

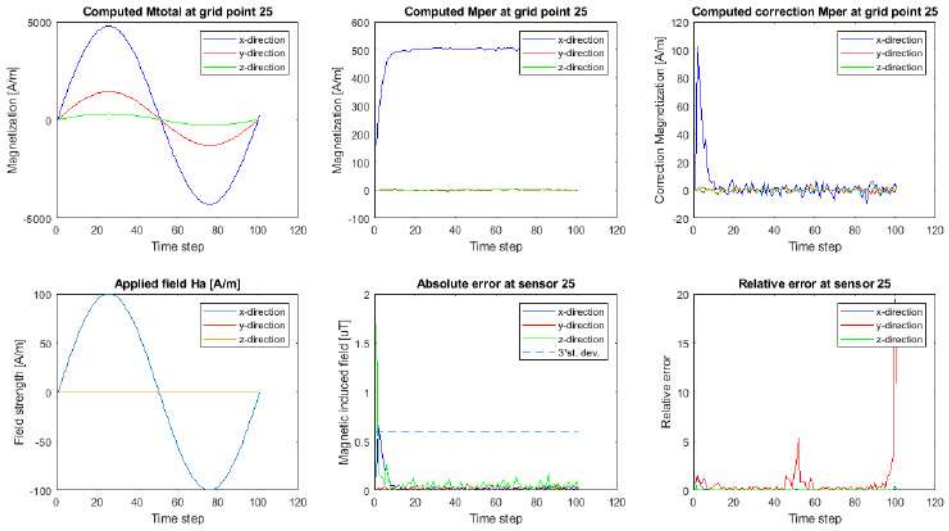

Figure 8.20: Evolution of magnetization and prediction errors over time with regularization λ = 'free', noise = $2 \cdot 10^{-7}$, $\mathbf{H}_a$ in x-direction and $\mathbf{M}_{per}^{true}$ 500 A/m in x-direction

As expected the results are less accurate than for the data set without noise. The maximum absolute field error has increased from 0.13 nT to 0.027 μT, which is a large increase. However this error is still acceptable on a field strength of 2.49 to 12.12μT. Remember that the noise in each sensor is approximately 1 μT, results with an absolute error of only 0.027 μT show that the model is able to handle noise in a correct, accurate way. The perturbations in the measurement are clearly dampened by the model, note that this is due to the filter factors in the regularization. From figure 8.20 it can be seen that the model is still able to approximate the true value $\mathbf{M}_{per}^{true}$, although the noise is slightly translated into the estimate of $\mathbf{M}_{per}$. In the figure with the absolute $x/y/z$ error an extra line is drawn at the height of 3σ, showing that the absolute errors in the magnetic fields are significantly lower than the noise introduced in the measurements.

In the relative $x/y/z$ error plot high peaks occur at certain time steps. To investigate the origin of these peaks we plot the measured and computed field at sensor 25 over time together with both errors, see figure 8.21. From this figure the following two observations are made: First the computed field at the sensor and the absolute errors do not show strange behaviour or large errors and secondly the peaks occur at the moment that the measured and computed fields are approximately zero ($10^{-10} - 10^{-9}$). Since the order of the noise ($10^{-7} - 10^{-6}$) is larger than the order of the fields it is very likely that the peaks in the relative error arise due to the level of the noise and not due to inaccuracies of the model. Therefore conclusions are drawn mainly from the absolute errors and the relation of the absolute errors to the level of noise. From the twin experiment it can be concluded that although the noise components are slightly visible in the estimates and the predictions, the model is able to dampen their contributions are compute accurate predictions.

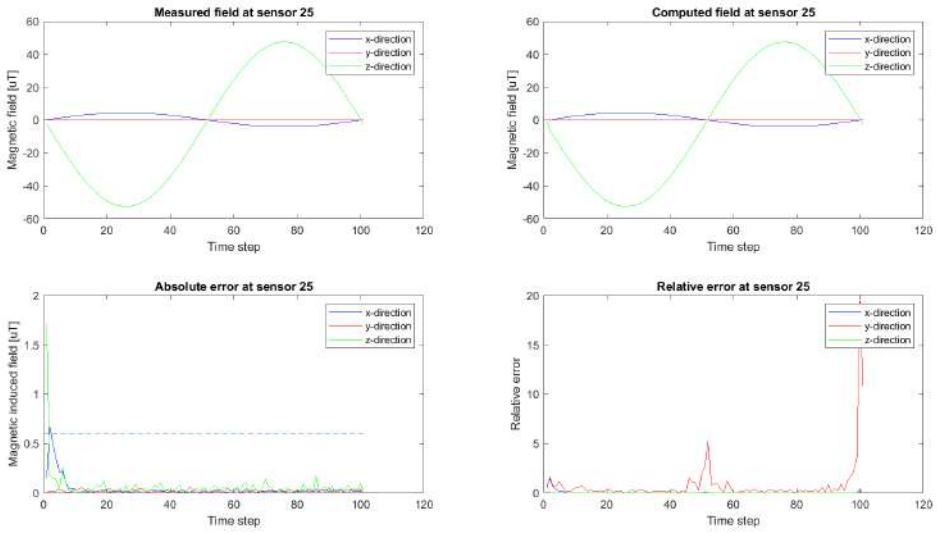

Figure 8.21: Measured and computed magnetic fields and relative/absolute errors at sensor 25, λ = 'free', noise = $2 \cdot 10^{-7}$, $\mathbf{H}_a$ in x-direction and $\mathbf{M}_{per}^{true}$ 500 A/m in x-direction

8.6. Phase II.2: Model adaptions

In this section two improvements are proposed and tested. First an improvement for the computation of the induced magnetization is discussed and secondly an improvement for the initial estimate of the permanent magnetization is discussed.

8.6.1. Induced magnetization

Remember from section 6.1.2 that there are two different options for the induced magnetization at each time step. Either the induced magnetization is computed from the applied field at time step k and the permanent magnetization at time step $k-1$. Or we add an extra computation of the induced magnetization based on the corrected permanent magnetization at time step k. The first option is denoted by $\mathbf{M}_{ind}^{k-1}$ and the second by $\mathbf{M}_{ind}^{k}$.

The two computations of the induced magnetization are compared using data sets 1 and 4 (fixed permanent magnetization with and without noise). Both cases are compared on basis of two errors. First the maximum absolute field errors ($\max \epsilon_{abs}^{s}$) are compared since these values show the order of the largest deviation in one sensor at a certain time interval. Secondly they are compared on basis of the sum over all time steps and all sensors:

$$\varepsilon_{tot} = \sum_{t=1}^{101} \sum_{s=1}^{112} \varepsilon_{abs}^{s,t},$$

which gives insight into the total error. We refer to this error as the total error. Lets start for the case without noise with the model with $\mathbf{M}_{ind}^{k-1}$.

The maximum absolute error field found is 0.13 nT and the total error is 193.322μT. When the second model is used the maximum absolute field error increases to 0.27 nT and the total error increases to 309.4 μT, which is a large increase. The model where the induced magnetization at time step k is based on the permanent magnetization at time step $k-1$ seems better for this data set. Now lets consider the data set with noise. Here the maximum absolute field error decreases from 0.073 μT to 0.013 μT, which is a large improvement. The total error decreases from 481.3 μT to 418.66 μT. From these values it is difficult to draw concrete conclusions on the influence of this model change, since it seems to improve for data with noise and get worse for data without noise.

In order to find if there is a significant constant improvement, figure 8.22 shows the maximum absolute field errors for both data sets at each time step for both $\mathbf{M}_{ind}^{k}$ as $\mathbf{M}_{ind}^{k-1}$. In figures 8.22a and 8.22b the maximum errors for the data set without noise can be seen. From these figures we observe that at one time step the model with the additional update is better and at time steps the model without, but at the end they converge to the approximately the same maximum absolute error. From these figures we can not draw any conclusions that one model is significantly more accurate than the other. In figure 8.22c the maximum absolute field errors are shown for the data set with noise. From this figure it is evident that the model with the additional update of $\mathbf{M}_{ind}$ has a lower maximum absolute field error at almost each time step. Due to the application of this model in naval ships it is important to have knowledge on the maximum absolute field error. Moreover in practice the data is always contaminated with noise, such that the results from the data set with noise are more important. When the maximum absolute field error is as small as possible this decreased the risk of detonation of a naval mine. Therefore we conclude that the model with the additional $\mathbf{M}_{ind}$ update gives more accurate predictions when the data set is contaminated with noise and that this update is added to the model.

8.6.2. Initial condition

From the evolution of the permanent magnetization it is evident that the solution of the inversion in the initial estimate is very inaccurate. For the estimation of the initial condition two direct inversions are done, from both the array sensors and the onboard sensors, see section 6.1.1. The performance of the model might be increased by improving the initial estimate.

One way to try to improve the estimate is to compute corrections for the permanent magnetization on basis of the same set of measurements from the onboard sensors at time step zero. Note that the measurements from the array sensors could also be used, but for now we only use the onboard sensors. The update is com-

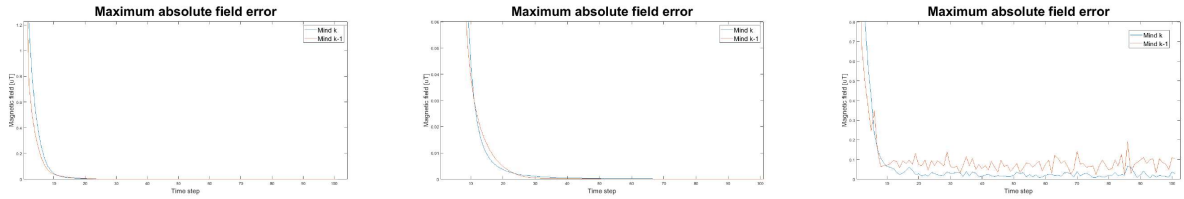

(a) Set without noise (b) Set without noise, zoomed (c) Set with noise $2 \cdot 10^{-7}$.

Figure 8.22: Maximum absolute field errors for model with and without extra $\mathbf{M}_{ind}$ update for constant permanent magnetization with λ = 'free'[2]

puted according to the method described in section 6.1.2. The number of iterations k, in which we update the initial estimate, needs to be defined, which can be done in two different ways. Either k is a fixed number, based on trial and error. Or it is defined variably, based on a certain tolerance level for the error in the field estimate: if $\| \mathbf{B}_{res}(k) \|_2 < \varepsilon_{tol}$, stop. First take k a fixed number to examine if corrections on the permanent magnetization are able to improve the initial condition.

In figure 8.23 the computed initial conditions are shown for different values of k with λ = 'free'. It is evident from the figure that the use of corrections improves the estimate of the magnetization. With one correction the estimate has already improved with almost $100 A/m$ and with $k = 20$ the estimate shows a good approximate of the true $\mathbf{M}_{per}$. Note that the regularization parameter is chosen optimally in each iteration, making it possible to gain more information from the data each iteration step. This also explains the fact that the solutions get less uniform with more iterations. In order to get a solution that better fits the data the influence of the regularization term is decreased.

Mathematically speaking it is interesting to find out whether it is also possible to improve the solution by iterations with a fixed lambda. Remember that we are solving the Tikhonov functional:

$$\min_{\mathbf{x}} \{ \| A\mathbf{x} - \mathbf{b} \|_2^2 + \lambda^2 \| R\mathbf{x} \|_2^2 \}, \tag{8.4}$$

and this functional has an equivalent least squares formulation. The found solution is believed to be the best possible solution, since it is the solution of a least-squares problem. The remaining residual is part of the solution which can not be computed from the data. Therefore we would not expect multiple iterations, with a fixed lambda, to improve the estimate.

However from figure 8.24 it is evident that the solution improves and becomes more uniform with more iterations. An explanation for this behaviour might be found in the formulation 8.4, in the first iteration the contribution due to the term $\| A\mathbf{x} - \mathbf{b} \|_2^2$ is most important. Such that the solution mainly minimizes the first part, resulting in a less uniform solution. In the next iterations the values of $\mathbf{b}$ are replaced by $\mathbf{b}_{res}$ decreasing the values of the first term and thereby giving more room for the minimization of the second regularization term. This could indeed result in more uniform solutions. However it is still very interesting that it is thereby able to correct the initial estimate almost to the true value. For now we unfortunately can not look further into this, but it is very interesting to conduct more research on this behaviour.

For this research the main question is if the improvement of the initial condition is present in the field predictions. In order to conclude if the better initial estimate improves the predictions we consider the maximum absolute field error at each time step and the total error defined in the previous section. The maximum absolute field errors over time can be seen in figures 8.25 and 8.26. We look at four different values for k, $k = 0, 1, 5, 10$, where $k = 0$ is the standard model without updates in the initial condition. For both with and without noise it can be observed that the absolute maximum field errors are significantly lower in the first 20 time steps if more updates are used in the initial estimate. For the data set without noise this difference stays present, although the errors all seem to converge to the same error ($\sim 10^{-5} \mu T$). However for the data set with noise after 20 time steps the data assimilation steps have been able to improve the less accurate initial estimates and each model gives the same level of accuracy. Even in the zoomed figure, 8.26b it is evident that there is no significant influence of the iterations in the initial condition. This behaviour is visible in the total

[2] Enlarged versions of these figures can be found in appendix A.

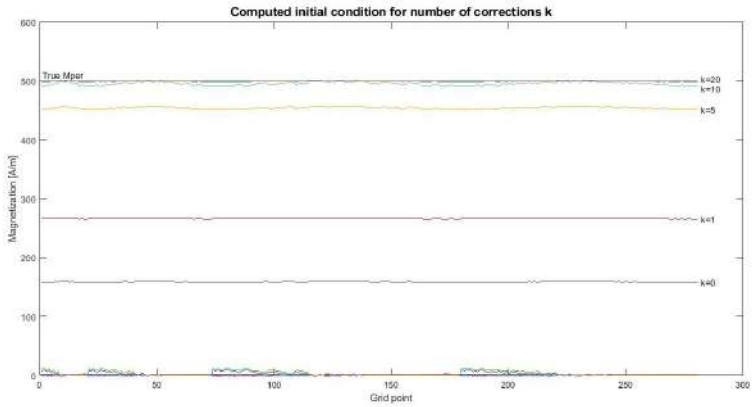

Figure 8.23: Initial conditions for different values of k for simulation data with constant $\mathbf{M}_{per}$ 500 A/m in $x-$direction without noise and with regularization with λ = 'free'.

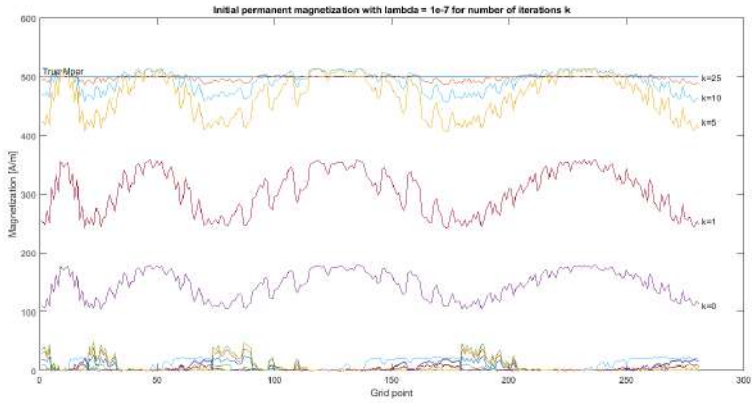

Figure 8.24: Initial conditions for different values of k for simulation data with constant $\mathbf{M}_{per}$ 500 A/m in $x-$direction without noise and with regularization with $\lambda = 2 \cdot 10^{-7}$.

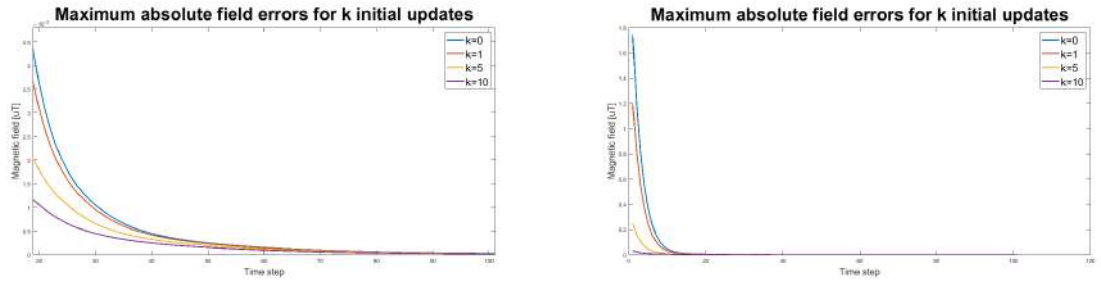

(a) Complete figure

(b) Zoomed figure

Figure 8.25: Maximum absolute field errors for model with and without extra iterations k in the initial estimate for constant permanent magnetization with λ = 'free' without noise

errors as well. For the data without noise the total error for $k = 0$ iterations is 310.8μT, while for $k = 10$ iterations the total error has decreased to 6.1μT. Note that this large decrease in total error is mainly to the first 20 time steps. For the data with noise the error decreases from 422.0 μT to 128.6 μT. Here the error is decreased less, which is due to the fact that after 20 iterations, the maximum absolute errors are approximately equal.

From these observations we can conclude two statements. First it is positive to find that the accuracy of the initial condition has no influence on the predictions from a certain time step if there is noise present in the

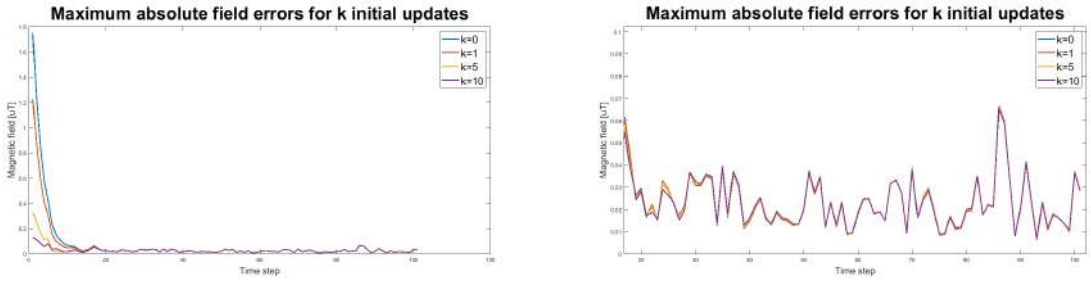

(a) Complete figure

(b) Zoomed figure

Figure 8.26: Maximum absolute field errors for model with and without extra iterations k in the initial estimate for constant permanent magnetization with λ = 'free' with noise

data. In practice data is always contaminated with noise and therefore we find that it is not essential to be able to compute very accurate initial estimates, which could save time and money. Further we can conclude that addition of data-driven iterations in the computation of the initial permanent magnetization improves the initial estimate. Logically the addition of data-driven iterations increases the computational time of the initial estimate. For these reasons we will not use the additional iterations in the coming twin experiments.

8.7. Conclusion phase II

In the second part the generated data was contaminated with noise, to find the performance of the model and especially the inversions when dealing with noise. It was found that although the predictions of the magnetic induced field are less accurate for the contaminated data, the errors are still far below the noise level. It is observed that due to the noise components the estimate of $\mathbf{M}_{per}$ no longer converges to the true value but keeps changing slightly. From the experiment it can be concluded that the model is able to handle the noise in a correct and accurate way.

In the second half of part 2, two model adaptions are discussed. The adaptions are tested on both data sets with and without noise. First it was proposed to add another computation of the induced magnetization after the permanent magnetization was updated instead of only using the permanent magnetization from the previous time step. It is concluded that for the data set without noise the adaptions does not have much influence on the maximum absolute field error, whereas it results in a large decrease in the maximum absolute field error for the data set with noise. Since the adaption gives better results for the data set with noise, it is added to the model.

The second adaption is to improve the initial estimate of the permanent magnetization. In this adaption, a number of corrections on $\mathbf{M}_{per}$ are done based on the measurements of the first time step. Interestingly, these additional corrections result in a large improvement of the initial estimate. However it is also observed that the improved initial condition does not have an influence on the prediction of the magnetic signature after 20 time steps. Since the additional updates largely increase the computational time, we have decided for now not to include them in the model. However the results from this adaption must certainly not be forgotten.

8.8. Phase III.1: Magnetic hysteresis

So far we have only used data sets generated with a constant permanent magnetization. However it is known that the permanent magnetization changes depending on the applied field according to the discussed hysteresis loop. In the next twin experiments we test how well the prediction model is able to track a varying permanent magnetization. This varying permanent magnetization is designed such that the total magnetization simulates the hysteresis loop, discussed in section 3.1. In figure 8.28 the true magnetization is set against the applied field, showing a hysteresis like loop. Note that at $\mathbf{H}_a = 0$ all lines have the same linearity coefficient but are on a slightly different height due to the permanent magnetization. Also it is not an exact loop as in chapter 3, due to the definition of the permanent magnetization. However this is not a problem since the loop shows the same behaviour as a true hysteresis loop and therefore we can draw correct conclusions on the performance of the model. Although we hope to find that the model is also able to track the permanent magnetization, it is most important that the model is able to give accurate predictions of the induced field at the sensor array. In figures 8.29 and 8.30 the results of the prediction model can be found.

Figure 8.27: Animation magnetic hysteresis

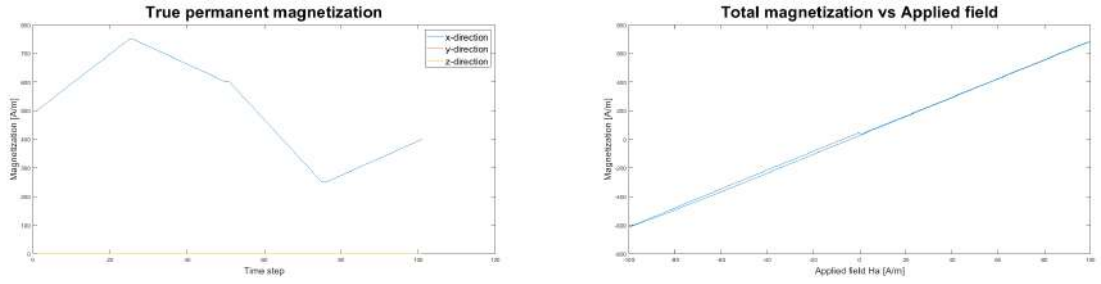

(a) True permanent magnetization

(b) True total magnetization

Figure 8.28: Hysteresis loop $\mathbf{M}^{true}$

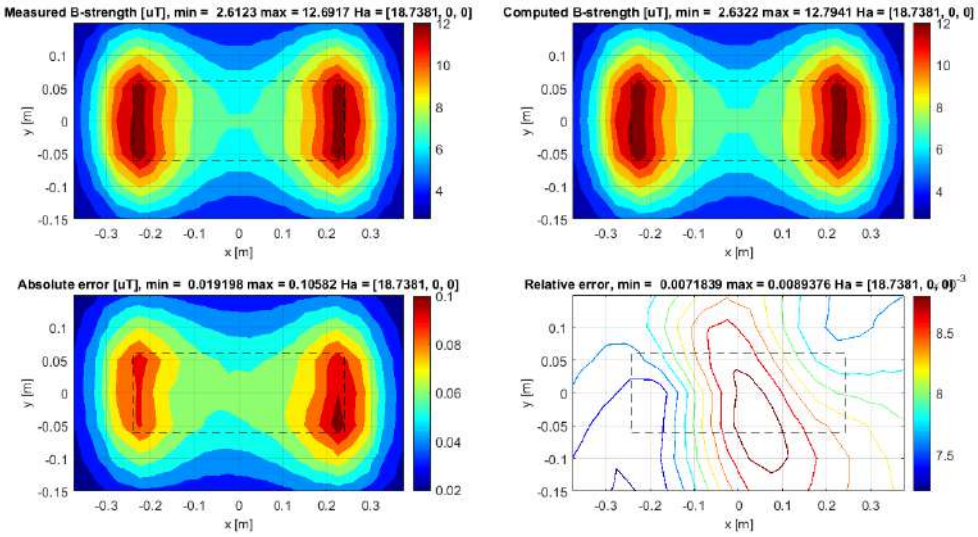

Figure 8.29: Measurements, predictions and errors induced field strength with regularization λ = 'free', noise = $2 \cdot 10^{-7}$, $\mathbf{H}_a$ in the x-direction and $\mathbf{M}_{per}^{true}$ in x-direction according to the hysteresis loop (fig 8.28)

From figure 8.29 it can be observed that the predicted fields are quite similar to the measured fields and the maximum absolute field error is 0.106 μT. From this figure it can be noticed that the absolute errors seem field strength dependent, if a larger field is present the errors are larger as well. However from a more

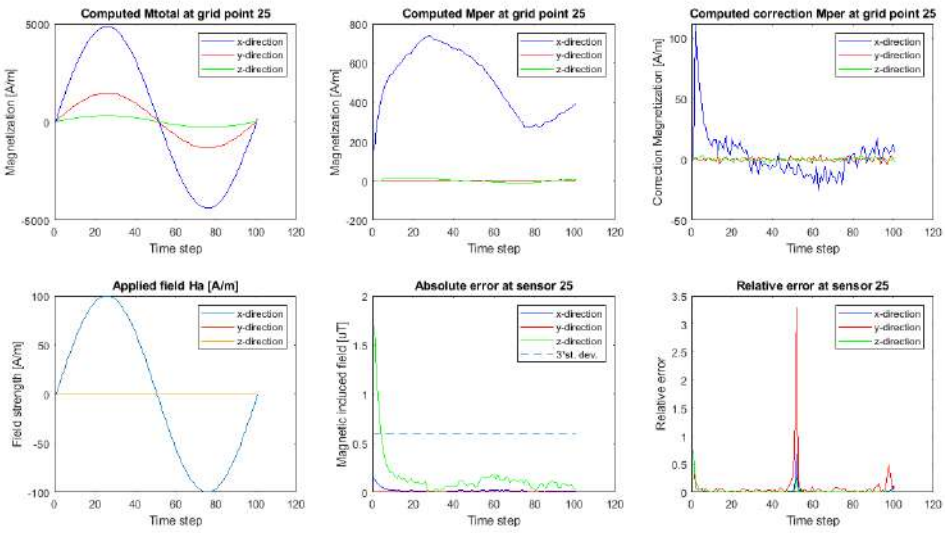

Figure 8.30: Evolution of magnetization and prediction errors over time with regularization λ = 'free', noise = $2 \cdot 10^{-7}$, $\mathbf{H}_a$ in x-direction and $\mathbf{M}_{per}^{true}$ in x-direction according to the hysteresis loop (fig 8.28)

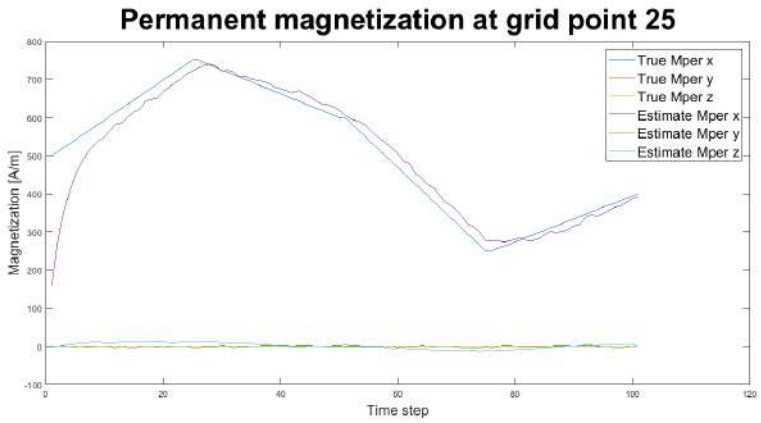

Figure 8.31: Comparison estimated $\mathbf{M}_{per}$ with true $\mathbf{M}_{per}$ at grid point 25 for λ = 'free' and noise = $2 \cdot 10^{-7}$

detailed analysis over time (not shown here) these errors do not increase/decrease significantly if the applied field and therefore the induced fields increase/decrease. The present error is probably caused by the noise components in the measured fields. Compared to previous twin experiments the errors in the predictions are larger. This is likely caused by the fact that the estimated permanent magnetization is not able to converge to the true permanent magnetization, since the true values are varying as well. From the results in figure 8.30 it can be seen that the absolute errors are still below the noise level of $6 \cdot 10^{-7}$ per direction. Observe that the estimate of the permanent magnetization is approximately linearly varying. To assure that this variation is also approximating the true values of $\mathbf{M}_{per}$, see figure 8.31. From this figure it is evident that the model is able to predict the permanent magnetization very well, although it has a slight delay in the computation. From all observations it can be concluded that the model is able to track a varying permanent magnetization and give predictions with an accuracy of around 0.1 μT.

8.9. Phase III.2: Non-uniform permanent magnetization

In the previous experiment the promising ability of the model to track a varying permanent magnetization was found. So far we have assumed that the permanent magnetization is uniform over the object. However in practice the permanent magnetization is non-uniform due to previous external influences like stress. To test the ability of the model to work with non-uniform magnetization, the next twin experiment is conducted.

We still expect the permanent magnetization to have a certain smoothness over the object and therefore we define the permanent magnetization of a grid point on basis of the $x-$coordinate of that point. Grid points with the same $x-$coordinate have the same permanent magnetization, close by grid points have a slightly different $x-$coordinate and thereby a slightly different permanent magnetization and grid points further away have different permanent magnetization. The permanent magnetization is constructed by the absolute value of a sine depending on the $x-$coordinate, such that it varies between 0 and 750 A/m. In figure 8.35a the arrows show the true permanent magnetization. The permanent magnetization is now stronger at the beginning and the ends of the SVP01 than at the middle. The coloured triangles show the divergence of the magnetization, which is at this moment less interesting. Using the defined permanent magnetization, simulation data is constructed with standard deviation $\sigma = 2 \cdot 10^{-7}$ for the noise component. The results for the model with regularization parameter λ = 'free' can be found in figures 8.33 and 8.34.

Figure 8.32: Animation non-uniform permanent magnetization, λ = 'free'

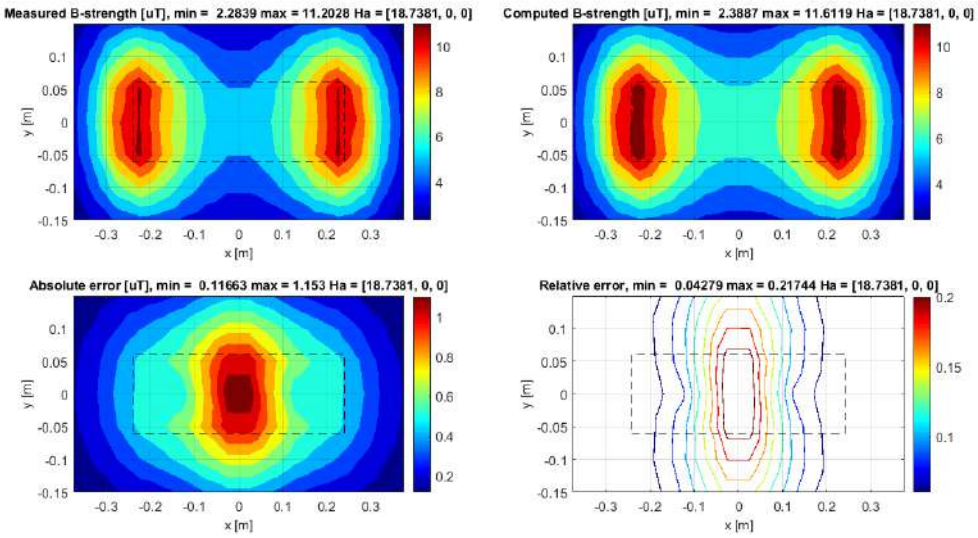

Figure 8.33: Measurements, predictions and errors induced field strength with regularization λ = 'free', noise = $2 \cdot 10^{-7}$, $\mathbf{H}_a$ in the $x-$direction and $\mathbf{M}_{per}^{true}$ non-uniform in x-direction.

From the figures it is directly visible that the predictions are less accurate than in the experiments before, the maximum absolute field error is 1.153 μT. This is about 10 times more than for the varying $\mathbf{M}_{per}$. Especially in the middle below the box the error is high, this rises the question as to whether the estimated magnetization is indeed non-uniform. In figure 8.35b the estimated permanent magnetization is shown by the arrows. When compared to figure 8.35a it can be observed that the estimated permanent magnetization is much higher than the true value. This can be the cause of the high errors in the center. To gain more insight on the estimated permanent magnetization, figure 8.41 shows the estimated and the true permanent magnetization at time step 100 for all grid points. From this figure it is clear that there has been too much regularization in the estimation, as it can not variate enough for the non-uniformity. Even though the L-curve should be able to find the parameter λ that minimizes the Tikhonov criterion, we try to find a better prediction by giving the model more freedom. The L-curve finds values for the parameter λ in the order $4-6 \cdot 10^{-6}$, apparently this parameter requires too much regularity for the preferred solution. For the regularization parameter $\lambda = 5 \cdot 10^{-8}$ is used in order to give the model more freedom to fit the data instead of the regularity.

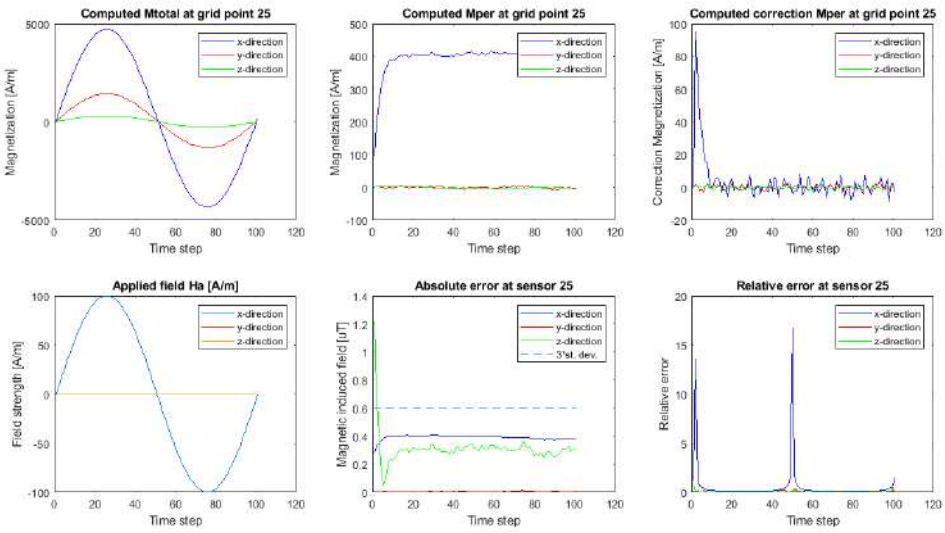

Figure 8.34: Evolution of magnetization and prediction errors over time with regularization λ = 'free', noise = $2 \cdot 10^{-7}$, $\mathbf{H}_a$ in x-direction and $\mathbf{M}_{per}^{true}$ non-uniform in $x-$direction.

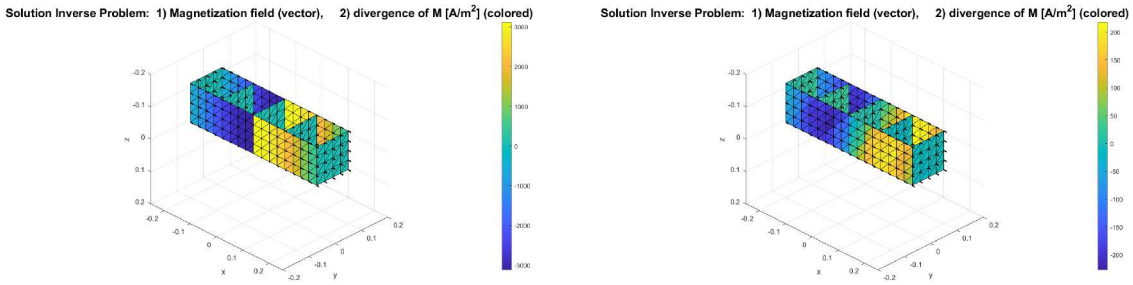

(a) True non-uniform magnetization and divergence

(b) Estimated non-uniform magnetization and prediction.

Figure 8.35: True and estimated non-uniform $\mathbf{M}_{per}$ and divergence with λ = 'free' and noise = $2 \cdot 10^{-7}$ [3]

Figure 8.37: Animation for nun-uniform permanent magnetization, $\lambda = 5 \cdot 10^{-8}$

The results can be found in figures 8.38- 8.41.Fortunately with the smaller regularization parameter the maximum absolute field error is brought back to 0.074 μT, which is of the same order as we have seen before. Also the absolute errors in the individual directions are again far below the noise level as desired. From figures 8.40b and 8.41 it is evident that the extra freedom in the regularization results in better approximations of the permanent magnetization and also in better predictions. It must be noted that this twin experiment shows that for non-uniform magnetization the L-curve cannot be trusted to find the optimal parameter. For a fact there might be a different value than $\lambda = 5 \cdot 10^{-8}$ which can result in even better predictions. Since the magnetization is non-uniform in practice it is necessary to find a different method for the computation of the regularization parameter if optimal predictions are desired.

From the twin experiment it can be concluded that the model is able to give accurate predictions on a non-uniform magnetization. However the regularization parameter must be small enough ($\sim 10^{-8}$) in order to give the model enough freedom to fit the uniformity. The L-curve, in this case, does not find the optimal value for λ. Since non-uniform permanent magnetization are standard in practice, another method must be found to compute an optimal regularization parameter.

[3] Enlarged versions of these figures can be found in appendix A.

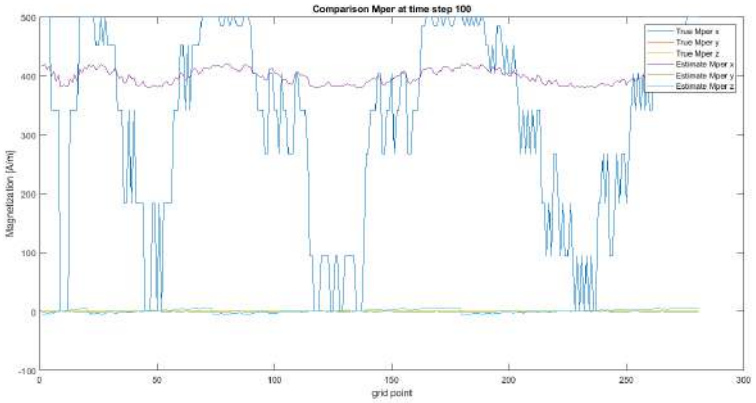

Figure 8.36: Comparison estimated $\mathbf{M}_{per}$ with true $\mathbf{M}_{per}$ at time step 100 for λ = 'free' and noise = $2 \cdot 10^{-7}$.

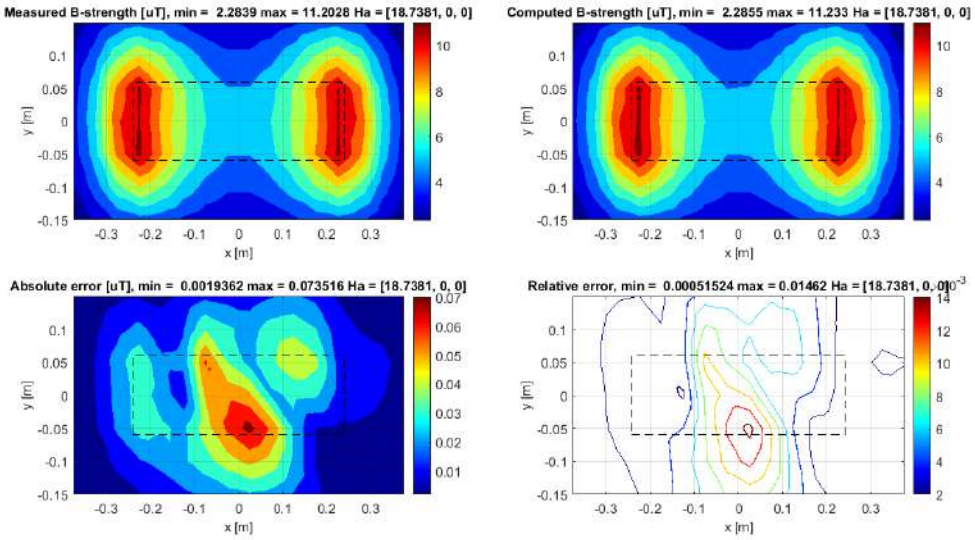

Figure 8.38: Measurements, predictions and errors induced field strength with regularization $\lambda = 5 \cdot 10^{-8}$, noise = $2 \cdot 10^{-7}$, $\mathbf{H}_a$ in the $x-$direction and $\mathbf{M}_{per}^{true}$ non-uniform in x-direction.

8.10. Phase III.3: Unknown susceptibility distribution

Until now we have assumed that the distribution of the susceptibility is completely known and uniform 100. In practice this is not the case, the susceptibility can only be estimated. With the assumption that the susceptibility is known, the true performance of the model could be tested. In the previous experiments we showed that the model is able to cope with linear varying and non-uniform distributions of $\mathbf{M}_{per}$. Now it is time to push the boundaries of the model by removing the assumption that χ is known. It is of our interest to research whether (small) errors in the susceptibility estimate influence the prediction of the magnetic signature. It might be possible that the data-assimilation is able to correct small errors in the susceptibility as well. If this is true it will improve the applicability of the model. In [22] a magnetic susceptibility estimation method is designed which is able to approximate the susceptibility distribution. Unfortunately due to time-reasons it has not been possible to specify this method for the SVP01. To still be able to research the influence of inaccurate susceptibility estimations, we specify different estimates for the susceptibility distribution and compute the predictions.

Remember that the value of χ at each element is used in the computation of matrix D, see equation 4.9. In the generation of the simulation data an uniform susceptibility distribution of 100 is used: $\chi_{true} \equiv 100$. In the computation of the initial estimate we add an initial estimate for χ of the following form: $\chi_{est} \equiv \text{randnrm}(\mu, \tau)$,

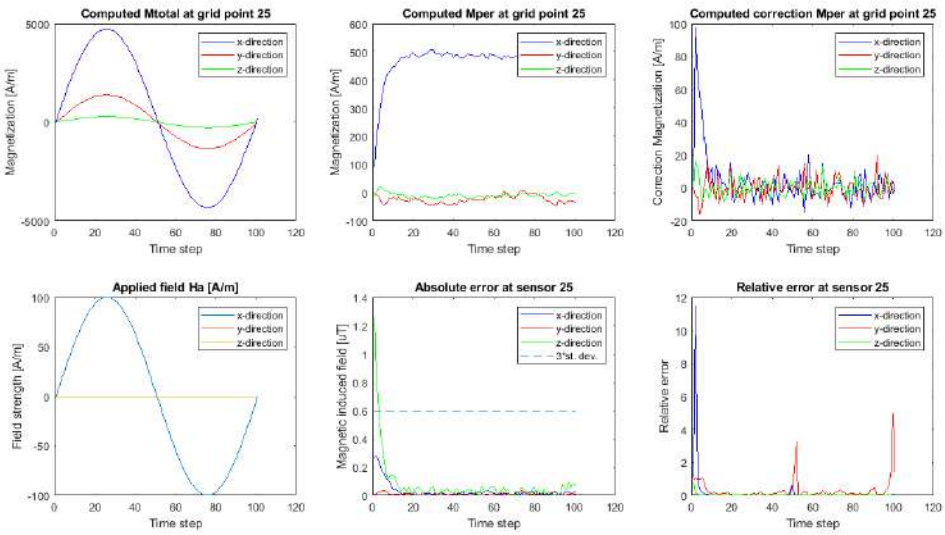

Figure 8.39: Evolution of magnetization and prediction errors over time with regularization $\lambda = 5 \cdot 10^{-8}$, noise = $2 \cdot 10^{-7}$, $\mathbf{H}_a$ in x-direction and $\mathbf{M}_{per}^{true}$ non-uniform in $x-$direction.

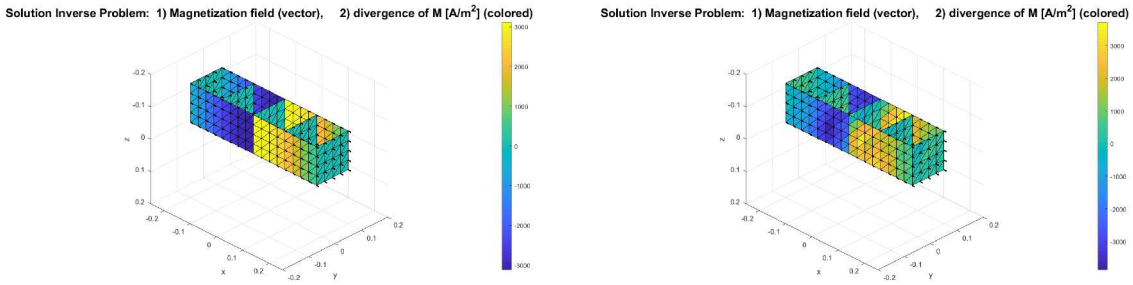

(a) True non-uniform magnetization and divergence

(b) Estimated non-uniform magnetization and prediction.

Figure 8.40: True and estimated non-uniform $\mathbf{M}_{per}$ and divergence with lambda = $5 \cdot 10^{-8}$ and noise = $2 \cdot 10^{-7}$.

here μ is the mean and τ the standard deviation. Using this χ_{est} the new matrix D is generated, after which the predictions are computed. First an estimate with $\mu = 100, \tau = 5$ is used, resulting in a distribution with values between 85 and 115 (-3τ to 3τ). In [22] a true chi distribution of a steel plate ranging from 40 - 100 could be estimated with a range of ± 3. Since it is yet unknown how well this method works on a 3D model, a larger error is used. In order to find the influence of these inaccuracies data set 4 (constant permanent magnetization with noise) is used.

Figure 8.42: Animation, with χ_{est} = randnrm(100,5)

In figures 8.43 and 8.44 the results for this model can be seen. The estimates of the induced magnetic field have a maximum absolute field error of 0.06944 μT, which is higher than the maximum absolute field error of 0.013 μT from section 8.6.1, where $\chi_{est} \equiv \chi_{true}$. Since the relative field errors are still less than 1% we can conclude that the predictions are still very good. In figure 8.44 it can be observed that the absolute errors are far below the noise level for each component, which is positive as well. Further it is interesting to find that the permanent magnetization is now corrected differently than with $\chi_{est} = \chi_{true}$, see figure 8.20. Where with exact χ the permanent magnetization was corrected to the true values, now the estimates keep changing. Note that for positive applied field the estimate of $\mathbf{M}_{per}$ is higher than the true value 500 and for negative applied field the estimate of $\mathbf{M}_{per}$ is below the true value. This

[4] Enlarged versions of these figures can be found in appendix A.

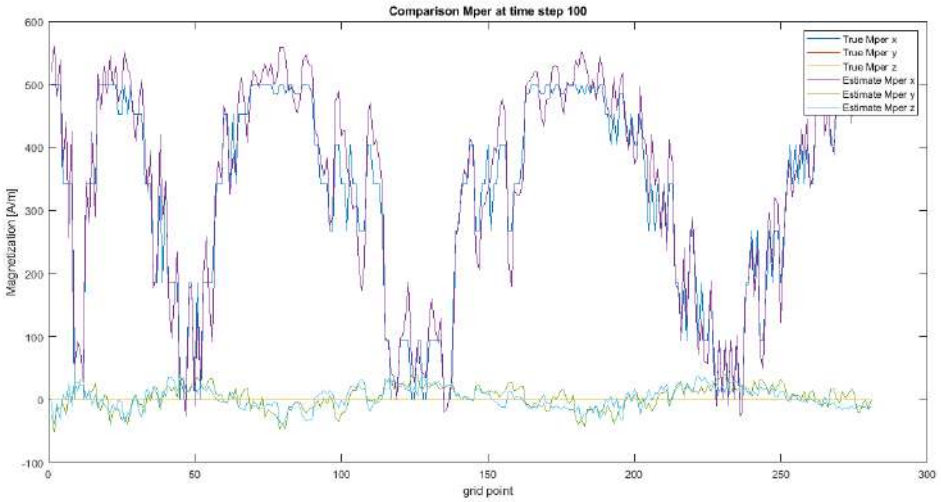

Figure 8.41: Comparison estimated $\mathbf{M}_{per}$ with true $\mathbf{M}_{per}$ at time step 100 for $\lambda = 5 \cdot 10^{-8}$ and noise $= 2 \cdot 10^{-7}$ [4]

might imply that the data-based corrections on $\mathbf{M}_{per}$ are also able to correct some of the influences of the errors in the susceptibility estimate.

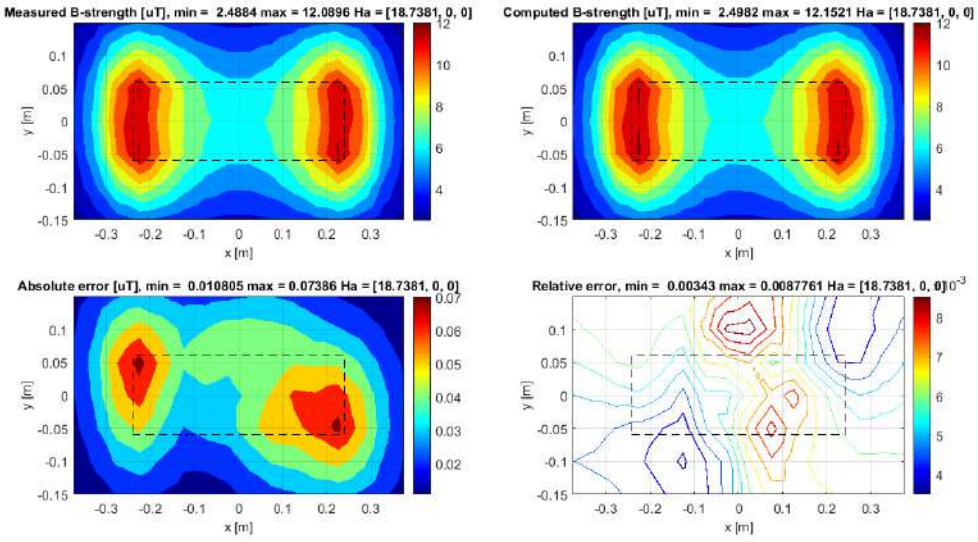

Figure 8.43: Measurements, predictions and errors induced field strength with regularization λ = 'free', noise $= 2 \cdot 10^{-7}$, $\mathbf{H}_a$ in x-direction and $\mathbf{M}_{per}^{true}$ 500 A/m in $x-$direction with χ_{est} = randnrm(100,5)

To push the boundaries of the model, a susceptibility distribution with mean $\mu = 90$ with standard deviation $\tau = 10$ is used. With values ranging from 60 to 120 this can be seen as an inaccurate estimate of the susceptibility. We are interested if the model is still able to generate reasonable predictions. In figure 8.46 the susceptibility distribution can be found, from the figure it can be observed that indeed the distribution is largely varying and in general not smooth, resulting in an inaccurate estimate. The results of the model can be found in figures 8.47 and 8.48. It is evident from the figures that the estimates are far less accurate than in the previous case. The maximum absolute field error has increased to $0.28\mu T$ and the relative field error has increased to more than 2%. From figure 8.48 it is clear that the separate absolute errors have increased, but they are still below the noise level, which is positive. Further it is now

Figure 8.45: Animation, with χ_{est} = randnrm(90,10)

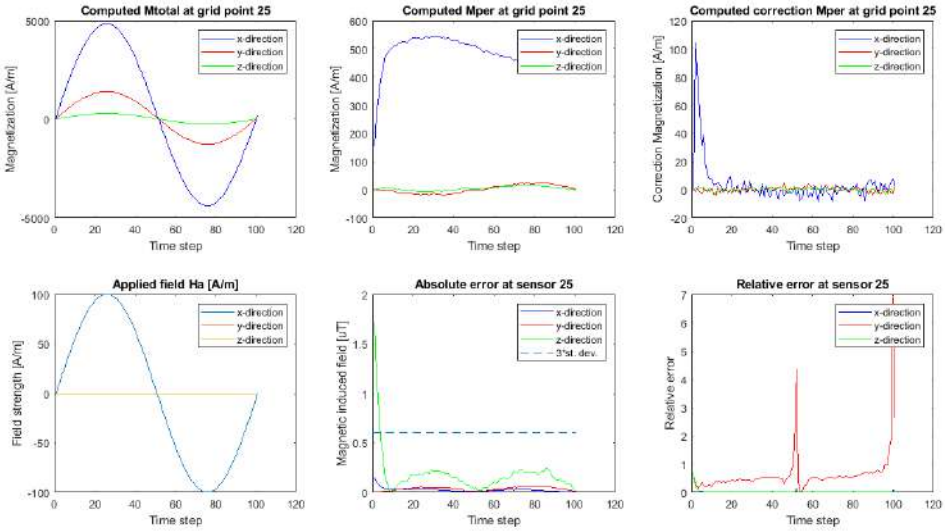

Figure 8.44: Evolution of magnetization and prediction errors over time with regularization λ = 'free', noise = $2 \cdot 10^{-7}$, $\mathbf{H}_a$ in $x-$direction and $\mathbf{M}_{per}^{true}$ 500 A/m in x-direction with χ_{est} = randnrm(100,5).

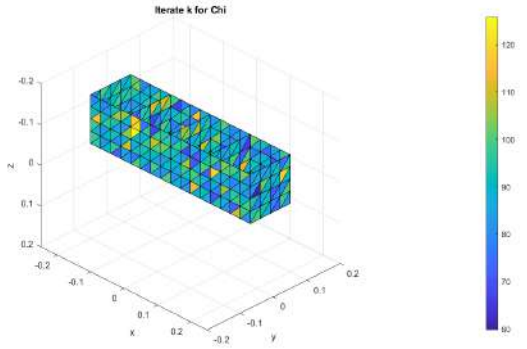

Figure 8.46: Susceptibility distribution χ_{est} = normrnd(90,10).

evident that the estimate of the permanent magnetization truly tries to correct for the inaccuracies in the susceptibility estimate. We observe that the relative error in the $y-$direction is large. The two peaks occur due to the fact that the field is very close to zero as described earlier. Here the $y-$field is in general over all time steps very small, which has the result that the noise-components have large influence on the relative errors. This can also be seen in the fact that the absolute errors are smallest for the $y-$direction. Therefore we can largely ignore the high relative errors in the $y-$directions. It can be observed that the absolute errors in the $x-$direction are largest when the applied field is largest. Note that when the applied field is largest, also the influence of χ is the largest. From this is can be seen that a large part of the absolute errors are caused by the inaccurate χ_{est}. Although naturally more research will need to be done, it is very promising to see that the model is able to handle inaccuracies in the susceptibility estimate quite well.

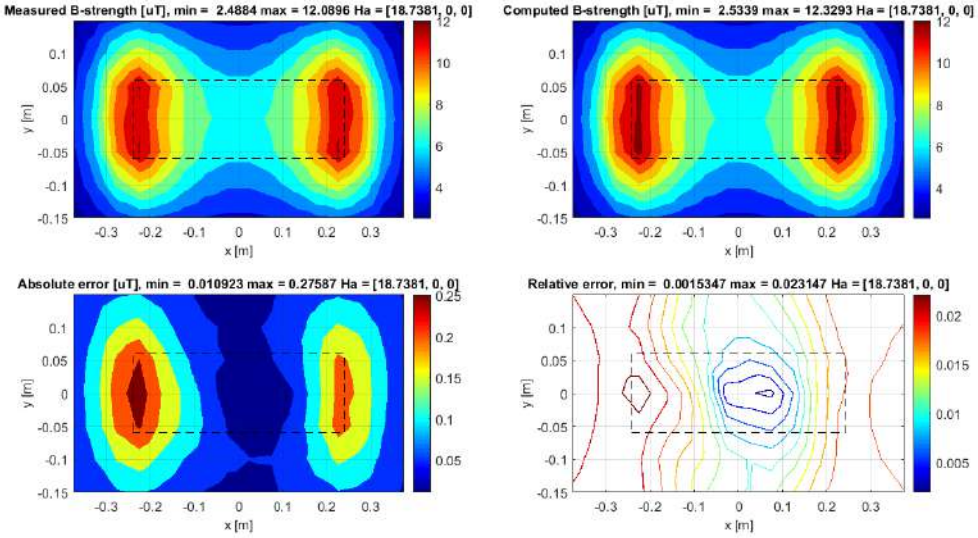

Figure 8.47: Measurements, predictions and errors induced field strength with regularization λ = 'free', noise = $2 \cdot 10^{-7}$, $\mathbf{H}_a$ in $x-$direction and $\mathbf{M}_{per}^{true}$ 500 A/m in $x-$direction with χ_{est} = randnrm(90,10)

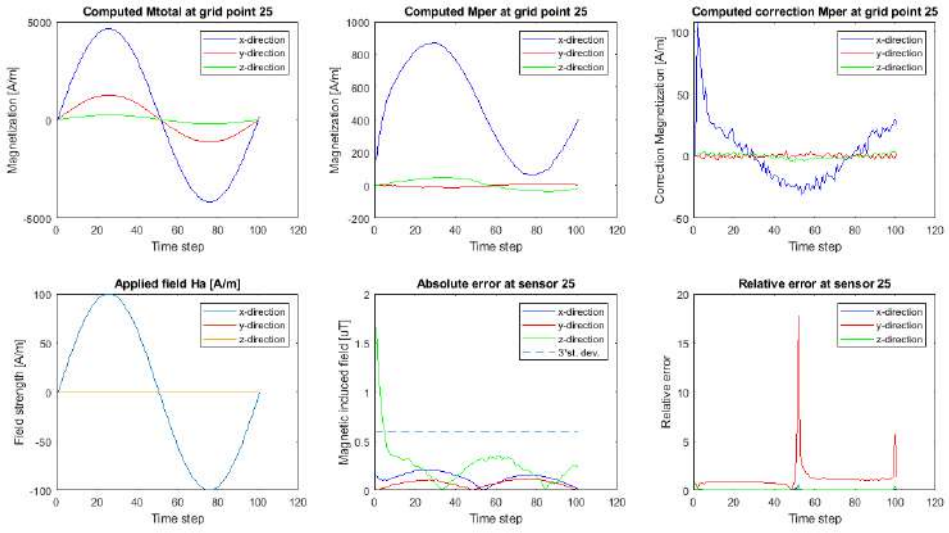

Figure 8.48: Evolution of magnetization and prediction errors over time with regularization λ = 'free', noise = $2 \cdot 10^{-7}$, H_a in $x-$direction and $\mathbf{M}_{per}^{true}$ 500 A/m in x-direction with χ_{est} = randnrm(90,10).

8.11. Conclusion phase III

Phase III consisted of three twin experiments to test the performance of the model on more complex situations. First a linear varying permanent magnetization was used in the generated data. It was concluded that although the errors increased with respect to the constant permanent magnetization, the model is able to compute accurate predictions on the magnetic signature. It was also observed that the model was able to track, with a slight delay, the varying permanent magnetization with the data-driven updates. This is a very positive and promising result.

In the second conducted twin experiment a non-uniform permanent magnetization is used, since in practice these distributions are non-uniform. Unfortunately the errors of the predicted magnetic signatures increased largely and the model was not able to estimate the non-uniformity in the initial condition. In order to give the model more freedom to fit the data instead of the regularity term, the regularization term λ was chosen smaller by hand. Fortunately the smaller λ improved the predictions to the accuracy from phase II. Further it was observed that in this case the model is able to compute an accurate estimate for the permanent magnetization. From this twin experiment is is concluded that the model is able to give accurate predictions for non-uniform permanent magnetizations. However the L-curve does not find an optimal λ for this case, such that it is important to find another method for the computation of an optimal λ.

In the last twin experiments the susceptibility distribution was no longer assumed to be known. In order to find how well the model is able to handle inaccuracies from the susceptibility estimate, two different susceptibility estimates were used as input. From the experiments it was concluded that the model can handle these inaccuracies quite well. The data-driven updates on the permanent magnetization capture a part of the errors caused by the susceptibility estimate as well. It was also concluded that if the errors in the susceptibility estimate become too large they are translated into the predictions. To sum up we can say that the model has the promising property of being able to correct inaccuracies in the susceptibility estimate. However more research will need to be done in order to understand how much of the errors in the susceptibility method are truly translated to errors in the predictions.

9

Conclusion

In this chapter we wrap up our research, first the research objectives and the main results are posed. Secondly a short summary on the model design is provided and at last more conclusions on the performance of the model are given.

9.1. Research objectives and main results

The aim of this research was defined as follows:

"Design, implement and test a data-driven model for the induced magnetic field of an object, made of linearly reacting isotropic material, considering both induced and permanent magnetization."

In chapter 2 we defined the following six sub-objectives:

- Design a mathematical-physical model, create the numerical model and implement the model;
- Perform a study on inverse problems, difficulties associated with inverse problems and methods, like regularization, to cope with these difficulties;
- Design and perform twin experiments to test the performance of the model;
- Research the accuracy of the predictions of the magnetic signature;
- Gain insight in the translation of errors in the estimate of the magnetization to errors in the signature prediction;
- Gain knowledge of the influence of inaccuracies in the estimation of the susceptibility on the accuracy of the prediction of the induced magnetic field.

In chapters 3-4 the first research objective is covered. The second objective is discussed in chapter 5 and 6. The last four objectives are all covered by the twin experiments in chapter 8.

From the twin experiments we are confident that the designed model is correct and is able to compute accurate predictions on the magnetic signature, considering both induced and permanent magnetization, even when the onboard data is contaminated with noise. The study on inverse problems and the twin experiments have shown that the use of regularization is essential to achieve accurate predictions. Further we can conclude that the use of data-assimilation is a good method to approximate the permanent magnetization in a varying applied field and in fact is essential for achieving high accuracy in the predictions of the magnetic signature. We found that the data-assimilation is also able to correct possible inaccuracies in the estimate of the magnetic susceptibility distribution. At last it is shown that the model is able to approximate linearly varying as well as non-uniform permanent magnetization

9.2. Signature Monitoring Model

In this section we give a short summary on the assumptions for and the structure of the model. For the model it has been assumed that the object is made of linearly reacting isotropic material, the geometry of the object is known and the applied field is uniform in a certain volume of interest around the object. For the model it is used that the total magnetization consists of two components, the induced magnetization, which reacts linearly with the applied field, and the permanent magnetization, which is based on the magnetic history of the material. In the model the data assimilation is used to correct the permanent magnetization at each time step.

After the initial computation of the permanent magnetization and the magnetic susceptibility, the induced magnetization is computed, based on the applied field and previous permanent magnetization. From the computed magnetization the induced magnetic field at the onboard sensors can be computed. Comparison of this computed field with the measured field at the onboard sensors is used to compute a correction on the permanent magnetization. The induced magnetization is then computed again, now using the corrected permanent magnetization. From the total magnetization the induced magnetic field at a certain distance around the object can be computed for this time step. This process is repeated for every time step.

The model consists of ill-posed inverse problems. In chapter 5 a study is conducted on inverse problems and regularization. In the model Tikhonov regularization is used to improve the solutions of these problems. The regularization parameter is optimally chosen by the L-curve and the regularization operator is constructed such that it adds smoothness to the solution. It is found that the use of regularization is essential to achieve accurate solutions from the inverse problems.

9.3. Performance of the model

The performance of the model is tested with a number of twin experiments. For data sets without noise and with constant permanent magnetization it is shown that the model is able to estimate the true value of the permanent magnetization perfectly and is able to give predictions on the magnetic signature with high accuracy. The maximum absolute field error ε^s_{abs} is in the order of 0.13 nT and the relative field error is in the order of 0.001%, which is very accurate. To achieve these accuracies it has been shown that regularization and data-assimilation are essential.

We have also investigated the performance of the model when the measurements of the onboard sensors are contaminated with noise. Gaussian white noise with standard deviation $2 \cdot 10^{-7}$ was used to achieve noise of approximately 1 μT in each sensor. It is concluded from the experiments that the regularization is able to dampen the noise components in the measurements, which is positive. The results get less accurate, but the absolute errors are still far below the noise level, from which it can be concluded that the results are accurate.

Further we have considered more complex situations with linearly varying and non-uniform permanent magnetization. From the experiments we can conclude that the model is able to approximate a linearly varying permanent magnetization and give accurate predictions on the magnetic signature. It is also concluded that the model is able to approximate a non-uniform permanent magnetization. However it is shown that in this case the L-curve does not provide an optimal, or even good, regularization parameter. The accurate predictions are achieved by choosing a fixed smaller regularization parameter. This parameter is chosen by trial and error and it is not known if this is in fact the optimal parameter for this twin experiment.

At last we have investigated the influence of an inaccurate susceptibility estimate on the accuracy of the model. It is shown that the model is able to correct inaccuracies in this estimate by the data-driven updates on the permanent magnetization. For small inaccuracies (5-15% deviation) in the susceptibility estimate the model still performs with approximately the same accuracy as without errors in the susceptibility estimate. For large errors in the susceptibility estimation (10-30% deviation) the model performs with less accuracy. However the found errors are still acceptable, considering the large deviation in the susceptibility estimate

The named conclusions all support the main result that the model is correctly formulated and is able to compute accurate predictions on the magnetic signature.

10

Future research

In our research we have set many steps towards the Magnetic Signature Monitoring System. However we have also encountered some difficulties or inaccuracies which are good food for future research. In this chapter we pose the ideas for the future.

10.1. Inverse problems

One of the critical points in the current model is the number of ill-posed inverse problems that need to be solved. Ill-posed problems often lead to inaccurate solutions and therefore must be reformulated to receive improved solutions. For inverse problems many methods have designed to improve these solutions. In order to improve the accuracy of the model it is important to research the possibilities for other methods, related to inverse problems.

10.1.1. Regularization methods

The current model uses Tikhonov regularization to improve the solutions from the ill-posed inverse problems. However much research has been done on inverse problems and regularization techniques. It might be that Tikhonov regularization is not the best method for this problem. It can be investigated whether other regularization methods can improve the solutions. It can be investigated whether using for example the Conjugate Gradient Least Squares (CGLS) method for solving the inverse probelm can improve the solutions. Another approach is by considering the inverse problem in the Bayesian statistic framework and solving it in a stochastic way. It might also be possible to alter the Tikhonov formulation to improve the solutions from this regularization. The inversions might for example be improved when the 1-norm is used instead of the 2-norm in the Tikhonov regularization.

Instead of changing the regularization method, it is also possible to alter the regularization operator. In the regularization operator R we have added the requirement that the solution must be smooth. This smoothness condition is constructed such that the permanent magnetization at each grid point must be the (weighted) average of its adjacent grid points, with a certain innovation factor. It might be possible that the smoothness condition is too strict to be able to reach a better solution. Relaxing the smoothness requirement can improve the solutions from the inverse problems. It is also possible to think of other properties that the inverse solutions should satisfy. From these properties another regularization operator R could be defined.

10.1.2. Regularization parameter

In the current model the regularization parameter λ is computed optimally by the L-curve. For non-uniform permanent magnetization we found that the L-curve is not able to estimate an optimal λ. Since in practice the permanent magnetization is non-uniform, it is important that a better method is found to compute an optimal regularization parameter λ. It might be considered to use the Bayesian statistical framework instead of the deterministic framework. Using the Maximum A Posteriori estimate from Bayesian statistics it might be possible to find a better prior estimate for λ.

10.2. Data-assimilation

The data-assimilation is an important part of our model as it completely describes the permanent magnetization. It is therefore very important that the data-assimilation is able to handle noise in the measurements correctly. At this moment only basic data-assimilation is used. However more complex methods have been designed, which might improve the results from data-assimilation. One method that can be considered is Kalman filtering.

10.2.1. Permanent magnetization

The basis of the model consists of the state correction by data assimilation, for the current model the correction is completely based upon one data assimilation step. In this research it was observed that the initial estimate for the permanent magnetization could be improved by performing multiple data-driven updates based on the same data set. We wonder whether adding multiple updates to the correction step at each time step can improve the accuracy of the permanent magnetization update.

At this moment only data-assimilation is used to estimate the permanent magnetization. It can be researched if the predictions can be improved by designing a mathematical-physical model update on the permanent magnetization. With this model for the update, the data-assimilation only needs to focus on correcting errors made by the update model.

10.2.2. Susceptibility

Before the model can be used in practice, we must be able to compute estimates of the susceptibility. As named before in [22] an estimation method for the magnetic susceptibility has been designed. Unfortunately due to time reasons we did not have time to implement this method into our model. We did find that small inaccuracies in this estimate can be corrected by the data-assimilation. It can be considered to update the susceptibility estimate together with the permanent magnetization as well. It might be possible that the data-assimilation is able to correct the susceptibility estimate to the true values.

10.2.3. Number of sensors

At this moment the model uses all available sensors for the data assimilation. For the future it is of great importance to gain insight into the number of sensors necessary for an accurate approximation. The SVP01 contains 24 onboard sensors, when translated to a naval vessel the number of sensors increases drastically. It will be necessary to research how the prediction changes if more or less sensors are used and also if more accurate sensors can significantly improve the predictions.

10.3. Performance tests

Although the model has been tested on multiple cases, there are still more situations available to check the performance of the current model. In this section we discuss multiple cases which can be used to test the performance of the model and different parts of the model which still need to be tested.

10.3.1. Computational efficiency

Due to time reasons no analysis has yet been done on the computational efficiency of the model. The model should be able to predict the magnetic signature in real-time. Large structures like naval vessels lead to very large systems, for which computations are computationally intensive. In order to be able to predict in real-time the formulation and implementation should be as efficient as possible.

For convenience we used implementation of Tikhonov by Hansen, which makes use of the generalized singular value decomposition for the computation. The use of the GSVD is computationally speaking not the most efficient method, it can be considered to use the Eldén bidiagonalization algorithm instead, which might improve the time consuming correction steps of the model.

10.3.2. Internal structure
For the application is naval vessels it is also of great importance to acquire information on the importance of modeling internal structures. With the SVP01 the influence of the removal of the subplates in the CAD-model on the predictions can be tested. If there is only a very small negative influence of removing the internal structures from the CAD-model, this could improve the efficiency of the prediction model. Note that for complex geometries like naval vessel it will be far more efficient if not all internal structures like engines and weaponry need to be modelled.

10.3.3. Influence of distance
In the current tests, the sensor array is always located at the same distance. However it is also of interest to know how the inaccuracies evolve if the sensor array is moved further away or closer to the object. It might occur that the estimate of the magnetization is less important if there is more distance between the object and the sensor array. This might reduce the need for very accurate predictions on the magnetization.

10.3.4. Complex situations and prototypes
The model has been tested on a few different, simple, situations. Naturally, the model must be tested on more complex and lifelike prototypes and in more complex situations. In this research for time reasons the magnetization and applied fields were only considered in one separate directions. Tests can be performed to find if the model works accurately when the permanent magnetization is in a different direction than the applied field.

Note that in the research it is assumed that the applied field is uniform. In practice the applied field is not known exactly and measurements contain noise. It must be investigated how well the model performs with noise in the applied field, one of the most important inputs of the model.

10.3.5. Experimental Data
Although we can gain knowledge on the performance of the model by numerical tests, like twin experiments, it is also of great interest to test the performance of the model on real experimental data. In chapter 7 an experimental setup was described. Unfortunately due to a lack of time it has not been possible to include experimental tests with this setup in this report. It will be interesting to find how accurate the model performs in real experiments.

Bibliography

[1] M. Bosack, J. Kollmer, B.Niemoczynski, and S. Biswas. Closed loop control of hysteretic magnetization. *IEEE International Symposium on Resilient Control Systems*, 7th, 2014.

[2] D. Calvetti, S. Morigi, L. Reichel, and F. Sgallari. Tikhonov regularization and the l-curve for large discrete ill-posed problems. *Elsevier, Journal of Computational and Applied Mathematics*, 123:423–446, 2002.

[3] J. M. D. Coey. *Magnetism and Magnetic Materials*. Cambridge University Press, 2009. ISBN 978-0-511-67743-4.

[4] P. C. Hansen. Regularization tools: A matlab package for analysis and solution of discrete ill-posed problems. *Numerical Algorithms*, 6, 1994.

[5] P. C. Hansen. *Rank-Deficient and Discrete Ill-Posed Problems: Numerical Aspects of Linear Inversion*. SIAM, 1998.

[6] P. C. Hansen. *Discrete Inverse Problems: Insight and Algorithms*. SIAM, 2010. ISBN 978-898716-96-2.

[7] P. C. Hansen and D.P. O'leary. The use of the l-curve in the regularization of discrete ill-posed problems. *SIAM J. Sci. Comput.*, 14:1487–1503, 11 1993.

[8] R. G. Harrison. A physical model of spin ferromagnetism. *IEEE Trans. Magn.*, 39:950, 2003.

[9] R. G. Harrison. Physical theory of ferromagnetic first order return curves. *IEEE Trans. Magn.*, 45:1922, 2009.

[10] J. J. Holmes. *Exploitation of A Ship's Magnetic Field Signatures*. Morgan & Claypool publ., Inc., 2006.

[11] J. J. Holmes. *Modeling of a Ship's Ferromagnetic Signatures*. Morgan & Claypool publ., Inc., 2007.

[12] J. J. Holmes. *Reduction of A Ship's Magnetic Field Signatures*. Morgan & Claypool publ., Inc., 2008.

[13] J. D. Jackson. *Classical Electrodynamics*. John Wiley & Sons, Inc, New York, 3rd edition, 1999.

[14] D. C. Jiles and D. L. Atherton. Theory of the magnetisation process in ferromagnets and its application to the magnetomechanical effect. *J. Phys. D: Appl. Phys*, 17(1265), 1984.

[15] M. Kachniarz and R. Szewczyk. Study on the rayleigh hysteresis model and its applicability in modeling magnetic hysteresis phenomenon in ferromagnetic materials. *12th Symposium of Magn. Meas. and Mod.*, 131(5), 2017.

[16] B. Kagström. The generalized singular value decomposition and the general (a-λ b)-problem. *BIT Num. Math.*, 24, 1984.

[17] H.P. Langrangen and K.A. Mardal. *Introduction to Numerical Methods for Variational Problems*. 2016.

[18] E. Motovilova and S. Huang. *Advances in Magnetic Materials*. CRC Press, 2017.

[19] C. C. Paige and M. A. Saunders. Towards a generalized singular value decomposition. *SIAM J. Numer. Anal.*, 18(3), 1981.

[20] O. J. G. Somsen and G. P. M. Wagemakers. Separating permanent and induced magnetic signature: A simple approach. *International Journal of Electrical, Computer, Energetic, Electronic and Communication Engineering*, 9(10), 2015.

[21] E.D. Torre. *Magnetic Hysteresis*. Wiley-IEEE Press, 1999.

[22] A. Vijn, E. Lepelaars, J. Dubbeldam, M. van Gijzen, and A. Heemink. Magnetic susceptibility estimation for magnetostatics. *IEEE Transaction on Magnetics (submitted)*, 2018.

[23] A.R.P.J. Vijn. Inverse modeling for magnetic signature monitoring of naval ships. Master's thesis, University of Technology Delft, 2016.

[24] S. E. Zirka, Y. I. Moroz, R. G. Harrison, and K. Chwastek. On physical aspects of the jiles-atherton hysteresis models. *Journal of Applied Physics*, 112, 2012.

A

Enlarged figures

In this appendix enlarged versions of figures 8.6, 8.22,8.35 and 8.40 can be found.

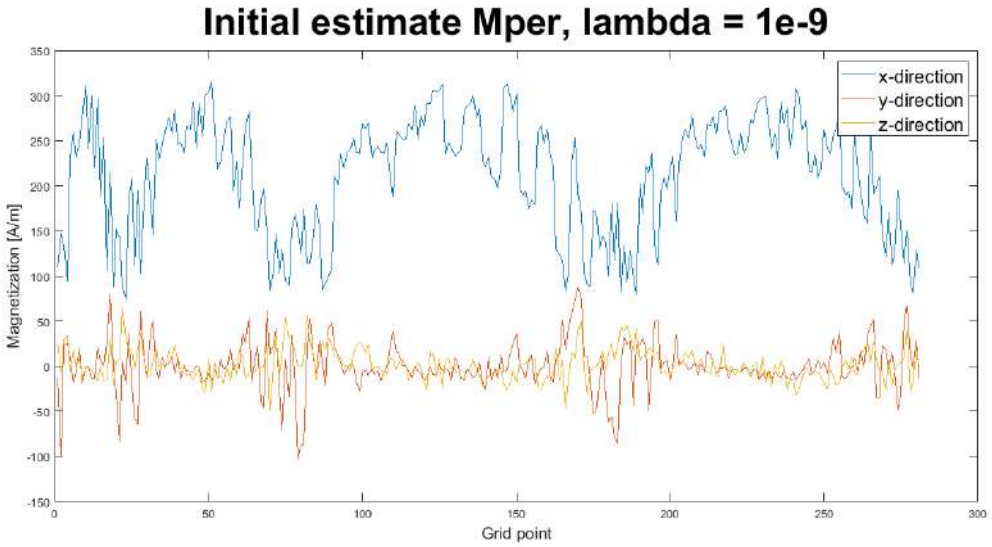

Figure A.1: Initial estimate permanent magnetization with regularization parameter $\lambda = 10^{-9}$ (8.6a)

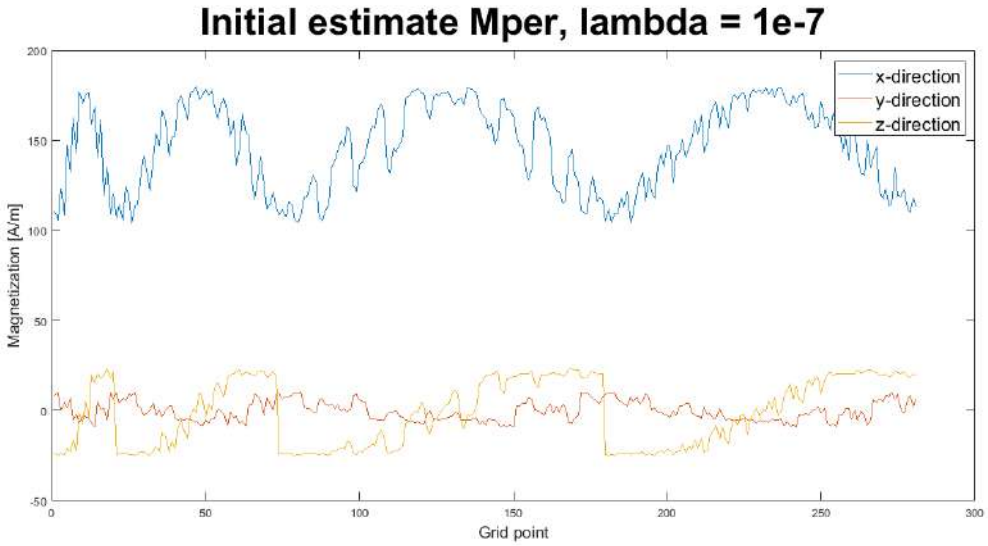

Figure A.2: Initial estimate permanent magnetization with regularization parameter $\lambda = 10^{-7}$ (8.6b)

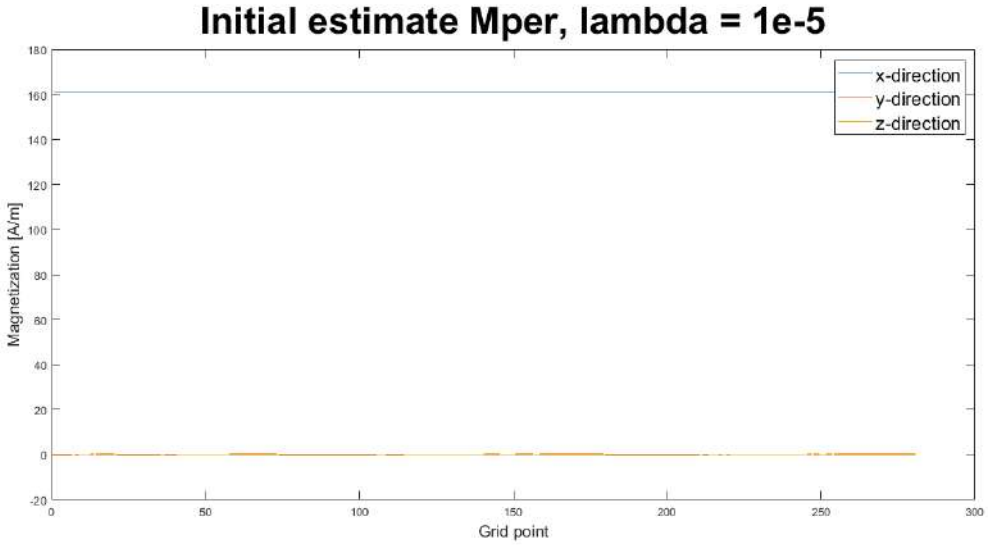

Figure A.3: Initial estimates permanent magnetization with regularization parameters $\lambda = 10^{-5}$

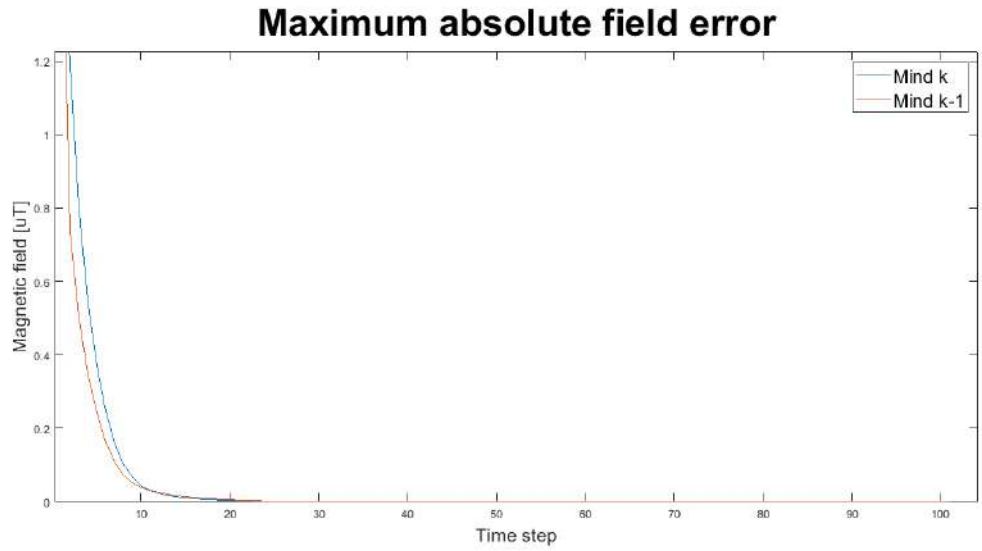

Figure A.4: Maximum absolute field errors for model with and without extra $\mathbf{M}_{ind}$ update for constant permanent magnetization with λ = 'free', without noise (8.22a)

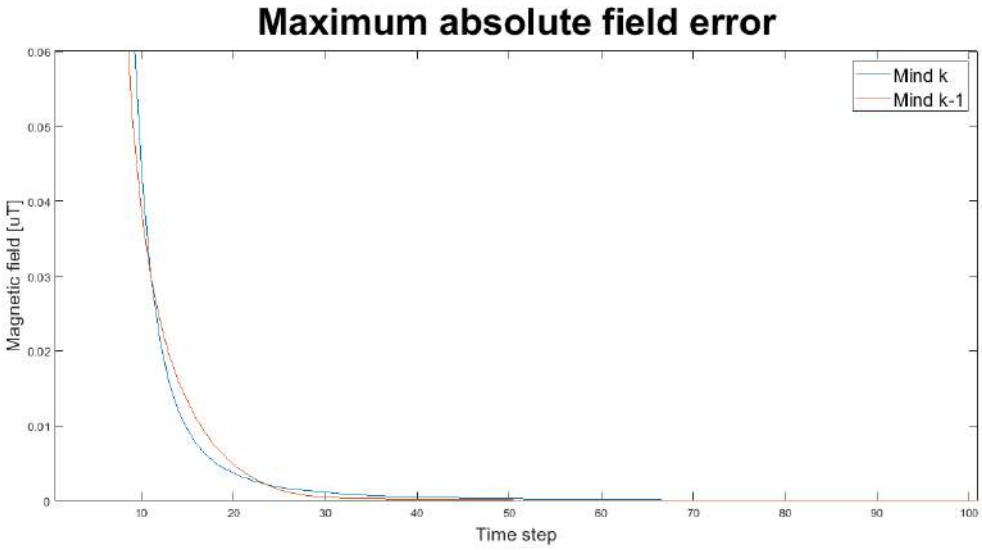

Figure A.5: Maximum absolute field errors for model with and without extra $\mathbf{M}_{ind}$ update for constant permanent magnetization with λ = 'free', without noise, zoomed (8.22b)

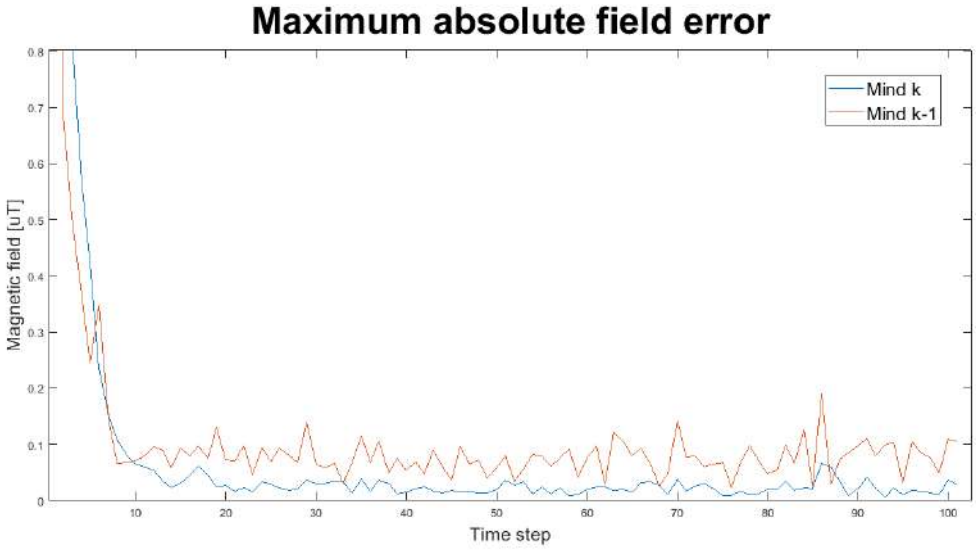

Figure A.6: Maximum absolute field errors for model with and without extra $\mathbf{M}_{ind}$ update for constant permanent magnetization with λ = 'free', with noise (8.22c)

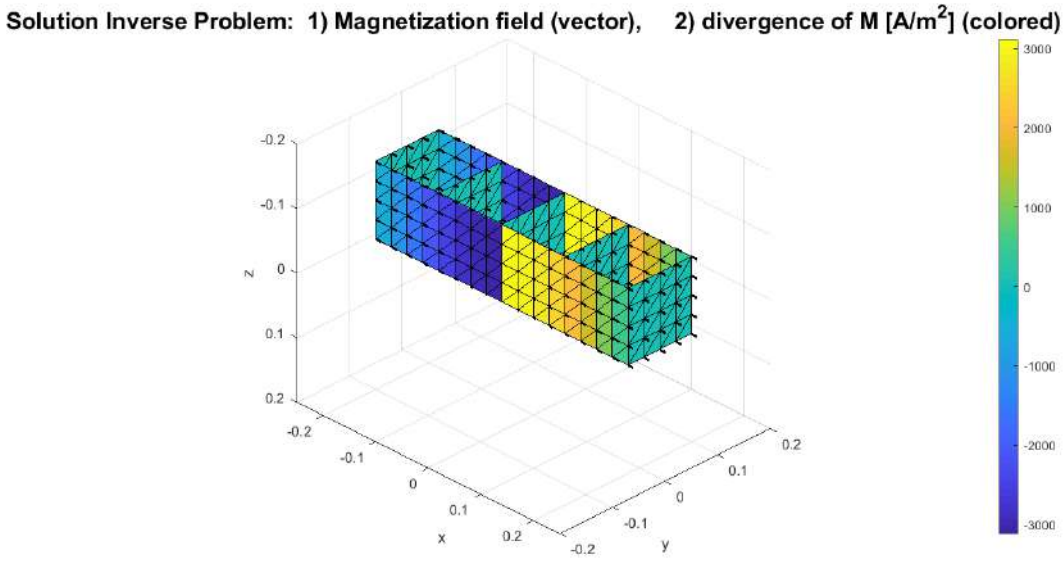

Figure A.7: True non-uniform $\mathbf{M}_{per}$ and divergence with λ = 'free' and noise = $2 \cdot 10^{-7}$ (8.35a)

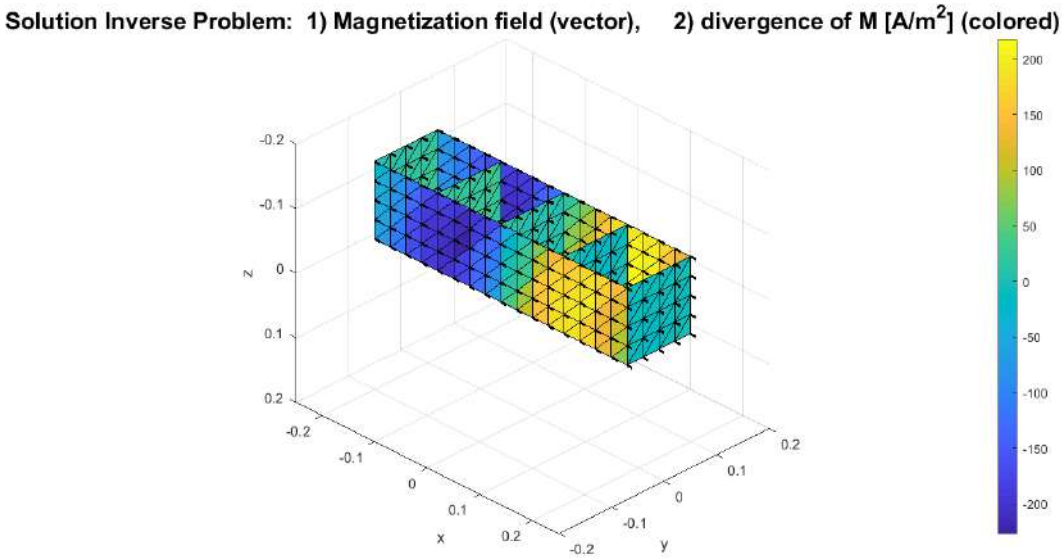

Figure A.8: Estimated non-uniform $\mathbf{M}_{per}$ and divergence with λ = 'free' and noise = $2 \cdot 10^{-7}$ (8.35b)

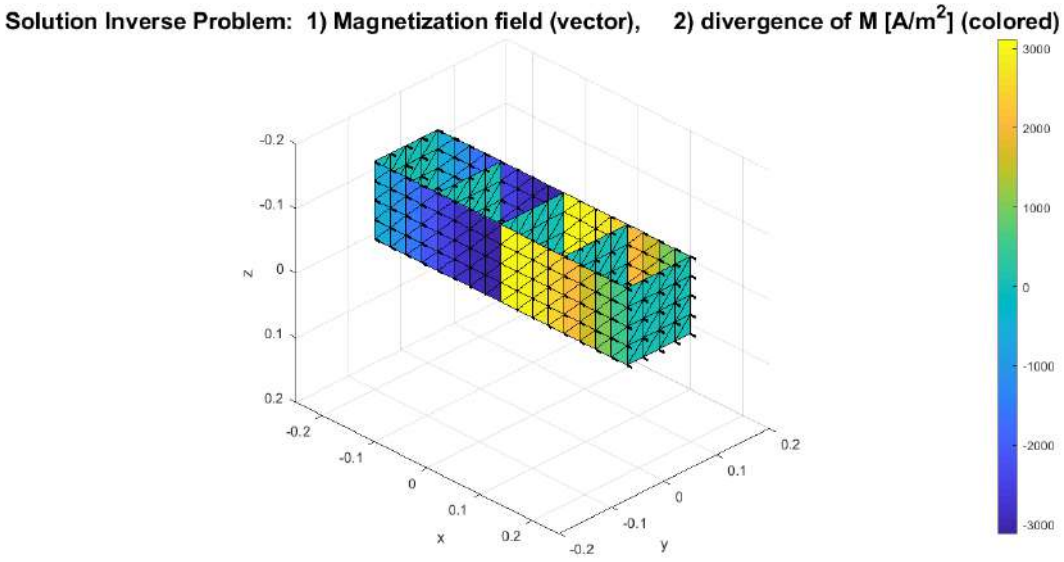

Figure A.9: True non-uniform $\mathbf{M}_{per}$ and divergence with lambda = $5 \cdot 10^{-8}$ and noise = $2 \cdot 10^{-7}$ (8.40a)

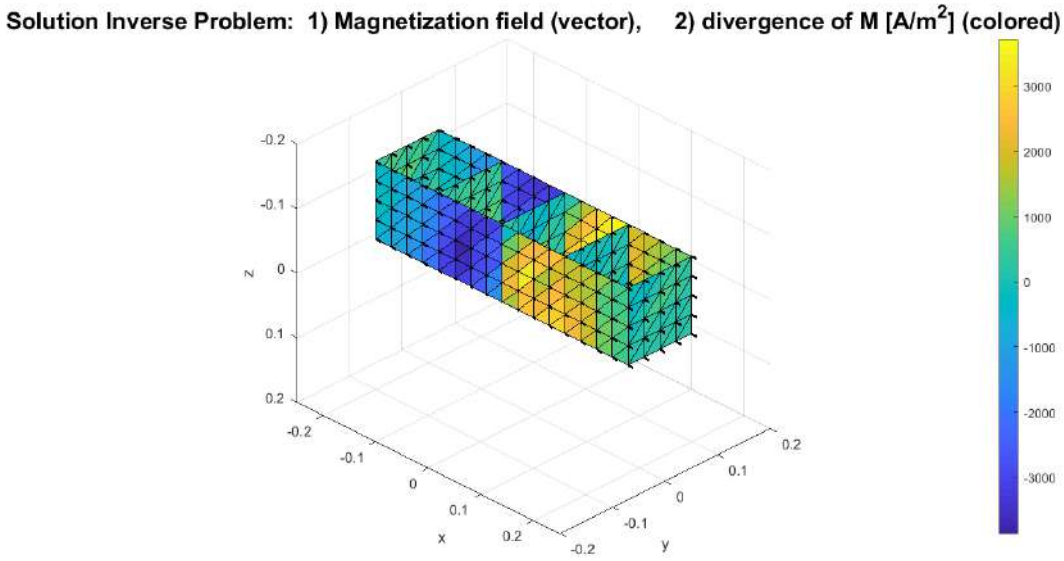

Figure A.10: Estimated non-uniform $\mathbf{M}_{per}$ and divergence with lambda = $5 \cdot 10^{-8}$ and noise = $2 \cdot 10^{-7}$ (8.40b)